Order Number 9304688

Part I. Evaluation of thermodynamic and kinetic parameters for electron transfer and following chemical reaction from a global analysis of current-potential-time data. Part II. Electro-catalytic detection in high-performance liquid chromatography of vitamin B_{12} and other molecules of biological and environmental interest

Kumar, Vimal T., Ph.D.

City University of New York, 1992

U·M·I
300 N. Zeeb Rd.
Ann Arbor, MI 48106

11

PART I. EVALUATION OF THERMODYNAMIC AND KINETIC PARAMETERS FOR ELECTRON TRANSFER AND FOLLOWING CHEMICAL REACTION FROM A GLOBAL ANALYSIS OF CURRENT-POTENTIAL-TIME DATA

PART II. ELECTRO-CATALYTIC DETECTION IN HIGH PERFORMANCE LIQUID CHROMATOGRAPHY OF VITAMIN B_{12} AND OTHER MOLECULES OF BIOLOGICAL AND ENVIRONMENTAL INTEREST

by

Vimal Kumar

A dissertation submitted to the Graduate Faculty in Chemistry in partial fulfillment of the requirements for the degree of Doctor of Philosophy, The City University of New York.

1992

This manuscript has been read and accepted for the Graduate Faculty in Chemistry in satisfaction of the dissertation requirement for the degree of Doctor of Philosophy.

6/23/92
Date

Ronald H Levine
Chair of examining Committee

6/23/92
Date

Executive Officer

David Lavallee

Charlotte J. Kinsella

Supervisory Committee

The City University of New York

Abstract

PART I. EVALUATION OF THERMODYNAMIC AND KINETIC PARAMETERS FOR ELECTRON TRANSFER AND FOLLOWING CHEMICAL REACTION FROM A GLOBAL ANALYSIS OF CURRENT-POTENTIAL-TIME DATA

PART II. ELECTRO-CATALYTIC DETECTION IN HIGH PERFORMANCE LIQUID CHROMATOGRAPHY OF VITAMIN B_{12} AND OTHER MOLECULES OF BIOLOGICAL AND ENVIRONMENTAL INTEREST

by

Vimal Kumar

Advisor: Professor Ronald L. Birke

PART I: Simultaneous evaluation of electron transfer rate constant, k^o, following chemical reaction rate constant, k_f, electron transfer coefficient, α and standard potential, $E^{o'}$ for an electrochemical reaction following the EC mechanism is described. A mathematical model for the current response to a potential step is developed, starting with the Butler-Volmer equation for electrode kinetics and concentration expressions for the redox couple. The resulting integral equations are solved numerically via the Step Function method. Current-potential and current-time curves are simulated and tested under limiting conditions. The four parameters of the system are then evaluated by fitting simulated current-voltage-time (i-E-t) surface to the theoretical equation, thus demonstrating the validity of the method. The

method is then applied to study an important biological molecule, viz., methyl cobalamin, in DMSO. The parameters determined for this system are: $\alpha = 0.552 \pm 0.004$; $k^o = 0.0052 \pm 0.0005$ cm s^{-1}; $kf = 1500 \pm 140$ s^{-1}; $E^{o'} = -1.54 \pm 0.01$ V. Included in the discussion part, is the use of kinetic zone diagrams, to depict chronoamperometric current response as a function of dimensionless rate constants, for the EC reaction scheme. This compact display of the influence of the two rate constants on current in all time windows can be used to select the best data for analysis. Theoretical limits of measurable rate constants can also be estimated from the zone diagram.

PART II. The development of a dropping mercury electrode detector for High Performance Liquid Chromatography (HPLC) and its application to analysis of B_{12} and other vitamins is described. This EC detector is able to achieve high levels of sensitivity by exploiting the catalytic hydrogen evolution undergone by many nitrogenous organic molecules. The detector could be used in conjunction with a simple pulse polarograph of a more sophisticated computer system offering a wide choice of waveforms and other data handling options. Vitamin B_{12}, thiamine, riboflavin and niacinamide were analyzed individually and in mixtures on reverse phase C18 column. The detection limit and linear dynamic range compared very favorably with UV-Vis detection using a modern commercial instrument (Waters 600E). Preliminary results from the analysis of commercial multivitamin preparations are also discussed.

Acknowledgements

I wish to thank professor Ronald L. Birke, my thesis mentor for his help and guidance. I enjoyed working with him for many reasons. Apart from being available whenever I needed help, the projects he offered in the area of Analytical Chemistry and Computer Applications were challenging, exciting and very much to my liking. I also wish to thank professor Charlotte Russell and professor David Lavallee, for finding time in their busy schedules to serve on my thesis committee.

TABLE OF CONTENTS

PART I.

PART II

LIST OF TABLES

PART I

PART II

LIST OF FIGURES

PART I

PART II

PART I

EVALUATION OF THERMODYNAMIC AND KINETIC PARAMETERS FOR ELECTRON TRANSFER AND FOLLOWING CHEMICAL REACTION FROM A GLOBAL ANALYSIS OF CURRENT-POTENTIAL-TIME DATA

1.1 Introduction

Electrochemical experiments in general can be considered as the measurement of current vs the experimental variables, time and applied voltage. Even though valuable information about the electrochemical process being studied is contained in the entire set of experimental data acquired, often times only a few selected points are used in data analyses. Typically, a cyclic voltammetric study may utilize only the values of peak current and peak potentials in determining parameters such as rate constants or standard potential. With digital computers, widely available in the laboratory, it is now possible to extract information from a much larger data set. This section describes simultaneous evaluation of thermodynamic and kinetic parameters associated with electrode reactions and coupled chemical reactions from an analysis of the current-voltage-time surface. This differs from the usual approach of studying current-voltage or current-time curves which are in two dimensional space. The three-dimensional analysis described here draws data from the entire domain of electrochemical measurements; naturally, the confidence in the parameter values estimated is higher.

The development of a mathematical model for an electron transfer reaction followed by a chemical reaction is described first. The model is used to simulate current vs time curves and current vs potential curves. These current-time and current-potential curves are then tested under various limiting conditions

to ensure the validity of the model and the simulation method. Attempts to evaluate the standard potential ($E^{o'}$), the electron transfer coefficient (α), the electron transfer rate constant (k^o) and the following chemical reaction rate constant (k_f) by fitting the theoretical equation to the simulated 'experimental data' are described next. These attempts lead to the conclusion that simultaneous evaluation of the four parameters is possible only by fitting a current-voltage-time surface and not from a single current-time curve or a single current-voltage curve. The limiting forms of the equation for current, that result when the kinetic parameters assume extreme values were analyzed. This information was used to map out various regions in parameter space showing what parameters influence the current predominantly in each region. These Kinetic Zone Diagrams were used to estimate the theoretical limits of measurable rate constants. The method was then applied to study the electrochemistry of methyl cobalamin, a vitamin B_{12} derivative known for its significant role in the B_{12}-catalyzed enzymatic reactions. The heterogeneous rate constant for the reduction of methyl cobalamin, the homogeneous rate constant for the chemical reaction that follows reduction, the standard potential for the redox couple and the electron transfer coefficient are determined simultaneously.

1.2 General Current-Potential Equation

The simple case of a reaction involving soluble species occurring at an electrode-solution interface can be represented as:

$$O + ne^- \rightleftharpoons R$$

The oxidized form O picks up n number of electrons at the electrode surface getting converted to the reduced form R. The reaction has forward and backward paths as shown. The forward component proceeds at a rate v_f which is proportional to the concentration of O at the electrode surface at time t, $C_o(0,t)$ Thus,

$$v_f = k_f C_o(0,t)$$

where k_f is the proportionality constant linking the forward reaction rate to the surface concentration. The rate may be expressed in terms of the current flowing across unit area of the electrode surface:

$$k_f C_o(0,t) = \frac{i_c}{nFA}$$

where i_c is the cathodic current due to reduction of O, F is the Faradaic constant equal to 96484.6 coulombs per equivalent and A is the area of the electrode surface. Likewise the backward reaction rate can be expressed as

$$v_b = k_b C_R(0,t)$$

$$k_b C_R(0,t) = \frac{i_a}{nFA}$$

where i_a is the anodic current due to oxidation of R and k_b is the rate constant for the reverse reaction. The net reaction rate which is the difference between the forward and backward reaction rates is

$$i = i_c - i_a$$

$$i = nFA[k_f C_o(0,t) - k_b C_R(0,t)] \qquad (1.1)$$

Values of k_f and k_b depend upon the potential applied on the electrode. When the applied potential is equal to the standard potential, E^o, and the concentrations of both O and R are the same, both k_f and k_b are equal to the standard rate constant k^o. For potentials that differ from the standard potential, the rate constants are related to the standard potential through the applied potential, E and the electron transfer coefficient, α as follows [1].

$$k_f = k^o e^{\left(-\alpha nF(E-E^\circ)/RT\right)}$$

$$k_b = k^o e^{\left((1-\alpha)nF(E-E^\circ)/RT\right)}$$

Substituting these expressions for k_f and k_b into equation (1.1), for the net reaction yields the modified Butler-Volmer equation [2] for electrode kinetics:

$$i = nFAk^{o}\left[C_O(0,t)e^{\{-\alpha nF(E-E^{o})/RT\}} - C_R(0,t)e^{\{(1-\alpha)nF(E-E^{o})/RT\}}\right]$$

$$= nFAk^{o}e^{\{-\alpha nF(E-E^{o})/RT\}}\left[C_O(0,t) - C_R(0,t)e^{\{nF(E-E^{o})/RT\}}\right]$$

$$= nFAk^{o}\left[C_O(0,t) - C_R(0,t)e^{\{nF(E-E^{o})/RT\}}\right] \qquad (1.2)$$

where,

$$k^{o} = k^{o}e^{\{-\alpha nF(E-E^{o})/RT\}}$$

and R is the molar gas constant. Equation (1.2), called the current-potential characteristic, describes the relationship between current flowing through an electrode-solution interface and the potential applied on the electrode. This equation or a variation of it is used in the treatment of every problem in electrode kinetics. Current at any instant is given by the thermodynamic and kinetic parameters of the system and the concentration of O and R at the electrode surface. These concentration terms at any instant are determined by the competition between the electron transfer and coupled chemical reaction(s) as well as diffusion to and from the electrode surface.

1.3 Electron Transfer Followed by Coupled Chemical Reaction (EC Process)

The process of a homogeneous reaction following the heterogeneous electron transfer process can be represented as

$$O + ne^- \rightleftharpoons R$$

$$R \underset{k_b}{\overset{k_f}{\rightleftharpoons}} Z$$

The reduced form R gets converted to Z by chemical reaction. Removal of R from the electrode surface by the chemical process causes more O to convert to R in order to maintain the Nernstian equilibrium. This results in an increase in cathodic current. Expressions for the concentrations of the oxidized and reduced forms at the electrode surface for various electrode mechanisms have been described in the literature [3]. For the EC mechanism the concentrations, as a function of time are given by the following expressions.

$$C_O(0,t) = C_O^* - \int_0^t \frac{i(\tau)d\tau}{nFAD_O^{\frac{1}{2}}\pi^{\frac{1}{2}}\sqrt{t-\tau}}$$

$$C_R(0,t) = C_R^* + \frac{K}{1+K}\int_0^t \frac{i(\tau)d\tau}{nFAD_R^{\frac{1}{2}}\pi^{\frac{1}{2}}\sqrt{t-\tau}} + \frac{1}{1+K}\int_0^t \frac{e^{-k(t-\tau)}i(\tau)d\tau}{nFAD_R^{\frac{1}{2}}\pi^{\frac{1}{2}}\sqrt{t-\tau}}$$

where

C_O^* and C_R^* are the bulk concentrations of O and R respectively

$\ell = k_f + k_b$ is a kinetic parameter which embodies the effect of the chemical process.

D_O and D_R are the diffusion coefficients of O and R respectively

$K = k_b/k_f$

For an irreversible chemical reaction ($k_f >> k_b$),

$\frac{K}{1+K} = 0$ and $\frac{1}{1+K} = 1$

Thus for an irreversible chemical reaction following electron transfer,

$$C_O(0,t) = C_O^* - \int_0^t \frac{i(\tau)d\tau}{nFAD_O^{\frac{1}{2}}\pi^{\frac{1}{2}}\sqrt{t-\tau}} \qquad \text{and}$$

$$C_R(0,t) = C_R^* + \int_0^t \frac{e^{-\ell(t-\tau)}i(\tau)d\tau}{nFAD_R^{\frac{1}{2}}\pi^{\frac{1}{2}}\sqrt{t-\tau}}$$

Substituting the above concentration expressions into the modified Butler-Volmer equation yields an expression for the current as a function of time and applied voltage, for an electrode reaction following the EC mechanism.

$$i(t) = nFAk^o\left[C_O^* - \int_0^t \frac{i(\tau)d\tau}{nFAD_O^{\frac{1}{2}}\pi^{\frac{1}{2}}\sqrt{t-\tau}} - \left\{C_R^* + \int_0^t \frac{e^{-\ell(t-\tau)}i(\tau)d\tau}{nFAD_R^{\frac{1}{2}}\pi^{\frac{1}{2}}\sqrt{t-\tau}}\right\}e^{\frac{nF(E-E^o)}{RT}}\right]$$

Replacing D_R in the second integral by $\frac{D_R D_O}{D_O}$ and assuming that only the oxidized form is initially present,

$$i(t) = nFAk^{o}\left[C_O^{*} - \int_0^t \frac{i(\tau)d\tau}{nFAD_O^{\frac{1}{2}}\pi^{\frac{1}{2}}\sqrt{t-\tau}} - \int_0^t \frac{e^{-\ell(t-\tau)}i(\tau)d\tau}{nFAD_O^{\frac{1}{2}}\pi^{\frac{1}{2}}\sqrt{t-\tau}}\sqrt{\frac{D_O}{D_R}}e^{\frac{\alpha nF(E-E^{o'})}{RT}}\right]$$

Besides the experimental variables, time and voltage the current is also dependent on the following important parameters of the system:

k^{o}, the heterogeneous rate constant for the electron transfer process

k_f, the homogeneous rate constant for the following chemical step ($\ell = k_f$ when the following reaction is irreversible)

α, the electron transfer coefficient

$E^{o'}$, the standard potential for the redox couple

Usual methods for the evaluation of one or more of these parameters, such as cyclic voltammetry and chronoamperometry requires prior knowledge of one or more of the other parameters. Also any error in the known parameters will affect the accuracy of the ones being determined. This makes it highly desirable to evaluate these parameters simultaneously, if possible.

Simultaneous evaluation of parameters is done by fitting experimental data to the theoretical equation. A brief outline of the method called non-linear regression or curve-fitting is given below.

When a set of n data points, $y_i (i = 0, 1 \ldots\ldots n-1)$ is to be fitted to a function with adjustable parameters, the optimum value of the parameters is achieved when the weighted sum of residuals,

$$\phi = \sum_{i=0}^{n-1} w_i (f_i - y_i)^2 \qquad \text{is minimum.}$$

The function to be fitted is

$$f = f(x_0, \ldots\ldots x_{m-1}, \beta_0, \ldots\ldots \beta_{k-1}) = f(x, \beta)$$

where $\beta_0, \beta_1 \ldots\ldots \beta_{k-1}$ are the k adjustable parameters and $x_0, x_1, \ldots\ldots x_{m-1}$ are the m independent variables. w_i is the weight of the i^{th} data point. In the least squares procedure, the estimates $b_0, b_1 \ldots\ldots b_{k-1}$ of the parameters $\beta_0, \beta_1 \ldots\ldots \beta_{k-1}$ is obtained when

$$\frac{\partial}{\partial b_j} \sum_{i=0}^{n-1} w_i (f_i - y_i)^2 = 0$$

for all $b_j (j = 0, 1 \ldots\ldots k-1)$

All non-linear regression methods search for the absolute minimum on the ϕ surface in parameter space. Starting with certain trial parameter values, $b_0, b_1 \ldots\ldots b_{k-1}$, a correction vector, δb is calculated. The new parameter values, $b_0 + \delta b_0, b_1 + \delta b_1 \ldots\ldots b_{k-1} + \delta b_{k-1}$ are the starting values for the next iteration. The process continues until all δb_j are smaller than a certain specified value.

The curve fitting experiments described in the following sections utilized a program based on the Marquardt method [4] for non-linear least squares minimization. The advantage of the Marquardt algorithm over the Simplex algorithm [5] which was also tried initially was relatively faster convergence. The Marquardt algorithm combines the best features of two very popular methods for minimum search, viz, the Taylor expansion method and the gradient method. Taylor expansion method is most suitable in the vicinity of the minimum of ϕ, where the function, f can be linearized. The gradient method on the other hand exhibits rapid convergence far from the minimum of ϕ but is slow near the minimum. In the Marquardt algorithm, a compromise is made between the parameter corrections predicted by the two methods. In the early stage of the iterative process, the compromise criterion favours the gradient method. As the parameter values get closer to their correct values, more use is made of the Taylor series method.

1.4 Simulation of Current-Time and Current-Potential Curves

The integral equation for current given in the previous section has no analytical solution and a numerical method is required to solve it. Nicholson and Olmsted [6] have described a numerical approach for the solution of integral equations of this form that appear frequently in electrochemical theory. Before applying the numerical treatment it is convenient to normalize the current by dividing both sides of the equation by the diffusion-limited current, $i(t)_d$, given by the Cottrell equation [1]:

$$i(t)_d = \frac{nFAD_O^{\frac{1}{2}}C_O^*}{\pi^{\frac{1}{2}}t^{\frac{1}{2}}}$$

Thus,

$$\frac{i(t)\pi^{\frac{1}{2}}t^{\frac{1}{2}}}{nFAD_O^{\frac{1}{2}}C_O^*} = \frac{k^o\pi^{\frac{1}{2}}t^{\frac{1}{2}}}{D_O^{\frac{1}{2}}C_O^*}\left[C_O^* - \int_0^t \frac{i(\tau)d\tau}{nFAD_O^{\frac{1}{2}}\pi^{\frac{1}{2}}\sqrt{t-\tau}} - \int_0^t \frac{e^{-\ell((t-\tau)}i(\tau)d\tau}{nFAD_O^{\frac{1}{2}}\pi^{\frac{1}{2}}\sqrt{t-\tau}}\cdot\sqrt{\frac{D_O}{D_R}}e^{\frac{\alpha F(E-E^{o'})}{RT}}\right]$$

Multiplying both sides by $\frac{D_O^{\frac{1}{2}}\pi^{\frac{1}{2}}}{k^{o'}}$

$$\frac{i(t)\pi^{\frac{1}{2}}t^{\frac{1}{2}}}{nFAD_O^{\frac{1}{2}}C_O^*}\frac{D_O^{\frac{1}{2}}\pi^{\frac{1}{2}}}{k^{o'}} = \pi t^{\frac{1}{2}} - \int_0^t \frac{i(\tau)\pi^{\frac{1}{2}}t^{\frac{1}{2}}d\tau}{nFAD_O^{\frac{1}{2}}C_O^*\sqrt{t-\tau}} - \int_0^t \frac{e^{-\ell((t-\tau)}i(\tau)\pi^{\frac{1}{2}}t^{\frac{1}{2}}d\tau}{nFAD_O^{\frac{1}{2}}C_O^*\sqrt{t-\tau}}\cdot\sqrt{\frac{D_O}{D_R}}e^{\frac{\alpha F(E-E^{o'})}{RT}}$$

Letting,

$$\frac{i(t)\pi^{\frac{1}{2}}t^{\frac{1}{2}}}{nFAD_O^{\frac{1}{2}}C_O^*} = \frac{i(t)}{i(t)_d} = \Psi(t)$$

$$\Psi(t)\frac{D_O^{\frac{1}{2}}\pi^{\frac{1}{2}}}{k^{o'}} = \pi t^{\frac{1}{2}} - \int_0^t \frac{\Psi(\tau)d\tau}{\sqrt{t-\tau}} - \int_0^t \frac{e^{-\ell((t-\tau)}\Psi(\tau)d\tau}{\sqrt{t-\tau}}\sqrt{\frac{D_O}{D_R}}e^{\frac{\alpha F(E-E^{o'})}{RT}}$$

$\Psi(t)$ represents the normalized, dimensionless current that is independent of concentration of O and electrode surface area.
Let $t = md$, thus dividing the range of integration into m equal intervals of width, d.

$$\Psi(md)\frac{D_O^{\frac{1}{2}}\pi^{\frac{1}{4}}}{k^{o'}} = \pi(md)^{\frac{1}{4}} - \int_0^{md}\frac{\Psi(\tau)d\tau}{\sqrt{md-\tau}} - \int_0^{md}\frac{e^{-\ell(md-\tau)}\Psi(\tau)d\tau}{\sqrt{md-\tau}}\sqrt{\frac{D_O}{D_R}}e^{\frac{nF(E-E^{o'})}{RT}}$$

Assuming the function to be a constant (zero order polynomial) and equal to b_i (i=1,2,....m) in each interval (figure 1.1), the integrals can be written as summations. The procedure as described by Nicholson and Olmsted is a special case of Huber's method [7] where, in general, the function to be evaluated is approximated by connected line segments on the integration subintervals.

$$b_m\frac{D_O^{\frac{1}{2}}\pi^{\frac{1}{4}}}{k^{o'}} = \pi(md)^{\frac{1}{4}} - \sum_{i=1}^{m} b_i\int_{(i-1)d}^{id}\frac{d\tau}{\sqrt{md-\tau}} - \sum_{i=1}^{m} b_i\int_{(i-1)d}^{id}\frac{e^{-\ell(md-\tau)}d\tau}{\sqrt{md-\tau}}\sqrt{\frac{D_O}{D_R}}e^{\frac{nF(E-E^{o'})}{RT}}$$

The integrals are simplified by the change of variables, $md-\tau = y$

$$b_m\frac{D_O^{\frac{1}{2}}\pi^{\frac{1}{4}}}{k^{o'}} = \pi(md)^{\frac{1}{4}} - \sum_{i=1}^{m} b_i\int_{(m-i)d}^{(m-i+1)d}\frac{dy}{\sqrt{y}} - \sum_{i=1}^{m} b_i\int_{(m-i)d}^{(m-i+1)d}\frac{e^{-\ell y}dy}{\sqrt{y}}\sqrt{\frac{D_O}{D_R}}e^{\frac{nF(E-E^{o'})}{RT}}$$

Substituting $\ell y = z$ and $dy = dz/\ell$ and multiplying both sides by $\ell^{\frac{1}{2}}$

$$b_m\frac{D_O^{\frac{1}{2}}\pi^{\frac{1}{4}}\ell^{\frac{1}{2}}}{k^{o'}} = \pi(md\ell)^{\frac{1}{4}} - \sum_{i=1}^{m} b_i\int_{(m-i)d\ell}^{(m-i+1)d\ell}\frac{dz}{\sqrt{z}} - \sum_{i=1}^{m} b_i\int_{(m-i)d\ell}^{(m-i+1)d\ell}\frac{e^{-z}dz}{\sqrt{z}}\sqrt{\frac{D_O}{D_R}}e^{\frac{nF(E-E^{o'})}{RT}}$$

Defining $s1_k = \int_{(k-1)d\ell}^{kd\ell} \frac{1}{\sqrt{z}} dz = 2\sqrt{d\ell}\left(\sqrt{k} - \sqrt{k-1}\right)$ (1.3)

and $s2_k = \int_{(k-1)d\ell}^{kd\ell} \frac{e^{-z}}{\sqrt{z}} dz = \sqrt{\pi}\left\{erf\left(\sqrt{kd\ell}\right) - erf\left(\sqrt{(k-1)d\ell}\right)\right\}$, (1.4)

the above equation can be written as

$$b_m \frac{D_O^{\frac{1}{2}} \pi^{\frac{1}{2}} \ell^{\frac{1}{2}}}{k^{o'}} = \pi (md\ell)^{\frac{1}{2}} - \sum_{i=1}^{m} b_i s1_{m-i+1} - \sum_{i=1}^{m} b_i s2_{m-i+1} \sqrt{\frac{D_O}{D_R}} e^{\frac{nF(E-E^{\circ})}{RT}}$$

Separating b_m from the two summations:

$$b_m \frac{D_O^{\frac{1}{2}} \pi^{\frac{1}{2}} \ell^{\frac{1}{2}}}{k^{o'}} = \pi (md\ell)^{\frac{1}{2}} - b_m s1_1 - \sum_{i=1}^{m-1} b_i s1_{m-i+1}$$

$$-b_m s2_1 \sqrt{\frac{D_O}{D_R}} e^{\frac{nF(E-E^{\circ})}{RT}} - \sqrt{\frac{D_O}{D_R}} e^{\frac{nF(E-E^{\circ})}{RT}} \sum_{i=1}^{m-1} b_i s2_{m-i+1}$$

Isolating b_m:

$$b_m\left\{\frac{D_O^{\frac{1}{2}}\pi^{\frac{1}{2}}\ell^{\frac{1}{2}}}{k^o}+s1_1+s2_1\sqrt{\frac{D_R}{D_O}}e^{\frac{nF(E-E^o)}{RT}}\right\}=\pi(md\ell)^{\frac{1}{2}}-\sum_{i=1}^{m-1}b_i s1_{m-i+1}$$

$$-\sqrt{\frac{D_O}{D_R}}e^{\frac{nF(E-E^o)}{RT}}\sum_{i=1}^{m-1}b_i s2_{m-i+1} \qquad (1.5)$$

Equation (1.5) is used to calculate the value of the function b_m in each of the m intervals, starting with the b_1 in the first interval.

1.5 Analysis of Simulated Current-Time (i-t) Curves

Figure 1.2 shows current-time curves simulated at various applied potentials. The current function is the normalized current obtained by dividing the current at each point in time by the diffusion limited current at the same point in time. The diffusion-limited current decays faster than current controlled by kinetics. The normalized current therefore increases with time as in figure 1.2 [8]. As the applied potential is varied from -1.40 volts to -1.55 volts in steps of -0.025 volts, the normalized current increases and eventually reaches the theoretical maximum of unity.

Figure 1.3 shows the effect of varying the electron transfer rate constant, on the simulated current vs time data. k^o is increased by a factor of five, from one curve to the next and the current function is seen to increase progressively until a limiting value is reached. The limiting value of the current function does not reach unity in this case, unlike the data presented in figure

1.2. This is because the applied potential, -1.45 volts is 50 mv positive, relative to the $E^{o'}$ used in the simulation.

The influence of the transfer coefficient, α, on the current-time curves is shown in figures 1.4a and 1.4b. When the potential on the electrode is changed from zero (on any arbitrary scale) to E, the energy of the electrons inside the electrode changes by -nFE. The resulting change in the activation energy for reduction is αnFE and that for oxidation is -(1-α)nFE. When α is 0.1 a negative voltage(-E) applied on the electrode will decrease the activation energy for reduction by 0.1nFE and increase that for oxidation by 0.9nFE. When α is 0.9 the changes will be 0.9nFE for reduction and 0.1nFE for oxidation. What value of α will result in more current, therefore, depends on which redox form of the molecule is predominant at the electrode surface. In figure 1.4a, the applied potential is more negative than Eo. The predominant species is the reduced form. This explains the larger current for α=0.1. In figure 1.4b the applied potential is on the positive side of Eo. The oxidized form is in excess and the effect of α on the current is reversed.

The effect of varying the rate of the following chemical step on the current - time curves is shown in figure 1.5. The k_f-values less than 1.0 did not have any effect on the current-time curves. These values of k_f are too low to compete with the reversible electron transfer rate for control of the overall conversion from O to R. The value of k_f varies from 1.0 s^{-1} to the very fast rate of 10^6 s^{-1}. As k_f is increased the current increases and eventually becomes close to the diffusion limited current. The value of E, -1.45 volts, is 50 millivolts positive to the standard redox potential used in the simulation. The following chemical step removes the reduction product from the vicinity of the electrode quickly. To maintain the Nernstian equilibrium, more of the oxidized form has to convert to the reduced form. This conversion

can become diffusion controlled, even at potentials on the positive side of E^o, if the heterogeneous reaction rate is reversible and the homogeneous reaction is fast enough. An interesting limiting case would be one in which both the electron transfer and the following reaction are extremely fast. Figure 1.6 shows a current-time simulation using a value of 1.0 for k^o and a value of 10^6 for k_f. Though the applied potential is on the positive side of $E^{o'}$, the current reaches the diffusion limited value even at very short times.

1.6 Analysis of Simulated Current-Voltage (i-E) Curves

Equation 1.5 was used to simulate current vs voltage (i-E) curves in a manner analogous to simulation of i-t curves, described in the previous section. A typical simulation is shown in figure 1.7 along with a list of the parameter values used. While the i-t curves can be considered as the simulation of chronoamperometry, the i-E curves are the counterpart in simulation of normal pulse polarography (NPP). The i-E curve does have the shape of a normal pulse polarogram. The normalized current function is zero far from $E^{o'}$ on the positive side. Beyond $E^{o'}$ on the negative side it reaches the limiting value of unity as expected.

The effect of varying the heterogeneous rate constant on the i-E curves is shown in figure 1.8. As the electron transfer rate increases the curves shift to the positive direction. The rising portion of the i-E curve, i.e., the range in voltage over which the current function goes from zero to one, gets smaller and eventually reaches a limit when electron transfer becomes reversible.

Figure 1.9 shows the effect of varying the rate of the homogeneous reaction following reversible electron transfer. As

the rate constant is increased the i-E waves shift towards positive voltages and reaches a limit when k_f is 10^9. On the other extreme, values of k_f less than 1.0 have no effect on the i-E curves. Effect of k_f on i-E curves depends on the values of other parameters, especially k^o as shown in figures 1.10 a-c. For large values of k^o, the only effect of increasing k_f is a shift in position of the curve and is thus indistinguishable from a change in E^o (figure 1.10a). For smaller values of k^o, the shift in position of the curve is less but there is also a change in the shape of the curve (figures 1.10b-c). The effect of a large k_f, in this case is similar to the combined effect of a slower electron transfer rate and a more positive E^o.

The simulated current-time and current-voltage curves in figures 1.2 to 1.10 are well in agreement with theoretical prediction as well as documented behavior of real systems. The simulation experiments further show how the two rate constants, k^o and k_f and the standard redox potential, $E^{o'}$ are correlated, suggesting that resolving these parameters may not be straightforward.

1.7 Accessible Rate Constants and Kinetic Zones

Rates of chemical reactions following electron transfer are often measured by either cyclic voltammetry or double-step chronoamperometry. These techniques rely on following a disappearing species during the reverse scan or step. Species whose half-life is much less than the reversal time realizable under conditions of the experiment cannot be observed. This limitation should not apply to the curve-fitting procedure described in this chapter. The theory developed here is for potential-dependent chronoamperometry and involves no reverse step. However, there are theoretical limits on measurable rate constants in different kinetic regions as described below. These limits are set by the competition between the electron-transfer

reaction, the following chemical reaction, and the diffusion of the reactants and products to and from the electrode surface. To determine these limits the digitized current-time equation (equation 1.5) derived in section 1.4 was analyzed as described below.

Replacing $S1_k$ and $S2_k$ by their respective definitions (equations 1.3 and 1.4) and letting $\theta = \sqrt{D_O/D_R}\, e^{nF(E-E^{o'})/RT}$, equation 1.5 can be written as follows:

$$b_m = \left[\pi(md\ell)^{\frac{1}{2}} - 2\sqrt{d\ell}\sum_{i=1}^{m-1} b_i\left(\sqrt{m-i+1}-\sqrt{m-i}\right) - \theta\pi^{\frac{1}{2}}\sum_{i=1}^{m-1} b_i\left\{erf\left(\sqrt{(m-i+1)d\ell}\right) - erf\left(\sqrt{(m-i)d\ell}\right)\right\}\right] \Bigg/ \frac{D_O^{\frac{1}{2}}\pi^{\frac{1}{2}}\ell^{\frac{1}{2}}}{k^{o'}} + 2\sqrt{d\ell} + \theta\pi^{\frac{1}{2}} erf\left(\sqrt{d\ell}\right)$$

It is more instructive to write this equation in terms of the following dimensionless rate constants:

$$\Lambda = \frac{k^{o'}\sqrt{d}}{\sqrt{D_O}}$$

and $$\lambda = d\ell$$

The resulting equation is:

$$b_m = \left[\pi(m\lambda)^{\frac{1}{2}} - 2\sqrt{\lambda}\sum_{i=1}^{m-1} b_i\left(\sqrt{m-i+1}-\sqrt{m-i}\right) - \theta\pi^{\frac{1}{2}}\sum_{i=1}^{m-1} b_i\left\{erf\left(\sqrt{(m-i+1)\lambda}\right) - erf\left(\sqrt{(m-i)\lambda}\right)\right\}\right] \Bigg/ \frac{\pi^{\frac{1}{2}}\lambda^{\frac{1}{2}}}{\Lambda} + 2\lambda^{\frac{1}{2}} + \theta\pi^{\frac{1}{2}} erf\left(\lambda^{\frac{1}{2}}\right)$$

Dividing the numerator and denominator by $\lambda^{\frac{1}{2}}$

$$b_m = \left[\pi(m)^{\frac{1}{2}} - 2\sum_{i=1}^{m-1} b_i\left(\sqrt{m-i+1}-\sqrt{m-i}\right) - \frac{\theta\pi^{\frac{1}{2}}}{\lambda^{\frac{1}{2}}}\sum_{i=1}^{m-1} b_i\left\{erf\left(\sqrt{(m-i+1)\lambda}\right) - erf\left(\sqrt{(m-i)\lambda}\right)\right\}\right] \Bigg/ \frac{\pi^{\frac{1}{2}}}{\Lambda} + 2 + \frac{\theta\pi^{\frac{1}{2}}}{\lambda^{\frac{1}{2}}} erf\left(\lambda^{\frac{1}{2}}\right) \qquad (1.6)$$

The use of dimensionless parameters, Λ and λ will yield results of the most general nature, compactly displaying the characteristics of the system in all time-windows. To get dimensioned profiles at any given time one only needs to multiply Λ by $\sqrt{D_o/d}$ and λ by $1/d$.

The limiting behaviors of the above equation obtained when Λ and λ assume extreme values are considered below.

1. $\Lambda \to \infty$ (Reversible Electron Transfer with Chemical Step)

The first term in the denominator drops out and equation 1.6 becomes:

$$h_m = \left[\pi(m)^{\frac{1}{2}} - 2\sum_{i=1}^{m-1} h_i\left(\sqrt{m-i+1} - \sqrt{m-i}\right) - \frac{\theta\pi^{\frac{1}{2}}}{\lambda^{\frac{1}{2}}} \sum_{i=1}^{m-1} h_i \left\{ erf\left(\sqrt{(m-i+1)\lambda}\right) - erf\left(\sqrt{(m-i)\lambda}\right)\right\}\right] \Big/ \left(2 + \frac{\theta\pi^{\frac{1}{2}}}{\lambda^{\frac{1}{2}}} erf\left(\lambda^{\frac{1}{2}}\right)\right) \qquad (1.7)$$

The boundary of this region was mapped (figure 1.11) by calculating values of parameters Λ and λ for which the denominators of equations 1.6 and 1.7 are nearly equal (within 2%).

$$\text{i.e.,} \quad \frac{2 + \frac{\theta\pi^{\frac{1}{2}}}{\lambda^{\frac{1}{2}}} erf\left(\lambda^{\frac{1}{2}}\right)}{\frac{\pi^{\frac{1}{2}}}{\Lambda} + 2 + \frac{\theta\pi^{\frac{1}{2}}}{\lambda^{\frac{1}{2}}} erf\left(\lambda^{\frac{1}{2}}\right)} = 0.98$$

2. $\lambda \to 0$ (Quasi-Reversible Electron Transfer)

Equation 1.6 becomes:

$$b_m = \frac{\pi(m)^{\frac{1}{2}} - 2\sum_{i=1}^{m-1} b_i\left(\sqrt{m-i+1} - \sqrt{m-i}\right) - 2\theta\sum_{i=1}^{m-1} b_i\left(\sqrt{m-i+1} - \sqrt{m-i}\right)}{\frac{\pi^{\frac{1}{2}}}{\Lambda} + 2 + 2\theta}$$

$$\left(\textit{Note: } erf(x) \approx \frac{2x}{\sqrt{\pi}} \textit{ for } x << 1\right)$$

The boundary of this region was mapped (figure 1.12) as in the previous case by solving the following equation for Λ at various values of λ.

$$\frac{\frac{\pi^{\frac{1}{2}}}{\Lambda} + 2 + \frac{\theta\pi^{\frac{1}{2}}}{\lambda^{\frac{1}{2}}} erf\left(\lambda^{\frac{1}{2}}\right)}{\frac{\pi^{\frac{1}{2}}}{\Lambda} + 2 + 2\theta} = 0.98$$

3. $\lambda \to \infty$ (Irreversible Electron Transfer)

Equation 1.6 becomes:

$$b_m = \frac{\pi(m)^{\frac{1}{2}} - 2\sum_{i=1}^{m-1} b_i\left(\sqrt{m-i+1} - \sqrt{m-i}\right)}{\frac{\pi^{\frac{1}{2}}}{\Lambda} + 2}$$

This region (figure 1.13) was mapped by solving the following equation:

$$\frac{\frac{\pi^{\frac{1}{2}}}{\Lambda}+2}{\frac{\pi^{\frac{1}{2}}}{\Lambda}+2+\frac{\theta\pi^{\frac{1}{2}}}{\lambda^{\frac{1}{2}}}erf\left(\lambda^{\frac{1}{2}}\right)}=0.98$$

In figure 1.14, the three limiting regions considered above are drawn in the same log(λ)-log(Λ) space dividing the entire region into several kinetic zones. These regions are essentially the same as in the zone diagram for the EC reaction scheme derived from cyclic voltammetric theory [9]. Listed in parentheses in each zone of figure 1.14, are the parameters that control the current in that region. According to this theory, it should be possible to evaluate the parameters listed in a region from experimental data acquired from the same region. Data for figure 1.14 were calculated for applied potential, E, equal to $E^{o'}$, the standard potential. If the value of applied potential is changed, the zones in the diagram could shift, as shown in figures 1.15 and 1.16. Apart from displaying the relationship of measured current and the parameters, the zone diagrams can aid in selecting data for analysis that contain the most information about the system. The diagram also shows the limiting values of parameters theoretically accessible . For instance, in figure 1.14, the region labelled 'Quasi-rev. ET with chem. step' represents the regime where current is controlled by all four parameters. At log(Λ)=0, the smallest and largest values of log(λ) that fall in this region are -0.75 and 2.5. This value of Λ will translate to a $k^{o'}$ of 0.01 cm s^{-1} when d is 10 milliseconds and D is 10^{-6} cm^2 s^{-1}. The values of k_f will be 18, for log(λ) = -0.75 and 3.2×10^4 for log(λ)=2.5. These values represent the smallest and largest rate constants for the following chemical reaction, measurable when $k^{o'}$ is 0.01 cm s^{-1}. The upper limit of k_f that could be evaluated by fitting simulated i-E-t data was

5×10^4 s^{-1}, for $k^{o'}$=0.01 cm s^{-1} and this value is in good agreement with the prediction based on the zone diagram.

1.8 Fitting current-time and current-voltage curves

The feasibility of simultaneously determining the four parameters was explored at first with data simulated using equation (1.5). Since simulated data are free of noise and other experimental errors, the curve-fitting program should converge on the same parameter values that were used to simulate the data set. Data presented in table 1.1 are typical of the results obtained in a large number of attempts to fit i-E data. The value of the experimental variable, time, used in the simulation is given in the first column. The next four columns contain the parameter values after convergence, with the true values listed in parenthesis. The last column is the sum of squares of residuals, Φ. In most cases, except for $E^{o'}$, the fitted values are considerably different from those used in the simulation. Yet, the sum of squares of residuals is very small. The same observation can be made from the results of fitting i-t data, shown in table 1.2. The time window in which current-time data was simulated is given in the first column. The remaining entries are same as in table 1.1. It is quite evident that the values of the four parameters that can generate a given i-E or i-t curve are not unique. The optimization program seems to compensate for the error in a given parameter by adjusting the other parameter(s). This adjustment of parameters resulting in non-unique values is further examined in the following study using simulated i-E data.

Three i-E curves were simulated at 0.1, 1.0 and 10 milliseconds. The adjustable parameters were same for all three curves. These curves were fitted to see how the same error in one parameter, viz, k^o will be compensated for by adjusting k_f. Thus α

and E^o were held constant at their true values while k^o was held at values different from the true value. The only parameter to be freely adjusted was k_f. The results are summarized in table 1.3. An interesting observation to be made here is that the optimizing program adjusted the value of k_f by a different amount for each curve, in order to correct for the same error in k^o. For instance, the first row in table 1.3 shows that k_f had to be increased by 562 to compensate for an error of 0.01 in k^o to fit an i-E curve simulated at 10^{-4} second. As shown in the fifth row, the same error in k^o is corrected by increasing k_f by 55, at 10^{-2} second. This result is not entirely unexpected considering the fact that the effect of kinetic parameters such as k^o and k_f on current depends on their magnitudes and also the time window of measurement. Nevertheless, this observation did provide the clue to a different approach for the extraction of parameters from the measured current. Suppose the three i-E curves were fitted simultaneously. The fitted parameters for individual i-E curves will not fit the data set made up of the three curves taken together. This is due to the fact that the adjustment required to compensate the error in a parameter is different for each curve. The optimizing program, in seeking parameter values that fit all the curves simultaneously, has a better chance of converging on the true values. The following section describes this approach applied to simulated data.

1.9 Fitting current-voltage-time surface

Several current-voltage curves, each recorded at different sampling times, constitute a current-voltage-time (i-E-t) surface. An equivalent concept would be several current-time curves recorded at different voltages. That fitting an i-E-t surface in three dimension is a viable approach for the simultaneous evaluation of all the four parameters is demonstrated in the following experiment.

Consider the domain of voltage and time defined by the plane surface shown in figure 1.17. The twenty five points of intersection on the grid represent twenty five points in time and voltage spread evenly across this E-t surface. The normalized current at these twenty five points was simulated. Experimentally such a data set could be formed by taking five points each from five current-voltage curves recorded at sampling times 0.15, 0.40, 0.65, 0.90 and 1.15 millisecond or equivalently by taking five points each from five current-time curves at voltages, -1.51, -1.56, -1.61, -1.66 and -1.71 volts. Table 1.4 contains the result of fitting this simulated i-E-t surface along with results obtained by fitting i-t and i-E curves from the same time-voltage domain. The first five entries are for i-t curves at -1.51, -1.56, -1.61, -1.66 and -1.71 volts followed by five i-E curves at 0.15, 0.40, 0.65, 0.90 and 1.15 millisecond. Each i-t and i-E curve is made up of 25 points. The last entry is for the i-E-t surface and is the only instance where all the converged values are same as those used in the simulation. A 3D-graph of the i-E-t data corresponding to the last entry in table 1.4 is shown in figure 1.18, with more points added for better definition of the surface.

1.10 Application of i-E-t surface analysis to study the electrochemistry of methyl cobalamin

There has been great interest in the chemistry of vitamin B_{12} since it was discovered in the 1920's as a cure for pernicious anemia and isolated in 1948 independently by Folkers and co-workers [10] and by Smith and Parker [11,12]. The enzymatic reactions catalyzed by vitamin B_{12} are accompanied by changes in the oxidation state of the cobalt atom in the vitamin. This provided the impetus for the vast amount of existing literature on the electrochemical reactions of vitamin B_{12} and related compounds.

Earlier work using polarographic techniques [13-20] produced several conflicting reports, most of the inconsistency being the result of adsorption of the compounds on the mercury electrode. Later, other techniques including cyclic voltammetry [21,22], potentiometry [22,23] and controlled potential coulometry [24-26] were used to study vitamin B_{12} derivatives and model compounds. More recently, several systematic investigations into the thermodynamics and kinetics of electrode reactions of vitamin B_{12} have been reported [27-36] by different laboratories. These attempts have unravelled some of the complexities deriving from the interplay of electron transfer and changes in axial ligation in the chemistry of vitamin B_{12} derivatives. That several questions remain unanswered regarding the role of vitamin B_{12} in biochemical reactions is hardly surprising in view of the highly complex nature of its redox chemistry.

The structure of vitamin B_{12}, the most complex naturally occurring non-polymeric molecule, is shown in figure 1.19. The form of vitamin B_{12} represented in the figure is referred to as cyanocobalamin, cyanocob(III)alamin or less commonly, 5,6-dimethylbenzimdazolylcyanocobamide. The coenzyme forms of vitamin B_{12} are obtained when the cyanide group in the axial position is replaced by some other residue, typically 5'-deoxyadenosyl or methyl groups. Biochemical reactions catalyzed by these coenzymes are known to occur via dissociation and reformation of the carbon-cobalt bond in the axial position, which was the first organometallic bond found to occur in nature [37]. For instance, methyl cobalamin in its reduced form is involved in the transfer of a methyl group from methyl-tetrahydrofolic acid to homocysteine in the biosynthesis of methionine [38]. The exact mechanism of this reaction sequence is not known at present and there is a great deal of interest in understanding factors that cause the Co-C bond to cleave and reform [21,39,40].

In vitro reduction of alkyl cobalamins is followed by dissociation of the Co-C bond. Spectroelectrochemical studies [31,32] have shown that the product formed on reduction of methyl and adenosyl cobalamins at -1.5 volts is cob(I)alamin, also known as vitamin B_{12s}. GC-MS studies [40] indicate that ethane is greater than 97% of the product of the reduction of methyl cobalamin, suggesting that the leaving group is a methyl radical. The number of electrons involved in the reduction step, as determined by controlled-potential coulometry at -1.5 volts was one for both methyl and adenosyl cobalamins [41,42]. Based on these and other evidence, the electroreduction of alkyl cobalamins can be represented by the following EC mechanism:

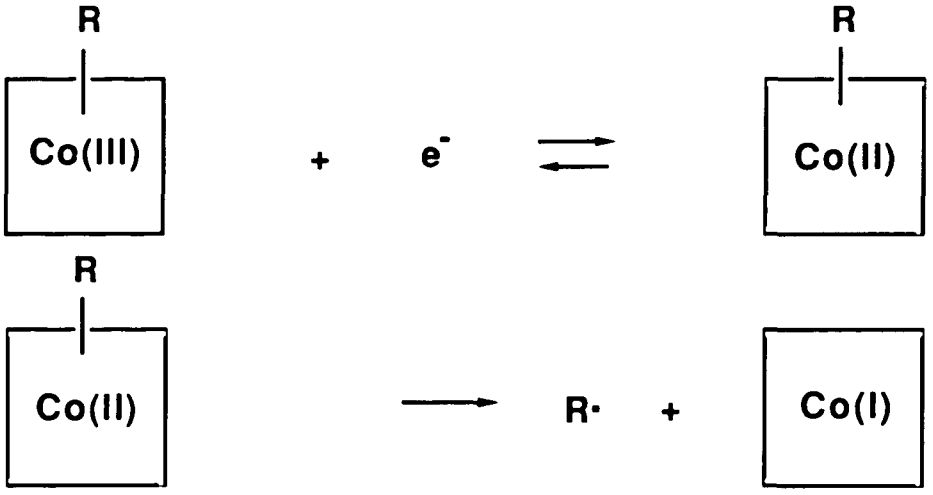

The kinetics of this dissociation step can vary over a wide range depending on the environment. In aqueous media the rate constant for dissociation is as low as $0.37s^{-1}$ [43]. In nonaqueous media where solvation effects stabilize the methyl radical, the rate constant was reported to be $1.2x10^{2}s^{-1}$ at -30 °C [33].

Analysis of current-time-voltage surface, as described in the previous sections, was applied to study methyl cobalamin in

dimethyl sulfoxide (DMSO) solvent. DMSO offers a fairly wide potential window, from 0.0 to -2.0 volts, vs saturated calomel electrode (SCE). Also the electrode process is not complicated by adsorption of the molecule on the electrode surface in DMSO. DC and normal pulse polarograms of methyl cobalamin in DMSO (figures 1.20 and 1.21) show well defined reduction waves at 1.51 volts. The polarograms were recorded in de-oxygenated solutions using a Tacussel pulse polarograph. Cyclic voltammetry of methyl cobalamin in the same solvent is shown in figure 1.22. There is a reduction peak at -1.55 volts corresponding to the reduction waves in the polarograms. The absence of a reoxidation peak on reverse scan is due to the fast chemical reaction following electron transfer.

The experimental set-up used to record the i-E-t surface is shown in figure 1.23. The electrochemical cell, protected from light (methyl cobalamin is light sensitive.) contains 10^{-3}M methyl cobalamin in DMSO with 0.1M tetrabutyl ammonium perchlorate as supporting electrolyte. The solution is maintained oxygen-free by bubbling nitrogen through a fine glass frit. A mercury drop suspended from the recessed tip of a platinum wire fused inside glass serves as the working electrode. A saturated calomel reference electrode and a platinum counter electrode complete the three-electrode cell. The wave form generator outputs the programmed wave form. The Wenking potentiostat applies this voltage on the electrodes in the cell. At first the potential of the working electrode is held where no reaction takes place. A voltage pulse is then applied to the rising part of the i-E curve shown in figure 1.20. The current-time response is collected and stored in a Nicolet storage oscilloscope. The experiment is repeated at various pulse heights, covering the entire i-E curve from the base line to the diffusion limited region. This collection of i-t curves recorded for different values of applied potential(E) constitute an i-E-t surface. The current-time curves were divided

by the diffusion-limited current to generate the normalized i-E-t surface. To record the diffusion-limited current the voltage was stepped to the plateau of the i-E curve. Figure 1.24 shows the normalized current-voltage-time surface that was fitted to the theoretical equation. Table 1.5 contains a summary of the parameter estimation for methyl cobalamin in DMSO.

1.11 Discussion

The estimated values of the four parameters in five experiments are listed in table 1.5. Below the fitted value of each parameter are the upper and lower bounds of the parameter as estimated by the curve-fitting routine. These error estimates are formed by taking the product of the standard deviation of the data points and the square root of the diagonal elements of the error matrix. The estimated errors seem to be higher than realistic and is probably due to the noise in experimental data. The experimental current-voltage-time surface is not very smooth as seen in figure 1.24. In fact, a memorandum [44] explaining the interpretation of the error estimates made by the program does caution users about much larger estimated errors than warranted by the precision of the data. One possible source of large error estimates mentioned in the memorandum is noise in the experimental data points.

The effect of the noise level on the estimated error, was studied by fitting data with and without noise. Table 1.6 shows the parameter values and error estimates obtained by fitting a simulated (noise free) i-E-t surface. Random numbers were generated on a computer in the range, 0 to $\pm$ 2.5 % of the average magnitude of the simulated data. By adding these numbers to the simulated data, a noisy i-E-t surface was generated. Parameters and their bounds obtained by fitting this surface are also shown in table 1.6. Introducing the noise only changed the estimated value

of the parameters slightly but the error estimates are very large as with the experimental data.

It seems more reasonable to calculate the standard deviation in the parameter estimates from repeated experiments. The average values and the standard deviations of the parameters based on the five experiments listed in table 1.5 are as follows: $\alpha = 0.552 \pm 0.004$; $k^o = 0.0052 \pm 0.0005$; $k_f = 1500 \pm 140$; $E^{o'} = -1.54 \pm 0.01$.

The role of methyl cobalamin in the biosynthesis of methionine is of considerable interest to biochemists. The mechanism of this reaction and the role played by methyl cobalamin has been an area of lively controversy for the last few decades [45, 46]. Data from electrochemical studies, mainly redox potential measurements have been used to support or dispute suggested mechanisms [36,47]. Methyl cobalamin is involved in the final step, viz., transfer of a methyl group from methyl-tetrahydrofolate to homocysteine, forming methionine. According to the reaction scheme (figure 1.25) considered most probable [46,47,48,49], cobalamin bound to the enzyme methionine synthase is converted to methylcobalamin by transfer of a methyl group from S-adenosylmethionine. This constitutes the activation step and is followed by the catalytic cycle in which a methyl group is transferred from methyl cobalamin to homocysteine. The methyl cobalamin is then regenerated by transfer of a methyl group from methyl-tetrahydrofolate. Experimental evidence including retention of configuration at the carbon atom of the methyl group [50] and pH dependence studies [51] suggests that the transfer of methyl group occurs via the classical S_N2 mechanism. However, since the reduction of methylcobalamin is known to be followed by heterolytic dissociation of the carbon-cobalt bond, an alternate pathway involving transfer of a methyl radical could be considered. In this context, the large negative $E^{o'}$

measured in the present study indicates that a reductive methyl radical transfer mechanism would be very unfavorable energetically. This would be indirect support for the proposed nucleophilic substitution in the catalytic cycle.

In conclusion, analysis of data in three dimensions, allowing a more complete characterization of the redox process should lead to a better understanding of biological processes involving vitamin B_{12} and other molecules. Simultaneous measurement of the four parameters, not requiring prior knowledge of any one, is clearly a major advantage of this approach. The method could easily be extended to other electrode mechanisms.

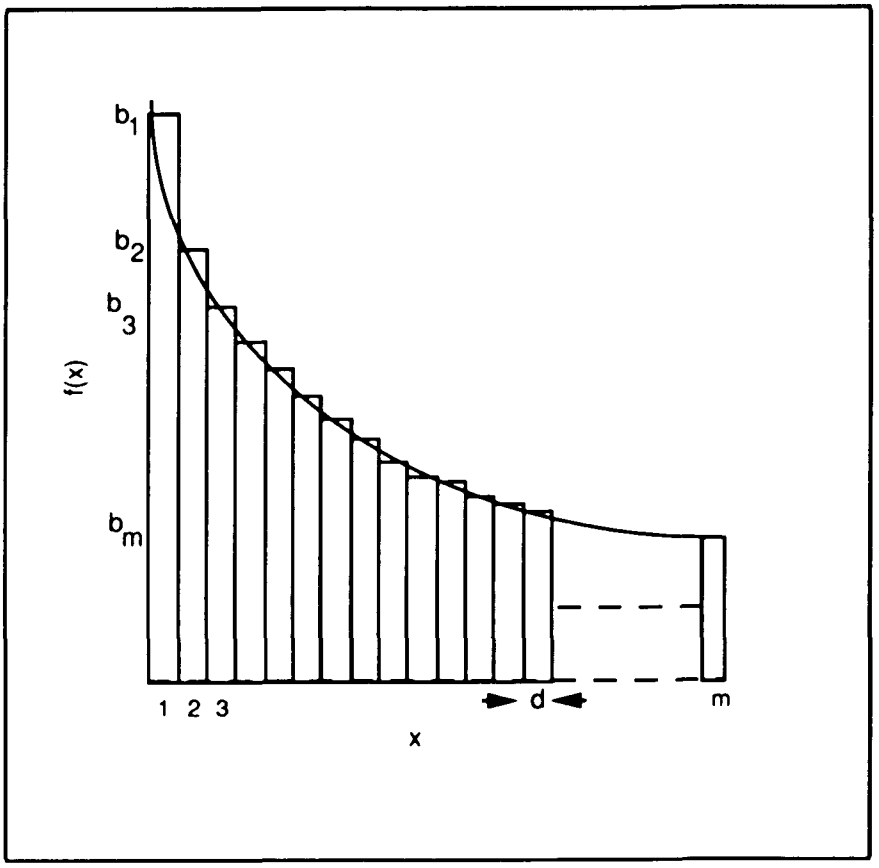

figure 1.1

Step Function method: The function to be evaluated, f(x) is approximated by a constant in each of the m intervals into which the range of integration is divided.

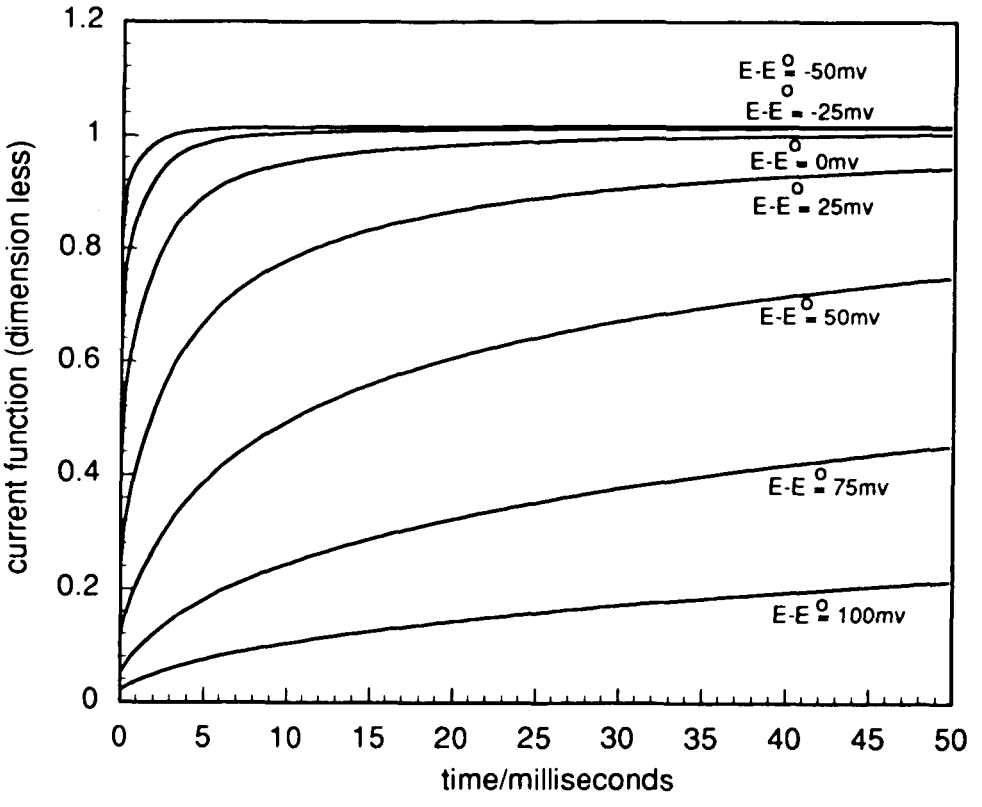

Figure 1.2 Normalized current simulated at various applied potentials. $\alpha = 0.5$, $k^{\circ} = 0.5$cm sec^{-1} $E^{\circ} = -1.5$volts, $k_f = 1000$ sec^{-1}

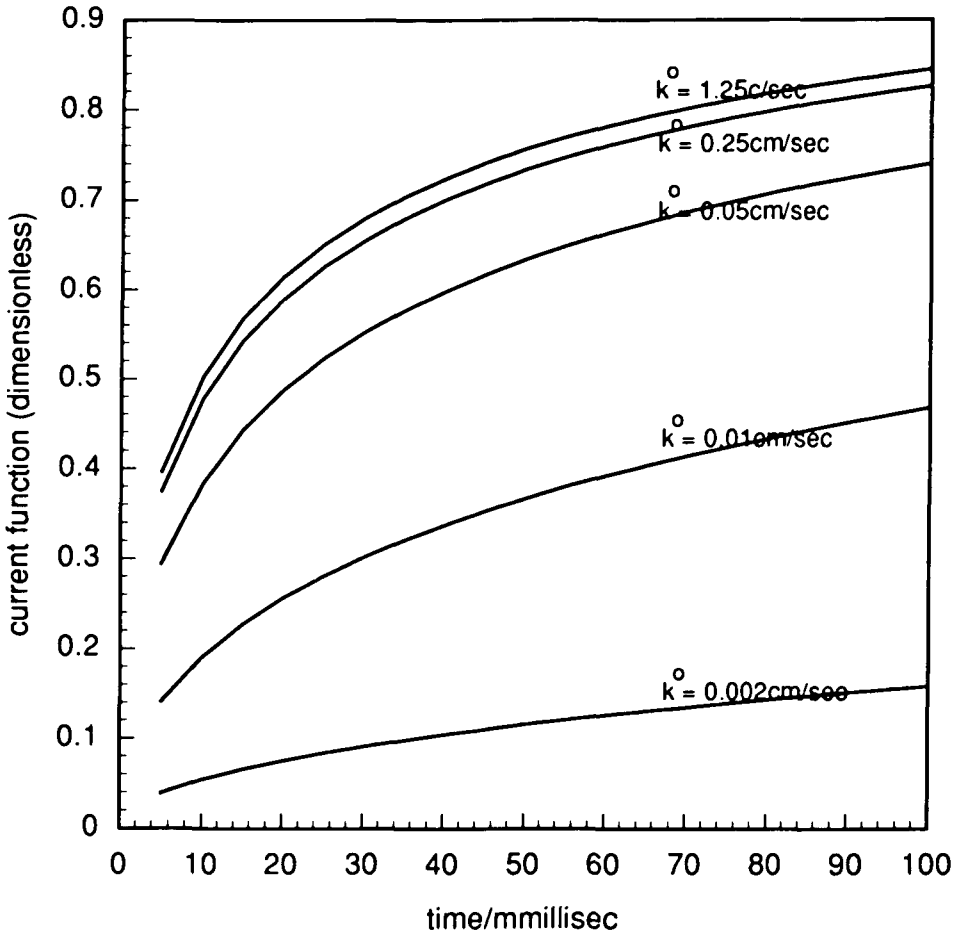

Figure 1.3 Normalized current simulated at various electron transfer rates. $\alpha = 0.5$, $E^{\circ} = -1.5$volts, $E = -1.45$volts, $k_f = 1000\ sec^{-1}$

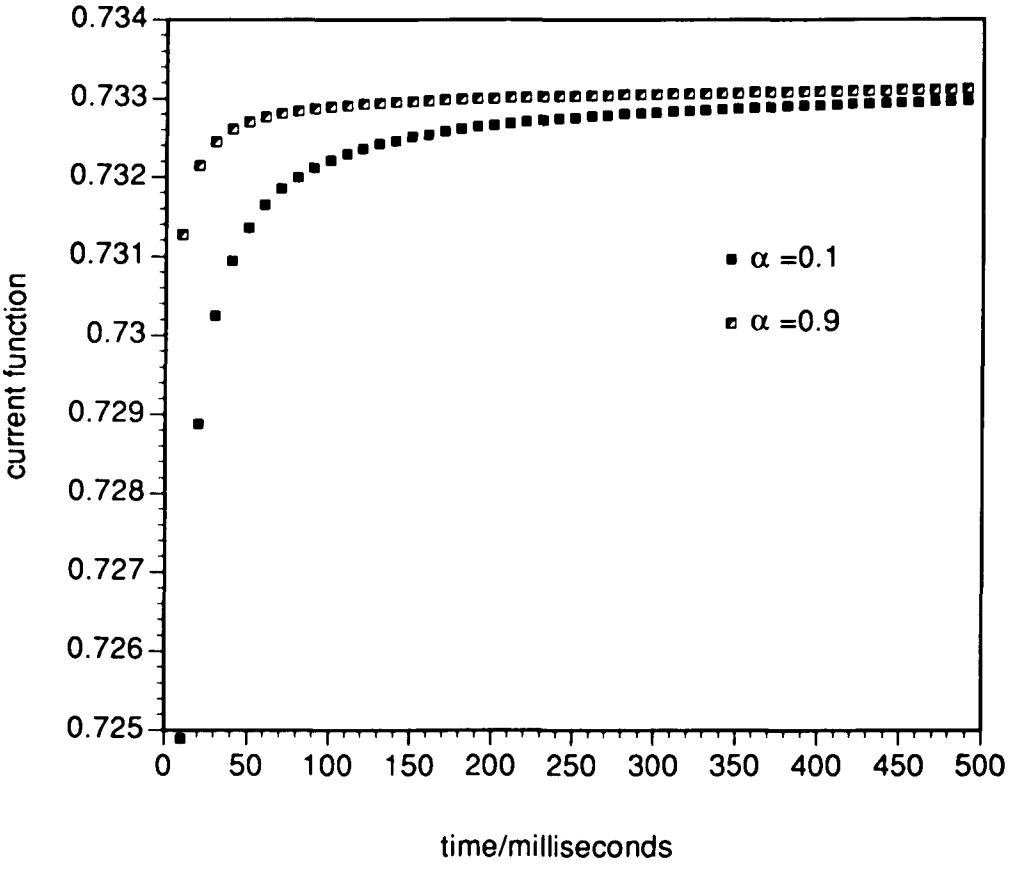

Figure 1.4a Effect of α on current-time curves when applied voltage is more negative than E°. $k^{\circ} = 0.1$, $k_f = 0.001$, $E^{\circ} = -1.5$ volts, $E = -1.525$ volts

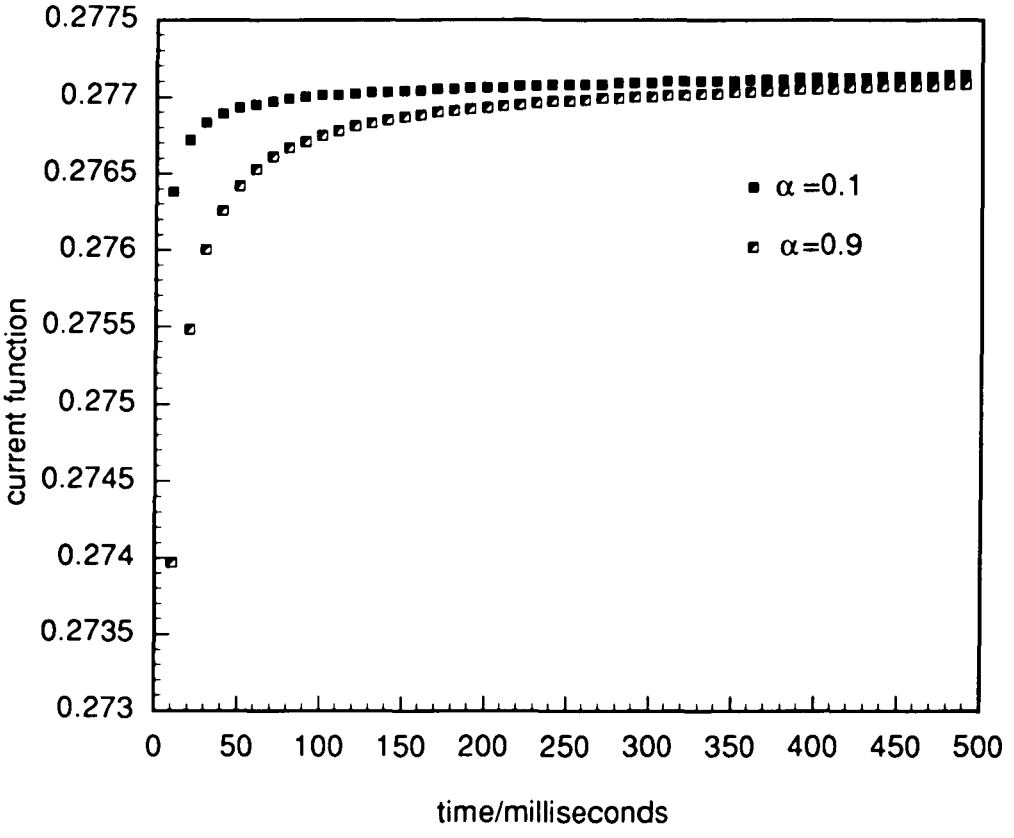

Figure 1.4b Effect of α on current-time curves when applied voltage is more positive than E^{o}. k^{o}= 0.1, k_f= 0.001, E^{o}= -1.5 volts, E = -1.475 volts

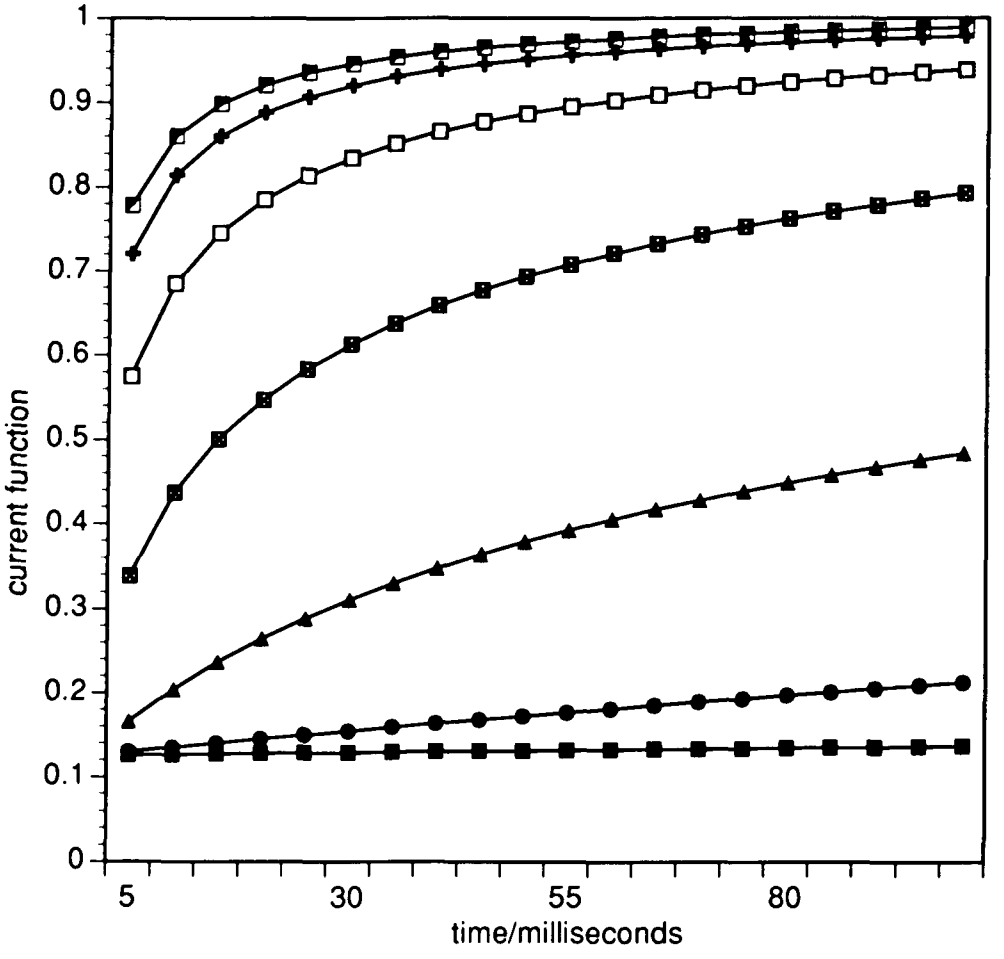

figure 1.5

Normalized current at various values of k_f. α=0.5, k^o=0.1, E^o=-1.5v, E=-1.45v

$k_f=10^0$; $k_f=10^2$; $k_f=10^4$; $k_f=10^5$; $k_f=10^6$;

$k_f=10^1$; $k_f=10^3$

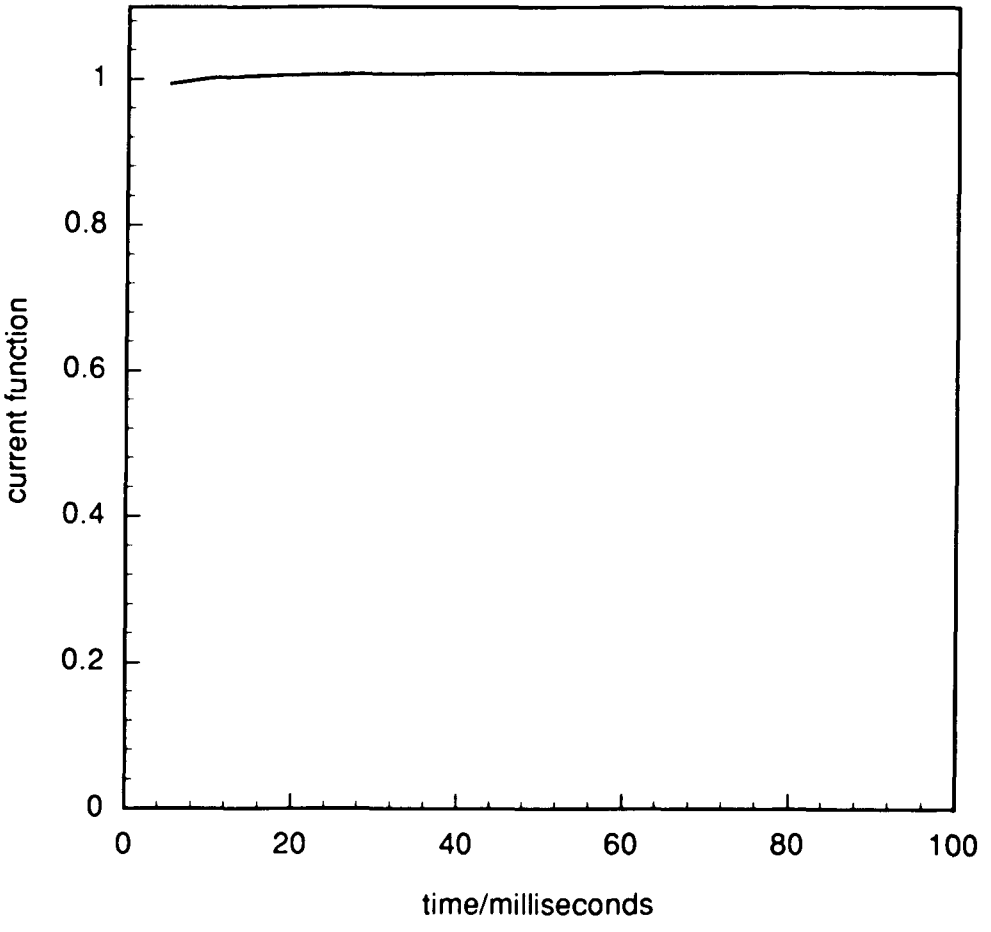

Figure 1.6 Current becomes diffusion limited when both k^{o} and k_f are very large. k^{o}= 1.0, $k_f=10^6$, α=0.5, E^{o}= -1.5v, E = -1.45v

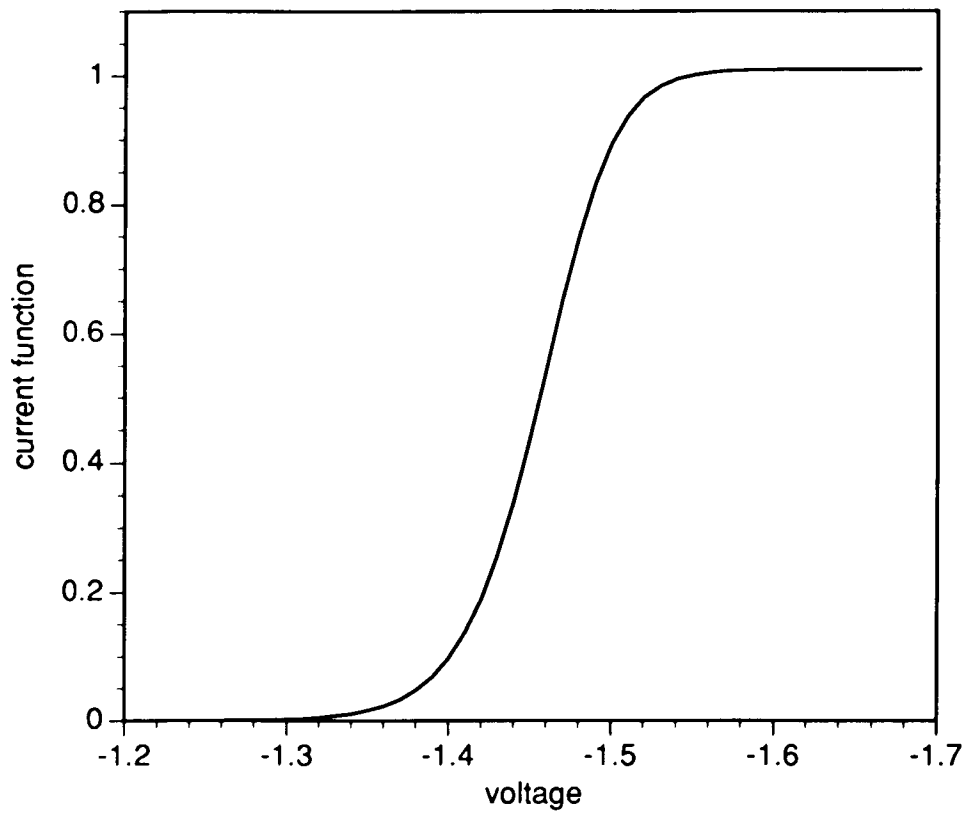

Figure 1.7 Normalized current as a function of applied voltage. α=0.5, k^o= 0.1cm/sec, k_f=1000 sec^{-1}, E^o= -1.5volts, time = 10 milliseconds

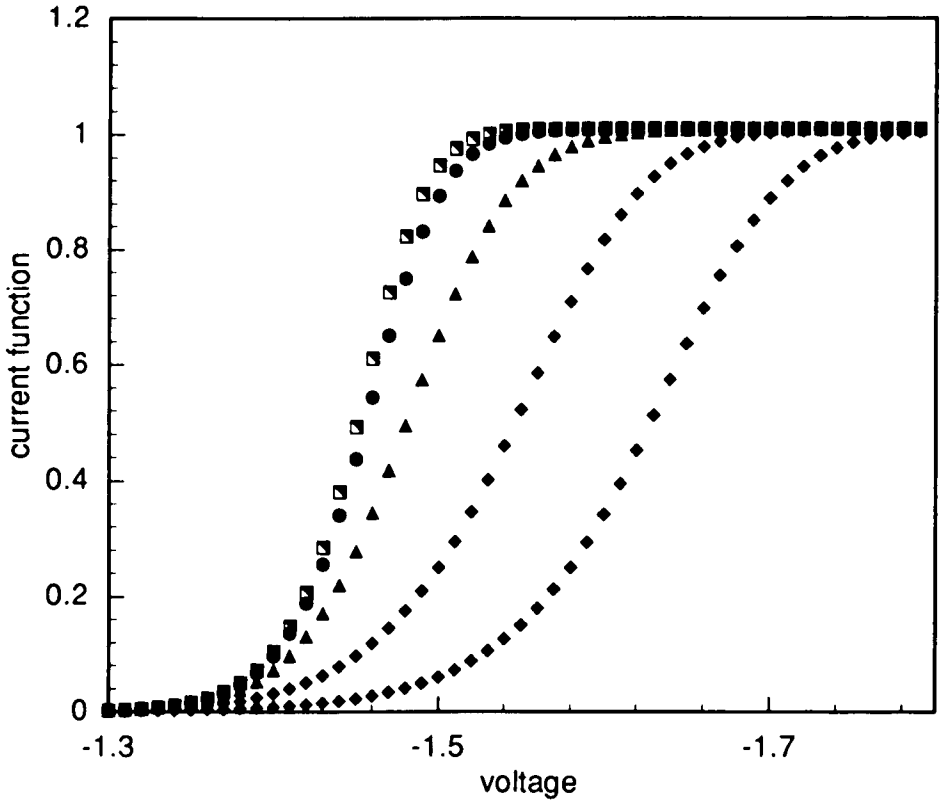

Figure 1.8 Effect of electron transfer rate on current -voltage curves.

$\alpha = 0.5$; $E^{o} = -1.5$volts; $k_f = 1000\ s^{-1}$; t = 10 ms

$k^{o}=0.5 cm\ s^{-1}$; $k^{o}=2\times10^{-2} cm\ s^{-1}$ $k^{o}=4\times10^{-3} cm\ s^{-1}$ $k^{o}=8\times10^{-4} cm\ s^{-1}$

$k^{o}=0.1 cm\ s^{-1}$

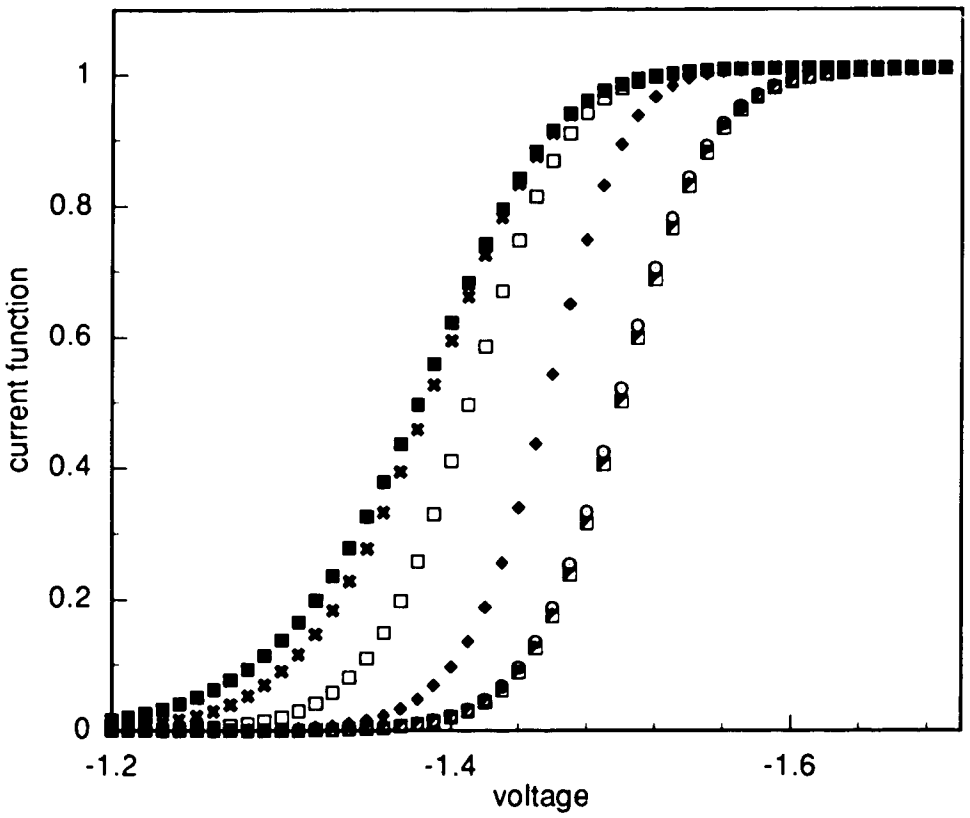

Figure 1.9 Effect of following reaction rate on normalized current-voltage curves. $\alpha = 0.5$; $k^o = 0.1$ cm s^{-1}; $E^o = -1.5$ volts; $t = 10$ ms.

▨ $k_f=10^{-1}$ o $k_f=10^1$ ◆ $k_f=10^3$ □ $k_f=10^5$ ✖ $k_f=10^7$ ■ $k_f=10^9$

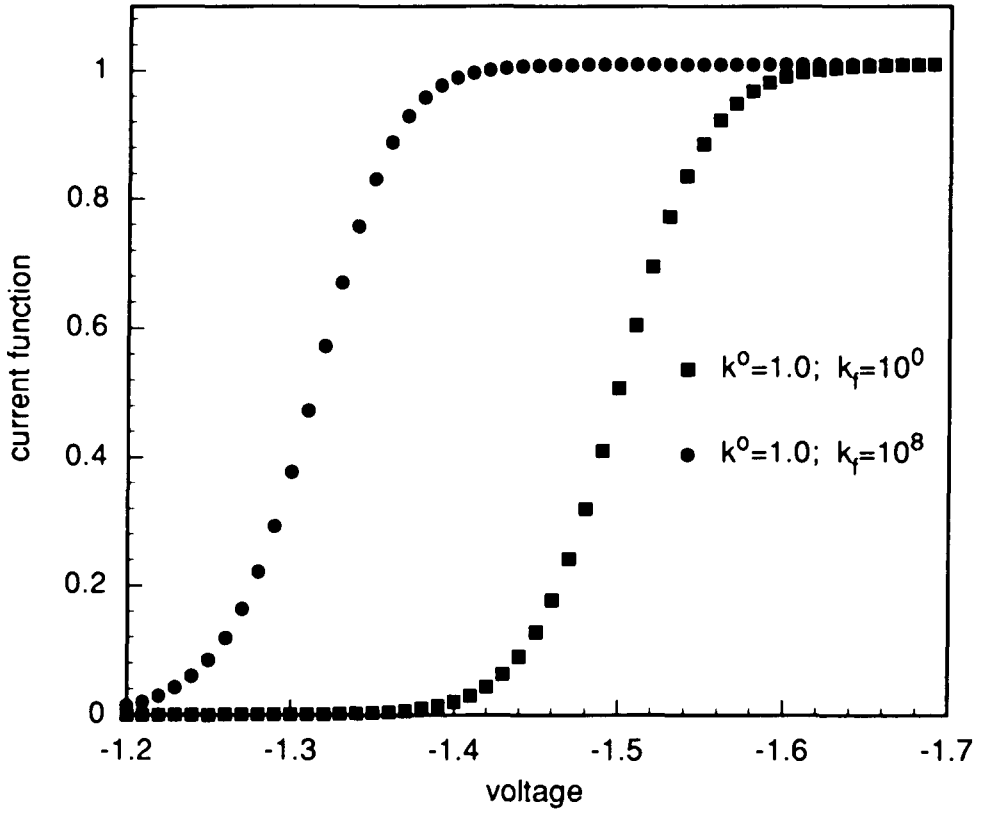

Figure 1.10a Effect of k_f on i-E curves when k^o is very large: The i-E curve shifts positive with no change in shape. α=0.5; E^o= -1.5 volts

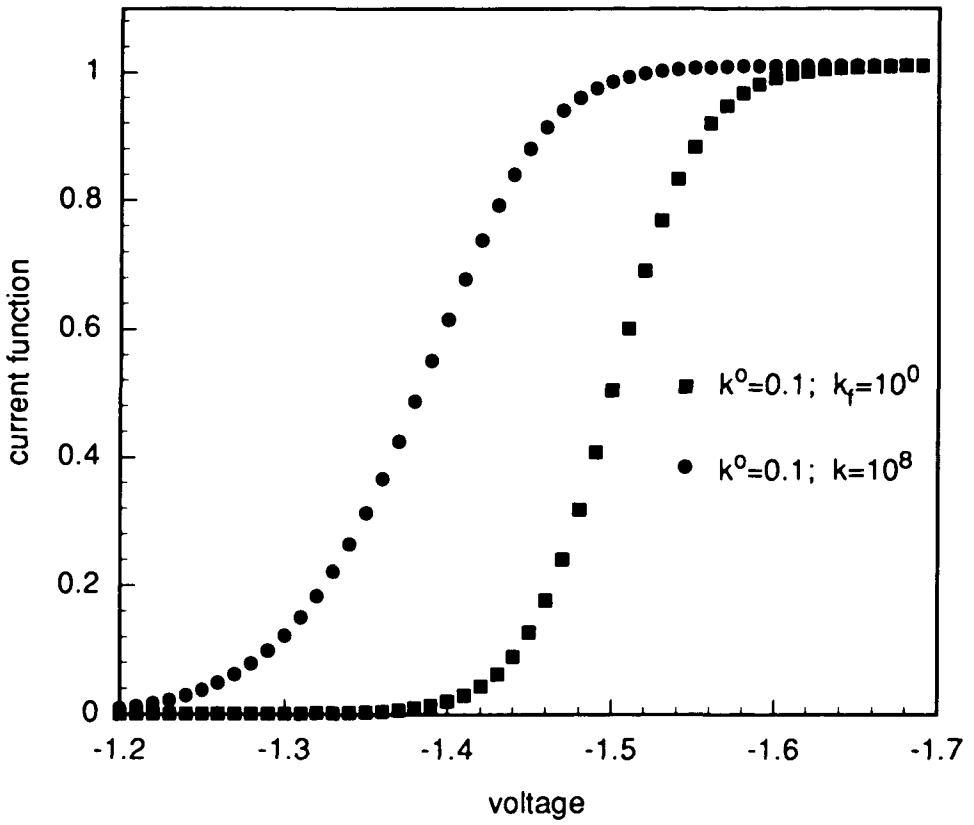

Figure 1.10b Effect of k_f on i-E curves when k^o is moderately large: The i-E curve shifts positive, more at the bottom. $\alpha = 0.5$; $E^o = -1.5$ volts

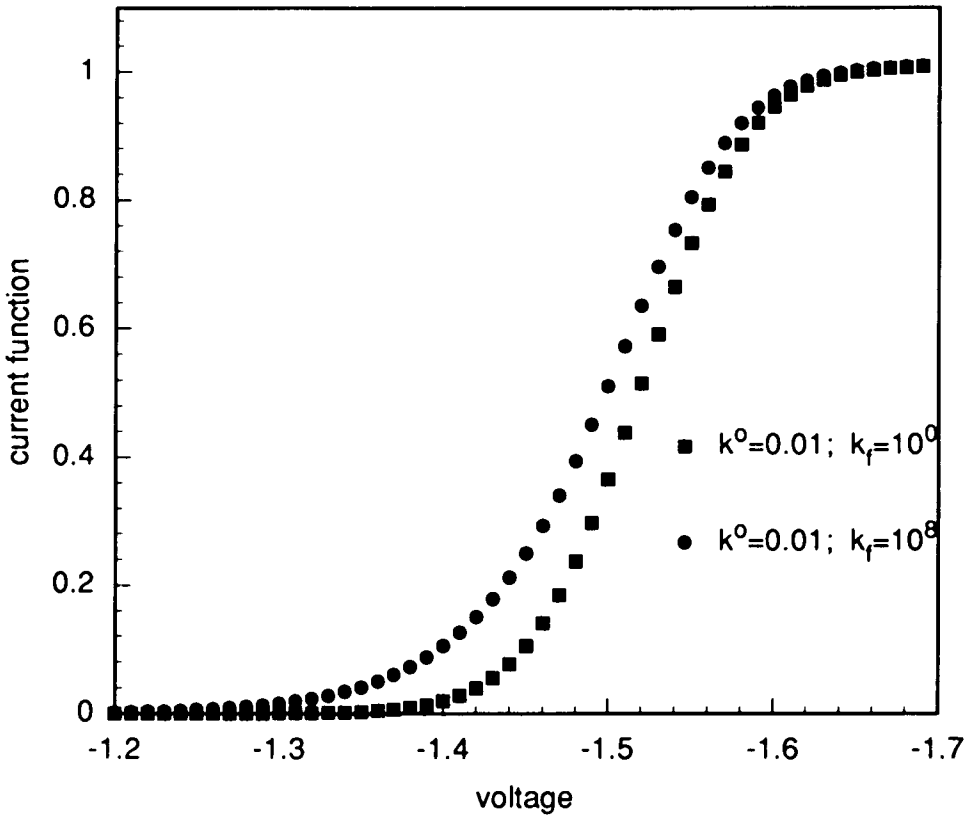

Figure 1.10c Effect of k_f on i-E curves when k^o is small: The i-E curve shifts very little, mostly at the bottom. $\alpha = 0.5$; $E^o = -1.5$ volts

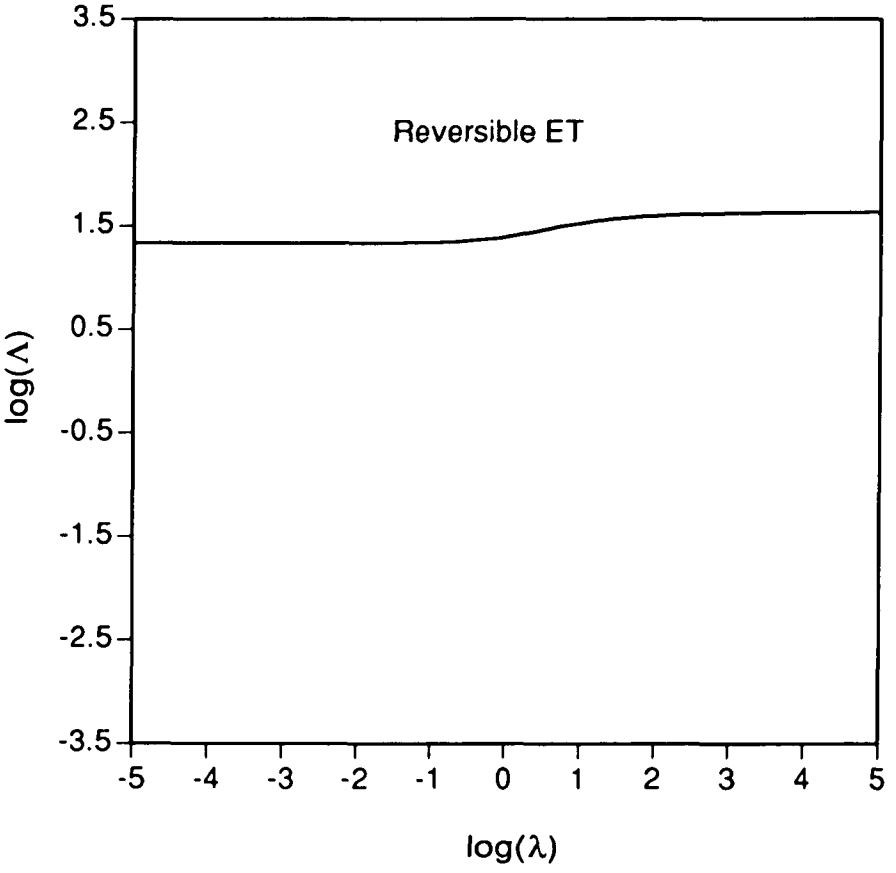

Figure 1.11
Region where electron transfer becomes reversible

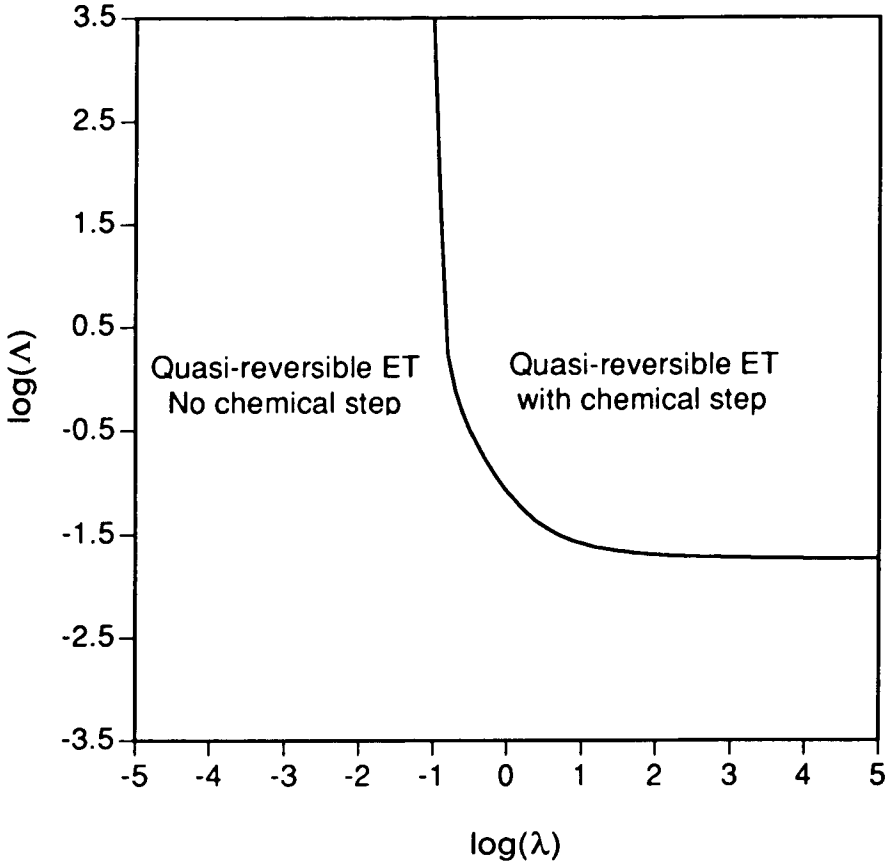

Figure 1.12
Region where chemical step begins to influence current

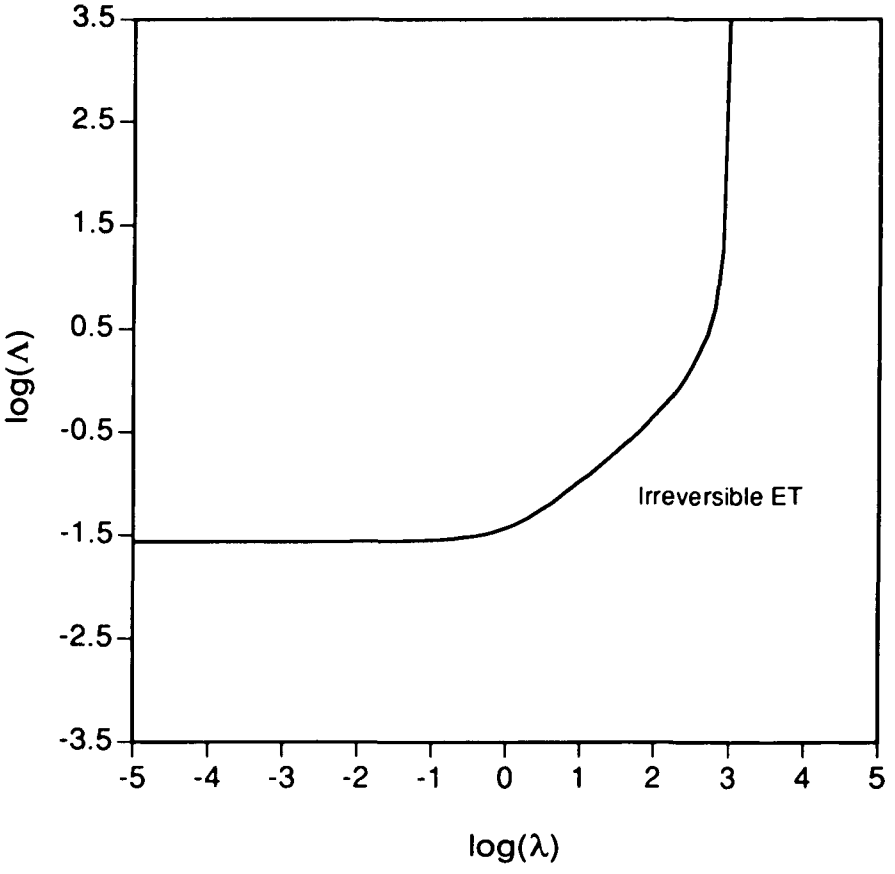

Figure 1.13
Region where electron transfer becomes irreversible

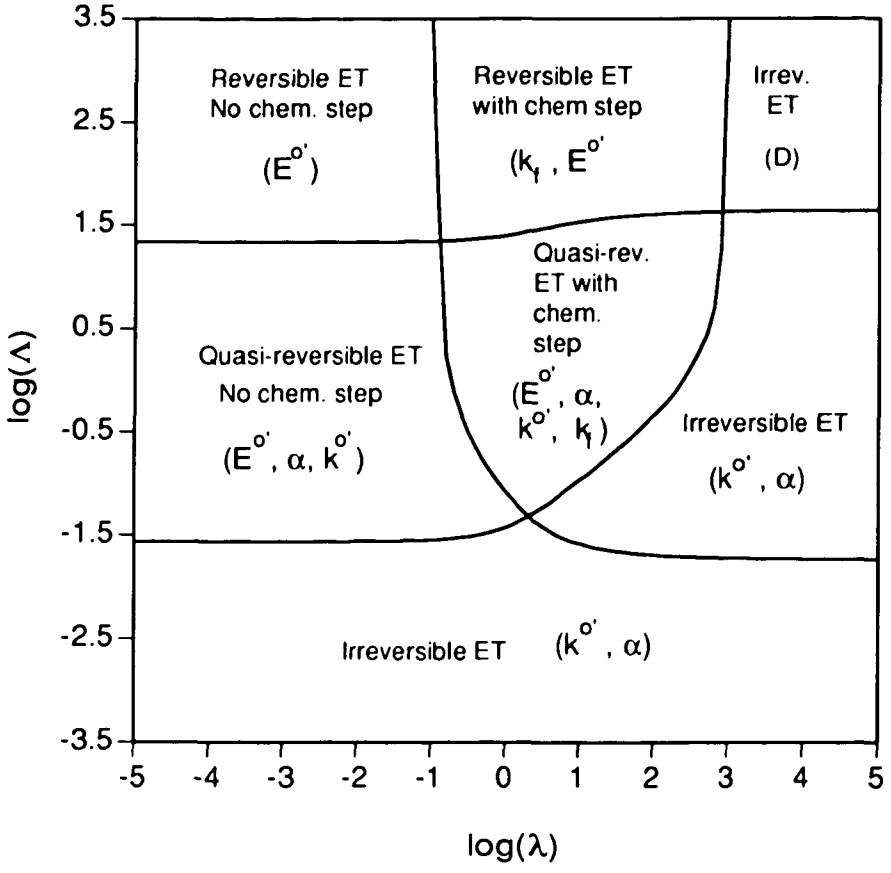

Figure 1.14
Kinetic Zone Diagram for EC reaction. Accessible parameters in each zone are listed in parenthesis
$E-E^{\circ}=0$ mv

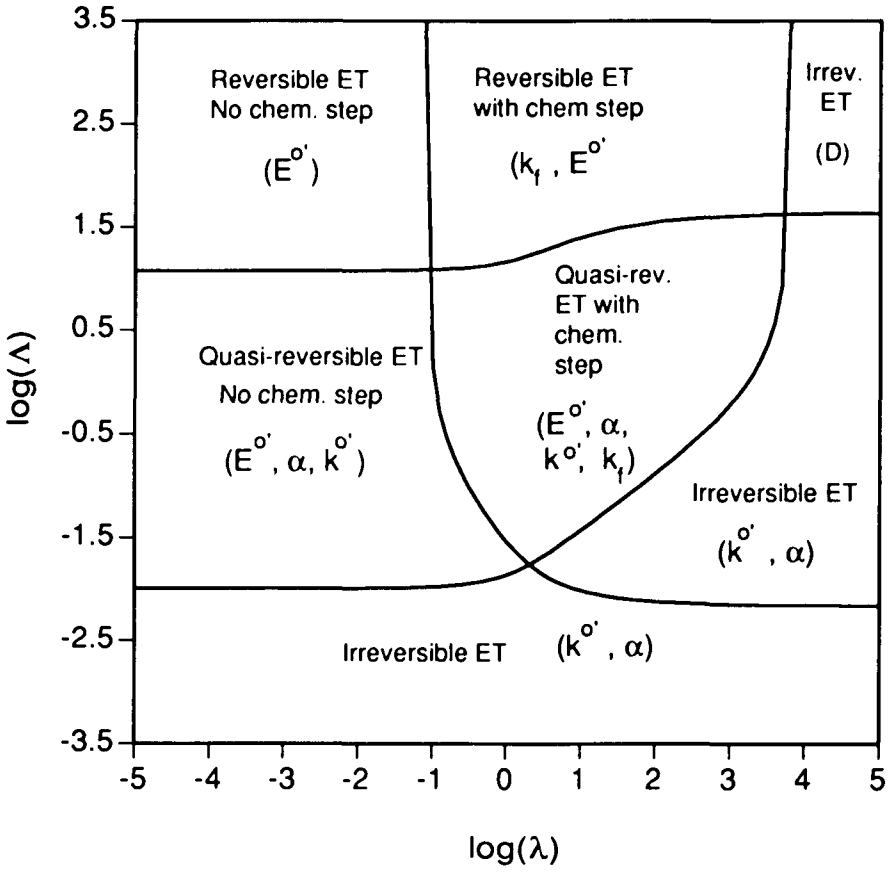

Figure 1.15
Kinetic Zone Diagram for EC reaction. Accessible parameters in each zone are listed in parenthesis
$E-E^{o}=25$ mv

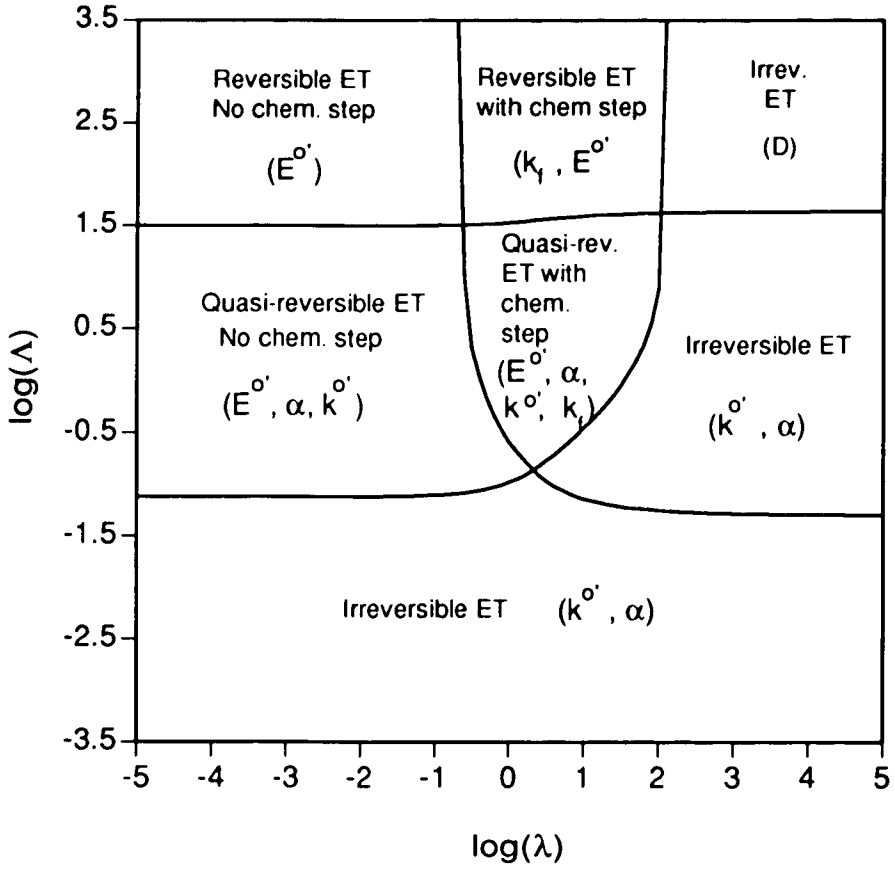

Figure 1.16
Kinetic Zone Diagram for EC reaction. Accessible parameters in each zone are listed in parenthesis
$E-E^{o}=-25$ mv

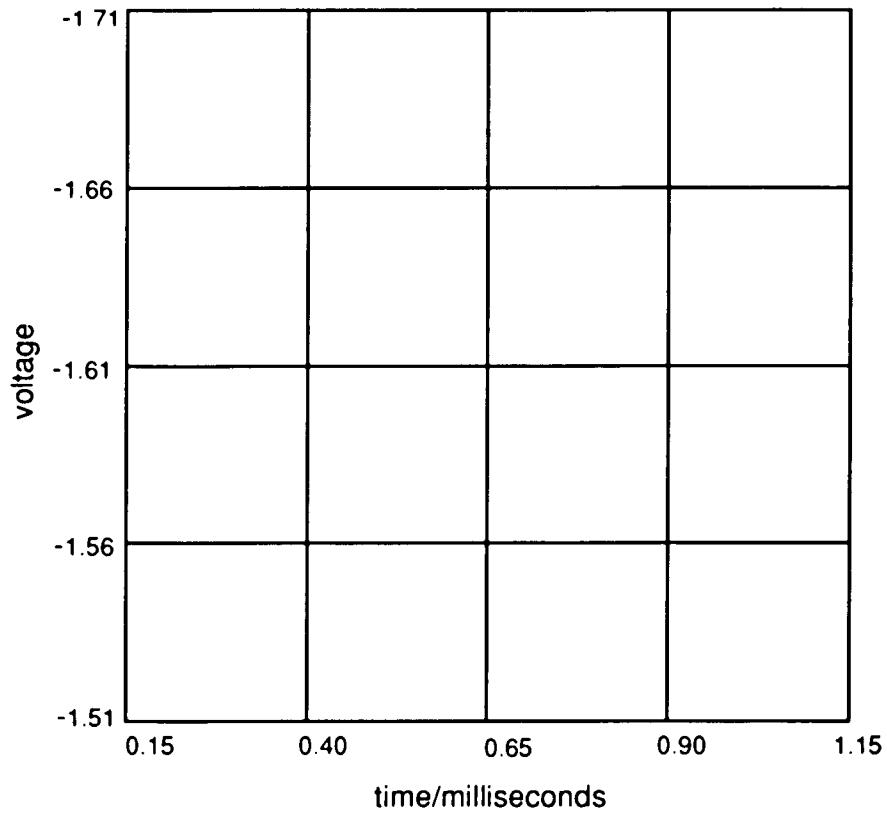

Figure 1.17 Voltage-Time (E-t) surface

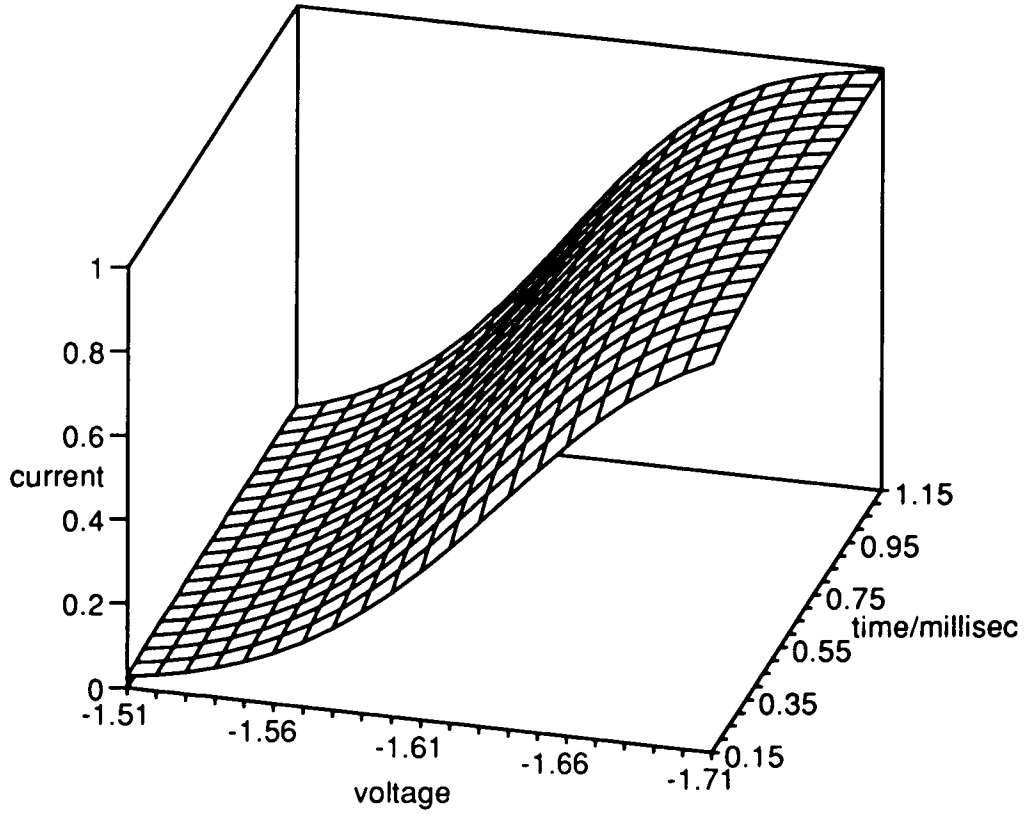

Figure 1.18 Simulated Current-Voltage-Time (i-E-t) surface. Table 1.3 has the results of fitting this surface to equation 1.5

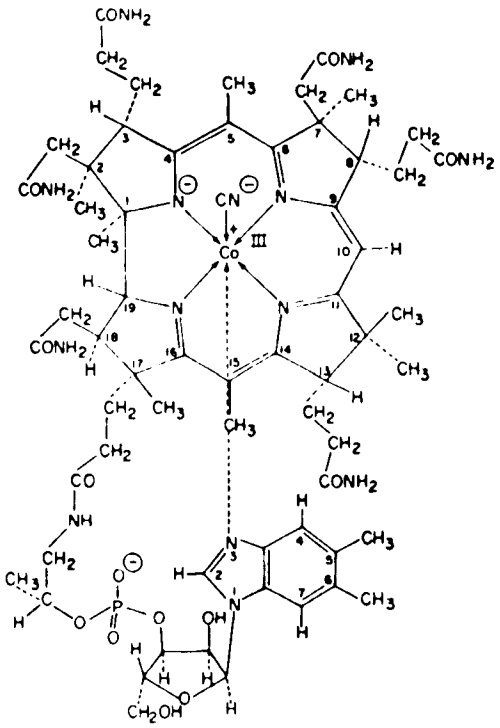

Figure 1.19

The Vitamin B_{12} Molecule

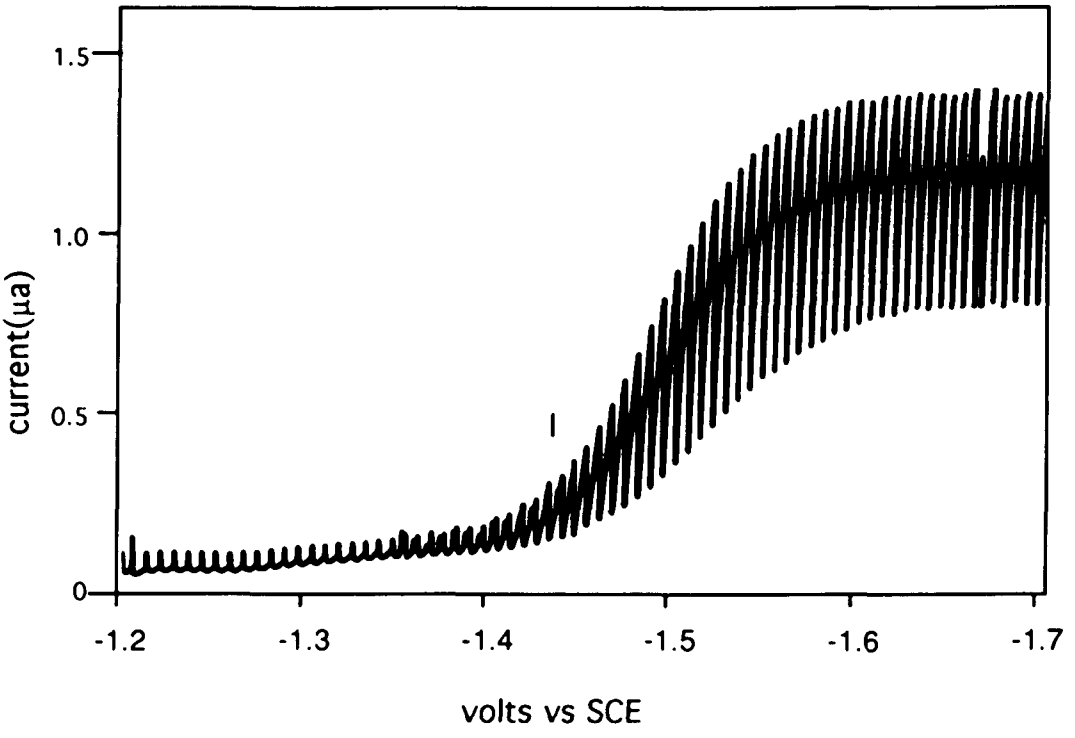

Figure 1.20 DC polarogram of methyl cobalamin (1millimolar) in DMSO. Supporting electrolyte: 0.1M tetrabutyl ammonium perchlorate (TBAP).

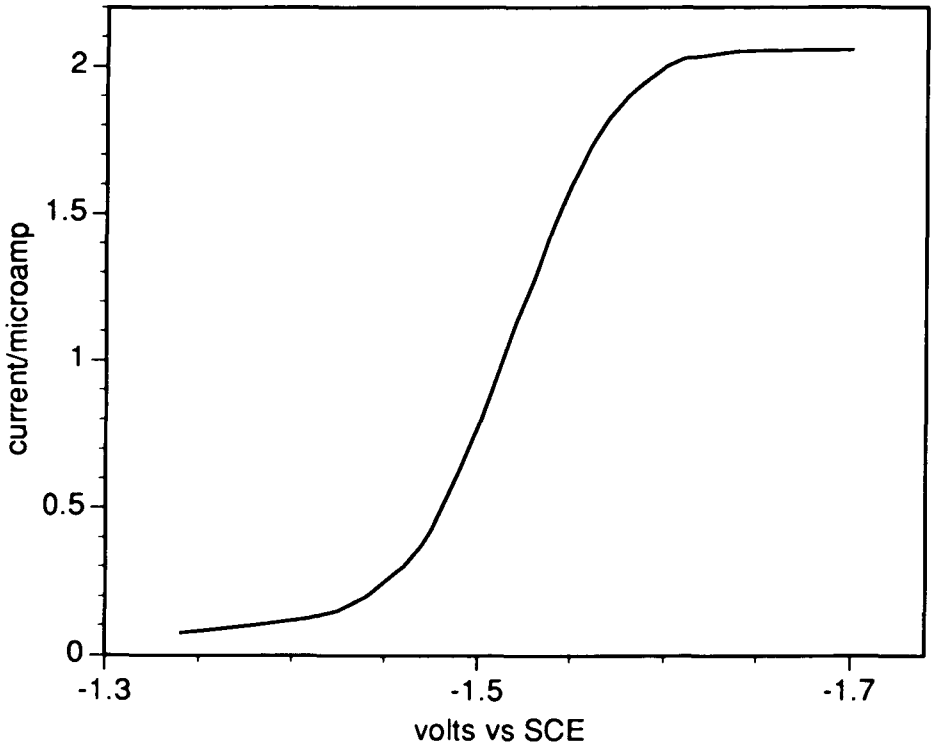

Figure 1.21 Normal Pulse Polarogram of methyl cobalamin (10^{-3} M) in DMSO. Supporting electrolyte: 0.1 M TBAP. Pulse-width: 80 millisec.

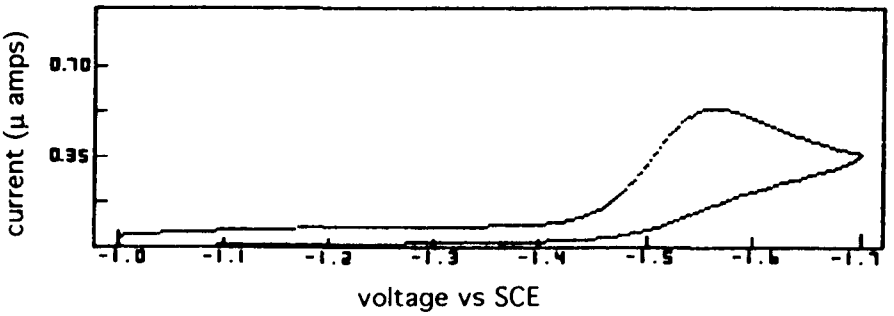

Figure 1.22 Cyclic voltammogram of methyl cobalamin in DMSO. Scan rate: 300 mv/sec

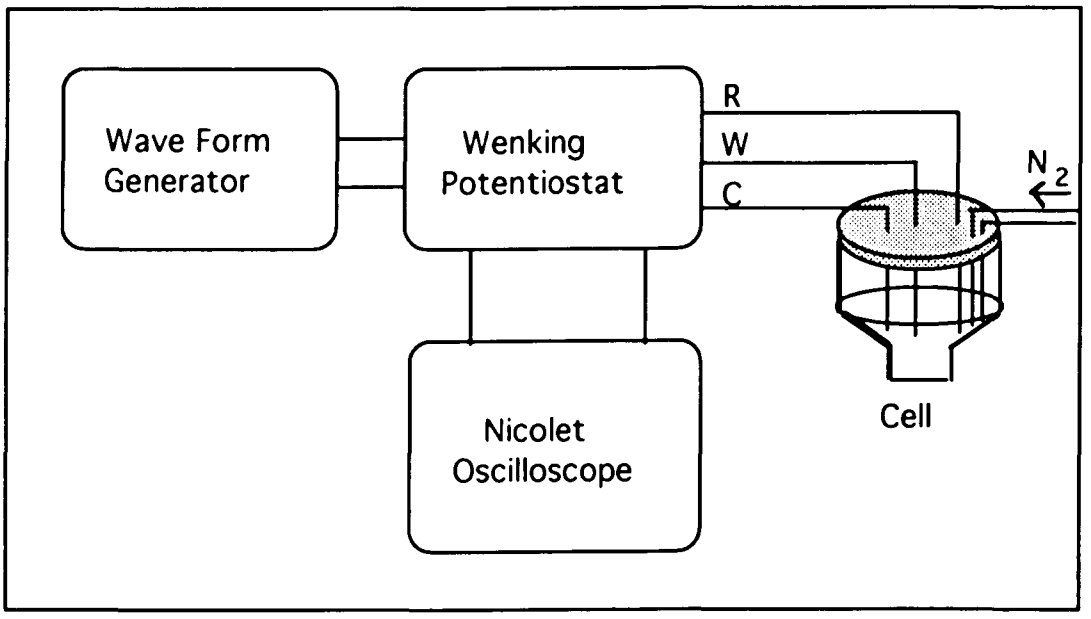

Figure 1.23
Experimental set-up for recording current-time curves

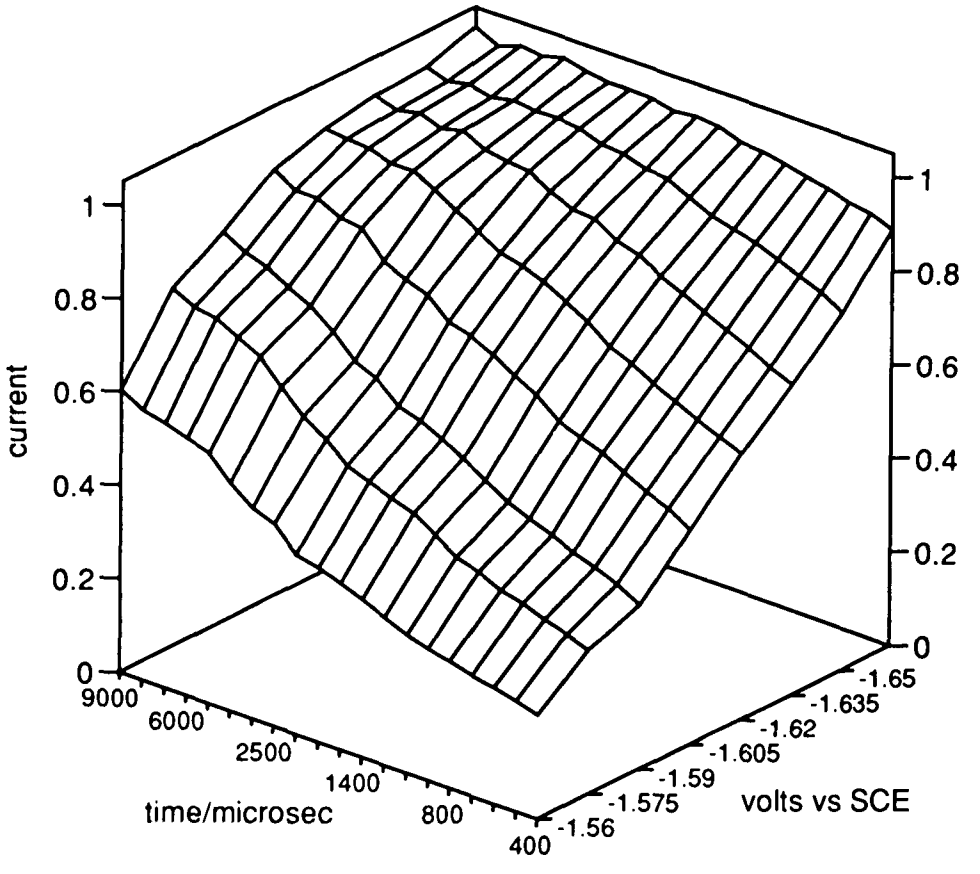

Figure 1.24 Experimental current-voltage-time surface. Data is normalized current for methyl cobalamin (millimolar) in DMSO.

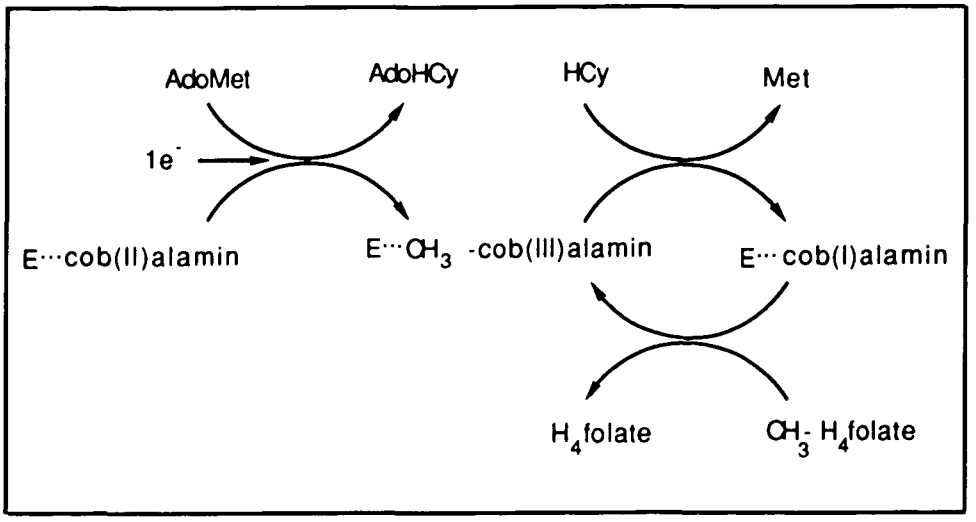

Figure 1.25
Final step in methionine synthesis, catalyzed by enzyme-bound methylcobalamin.

time sec	α	k^o cm sec^{-1}	k_f sec^{-1}	E^o volts	Φ
$1x10^{-3}$	0.474 (0.5)	0.066 (0.05)	3644 (1000)	-1.62 (-1.60)	$2.3x10^{-5}$
$5x10^{-4}$	0.463 (0.5)	0.076 (0.05)	6898 (1000)	-1.62 (-1.60)	$5.9x10^{-4}$
$1x10^{-4}$	0.478 (0.5)	0.099 (0.05)	7088 (1000)	-1.63 (-1.60)	$2.6x10^{-3}$
$2x10^{-3}$	0.596 (0.5)	0.028 (0.05)	26.56 (1000)	-1.58 (-1.60)	$1.1x10^{-3}$
$2x10^{-3}$	0.863 (0.5)	0.002 (0.005)	$2x10^{17}$	-1.52 (-1.60)	$4.1x10^{-1}$
$5x10^{-3}$	0.650 (0.5)	0.025 (0.01)	34.38 (1000)	-1.57 (-1.60)	$8.5x10^{-5}$

Table 1.1 Parameters estimated by fitting simulated i-E data. True values are listed in parenthesis

time sec	α	k^o cm sec^{-1}	k_f sec^{-1}	E^o volts	Φ
$5x10^{-6}$ to $1x10^{-3}$	0.237 (0.5)	0.030 (0.05)	500 (500)	-1.50 (-1.50)	$2.4x10^{-13}$
$5x10^{-5}$ to $1x10^{-2}$	0.185 (0.5)	0.027 (0.05)	500 (500)	-1.50 (-1.50)	$2.6x10^{-13}$
$2x10^{-4}$ to $2x10^{-3}$	-0.51 (0.5)	0.0095 (0.01)	$1x10^{15}$ (500)	-1.60 (-1.60)	$8.1x10^{-3}$
$5x10^{-5}$ to $5x10^{-3}$	-1.6 (0.5)	0.072 (0.01)	$2x10^{16}$ (1000)	-1.59 (-1.60)	$2.5x10^{-1}$
$5x10^{-4}$ to $3x10^{-3}$	0.002 (0.5)	0.0073 (0.005)	2894 (2000)	-1.63 (-1.60)	$2.1x10^{-6}$
$1x10^{-4}$ to $5x10^{-4}$	-0.72 (0.5)	0.022 (0.05)	1000 (1000)	-1.60 (-1.60)	$6.4x10^{-13}$

Table 1.2 Parameters estimated by fitting simulated i-t data. True values are listed in parenthesis

Time sec	α held constant	E^o volts held constant	k^o cm sec^{-1} held constant	k_f sec^{-1} adjustable	Φ
10^{-4}	0.5 (0.5)	-1.5 (-1.5)	0.04 (0.05)	1562 (1000)	$2.4x10^{-1}$
10^{-4}	0.5 (0.5)	-1.5 (-1.5)	0.06 (0.05)	471 (1000)	$1.5x10^{-1}$
10^{-3}	0.5 (0.5)	-1.5 (-1.5)	0.04 (0.05)	1084 (1000)	$6.0x10^{-2}$
10^{-3}	0.5 (0.5)	-1.5 (-1.5)	0.06 (0.05)	936 (1000)	$2.9x10^{-2}$
10^{-2}	0.5 (0.5)	-1.5 (-1.5)	0.04 (0.05)	1055 (1000)	$2.4x10^{-2}$
10^{-2}	0.5 (0.5)	-1.5 (-1.5)	0.06 (0.05)	962 (1000)	$1.1x10^{-2}$

Table 1.3 Adjustment of k_f to offset error in k^o for i-E curves from different time windows. True parameter values are given in parenthesis.

	time/ voltage	α 0.5	k^o 0.05cm sec^{-1}	k_f 1000 sec^{-1}	E^o -1.60 volts	Φ
i - E data	150 μ sec	0.437	0.0079	15048	-1.62	2.13×10^{-4}
	400 μ sec	0.422	0.0072	8257	-1.622	3.79×10^{-5}
	650 μ sec	0.429	0.0062	4370	-1.616	6.04×10^{-6}
	900 μ sec	0.428	0.0587	4101	-1.617	3.91×10^{-6}
	1150 μ sec	0.429	0.0057	4060	-1.617	3.92×10^{-6}
i-t data	-1.51 volts	-4.42	0.0422	1013	-1.603	2.34×10^{-2}
	-1.56 volts	-0.704	0.0607	2.5×10^{15}	-1.487	2.70×10^{-1}
	-1.61 volts	0.003	0.3514	1000	-1.6	1.60×10^{-12}
	-1.66 volts	1.21	0.0047	2527	-1.634	1.42×10^{-2}
	-1.71 volts	1.05	0.0047	1000	-1.6	1.80×10^{-14}
i-E-t data	150-1150 μ sec ; -1.51 to -1.71volts	0.5	0.05	1000	-1.6	4.00×10^{-12}

Table 1.4 Parameters estimated by fitting simulated i-t, i-E and i-E-t data
i-E data are current-voltage curves at the time specified under 'time/voltage'
i-t data are current-time curves at the voltage specified under 'time/voltage'
i-Et data are points on the E-t surface specified under 'time/voltage'

Expt#	α	k^o cm sec^{-1}	k_f sec^{-1}	E^o volts vs SCE
1	0.552 ± .020	0.0052 ± .0039	1430 ± 1620	-1.54 ± .03
2	0.546 ± .022	0.0061 ± .0040	1640 ± 1500	-1.55 ± .03
3	0.557 ± .020	0.0042 ± .0038	1260 ± 1800	-1.53 ± .04
4	0.553 ± .024	0.0050 ± .0048	1450 ± 1950	-1.54 ± .04
5	0.550 ± .022	0.0055 ± .0041	1530 ± 1590	-1.55 ± .03

Table 1.5 Kinetic and thermodynamic parameters for electron transfer and coupled homogeneous reaction of methyl cobalamin in DMSO

Parameters	α (0.5)	k^o cm sec^{-1} (0.05)	k_f sec^{-1} (10000)	E^o volts vs SCE (-1.60)
noise-free data	0.5 $\pm 1.1 \times 10^{-7}$	0.05 $\pm 1.7 \times 10^{-8}$	10000 $\pm 1.2 \times 10^{-2}$	-1.60 $\pm 1.6 \times 10^{-8}$
noisy data	0.44 $\pm 5.3 \times 10^{-2}$	0.056 $\pm 7.5 \times 10^{-3}$	9477 $\pm 5.2 \times 10^{3}$	-1.602 $\pm 7.0 \times 10^{-3}$

Table 1.6 Effect of added noise on error estimates. True values of the parameters are listed in parantheses

PART II

ELECTRO-CATALYTIC DETECTION IN HIGH PERFORMANCE LIQUID CHROMATOGRAPHY OF VITAMIN B_{12} AND OTHER MOLECULES OF BIOLOGICAL AND ENVIRONMENTAL INTEREST

2.1 Introduction

Several compounds of biological and environmental interest that include Vitamin B_{12} (cyanocobalamin) and Vitamin B_1 (thiamine) undergo an electrocatalytic reaction known as catalytic hydrogen evolution upon reduction in acidic or neutral media. The molecule acts as a catalyst in reducing hydrogen ions in the solution, producing a large reduction current. The following is a suggested mechanism [52] for this reaction:

$$B + HA \rightleftharpoons BH^{\cdot} + A$$

$$BH^{+} + e^{-} \rightarrow BH$$

$$BH \rightarrow B + \tfrac{1}{2}H_2$$

$$\text{---------- (sum)} \qquad HA + e^{-} \rightarrow \tfrac{1}{2}H_2 + A^{-}$$

B represents the catalyst, which, in general is a base. HA is the proton donor in the medium. Though the exact mechanistic sequence is not fully established, the following characteristics are known about catalytic hydrogen evolution:

1) Current increases with lowering of pH.

2) Current increases with increasing buffer capacity.

3) Current increases with increasing concentration of the catalyst and reaches a limit, that depends on the concentration of the proton donor in the medium.

4) Compounds that give rise to catalytic hydrogen current are generally nitrogenous organic molecules capable of binding a proton to the free electron pair of the nitrogen atom. Many of these compounds are adsorbed strongly on the mercury electrode.

Several classes of organic molecules including proteins [53,54], alkaloids [55] and pyridine derivatives [56] have been reported to give rise to large catalytic currents. This chapter explores the possibility of developing an electrochemical detector for high performance liquid chromatography (HPLC), that takes advantage of the electrocatalytic process (HPLC-ECat) to achieve high levels of sensitivity.

High performance liquid chromatography [57,58], as an analytical technique, has undergone phenomenal growth in the past two decades. Nearly 70% of all pharmaceutical analyses are nowadays performed using HPLC. The major components of an HPLC system are the solvent delivery system, the chromatographic column and the detector. A substantial amount of the research work done in HPLC is directed towards developing new detectors or improving existing ones, as evidenced by the large number of research papers appearing in current journals and the number of new patents issued each year. Development of an HPLC detector based on reductive electrochemistry at the dropping mercury electrode is described in this chapter. This

detector, while capable of responding to any species that undergoes reduction at mercury, is highly sensitive for Vitamin B_{12}, thiamine and other compounds that exhibit catalytic hydrogen evolution.

Electrochemical or electrical properties of the components of chromatographic effluents have been utilized as a basis for detection long before the advent of high-performance liquid chromatography. In 1940 Troitskii [59] detected the adsorption boundaries in liquid chromatography by measuring the dielectric constants. In 1947 Muller [60] designed a continuous flow system with an amperometric cell for the measurement of low levels of hydroquinones. The combined use of electrochemical detectors and liquid chromatography was first reported by Drake [61] and Kemula [62] as early as 1950. However the full potential of the tandem operation of electrochemistry and liquid chromatography was not realized until the detection technique was further adapted and refined by Adams [63] and Kissinger et. al. [64]. It soon became evident that electrochemical detection would be unrivaled in the HPLC analysis of certain classes of compounds in terms of sensitivity and linear dynamic range. During the last ten-fifteen years this technique has experienced spectacular ascent and its principles [65-72] and applications [73-80] have been reviewed in numerous publications.

A wide variety of organic and inorganic compounds are electroactive and amenable to electrochemical detection. Tapping this potential requires addressing certain practical considerations that go into the construction and maintenance of EC detectors. It is a relatively simple task to build electrochemical detectors that use solid working electrode material such as platinum, gold, graphite, glassy carbon, carbon paste etc. Several such detectors are described in the literature [81-92]. Solid electrodes in HPLC detectors have certain serious drawbacks. Most important is the

irreproducibility of surface conditions. The electrode surface is easily poisoned by formation of oxide films, polymeric compounds, dissolution in mobile phase etc. The life span of solid electrodes, especially carbon paste and glassy carbon are relatively short, i.e., a few weeks or months. Maintenance of the electrode often requires polishing, electrochemical pretreatment or other means of conditioning. Several of these limitations can be overcome by use of a liquid electrode such as the dropping mercury electrode. Also the bulk of electrochemical data in the literature is from polarographic studies done at the dropping mercury electrode. Several papers exploring the use of mercury electrodes for HPLC have appeared [93-100].

Besides electrode materials, another area of active research is the potential wave form applied to the working electrode [92,93]. In the most basic amperometric detector a constant potential is applied on the working electrode. Selectivity and sensitivity has been increased in electrochemical detectors by the use of more sophisticated potential wave forms and data acquisition methods. These include the differential pulse [101] and square wave [100], among others. The potential of the working electrode is linearly varied in rapid scanning electrochemical detection, with or without superimposed voltage pulses [88,96,97]. The resulting current vs voltage curves can be displayed as a function of time forming a three dimensional chromato-voltamogram [98,99] which can reveal more specific information about the components in the sample. The use of multi-electrode, mostly dual-electrode, electrochemical detectors have also been explored [102]. Typically, the product of oxidation or reduction occurring at an upstream electrode is monitored at a downstream electrode.

During the last 10-15 years the popularity of electrochemical detectors in HPLC has steadily increased and all major manufacturers of commercial HPLC equipment supply EC

detectors. These are mostly for oxidative detection and fewer systems for reductive detection, which use mercury electrode have appeared. The potential of the electrochemical detector for HPLC is far from being fully exploited. The best approach to closing this gap is the development of sensitive detectors that are easier to maintain and operate.

2.2 History of Development in Our Laboratory

The experimental set-up presently in use in our laboratory is the result of several stages of development. Our initial attempts to develop an electrochemical detector for HPLC employed a commercially available detector cell manufactured by Bio-Analytical Systems (BAS) Inc. shown in figure 2.1. The working electrode in the BAS cell is a disc made of platinum, gold or glassy carbon embedded in a Kel-F® block. A thin film spacer separates the working electrode block from another Kel-F® block. An oval shaped piece is cut out from the spacer creating a cavity. Eluent from the chromatographic column is passed through this cavity. An Ag/AgCl reference electrode and a platinum counter electrode are also provided.

To analyze samples containing vitamin B_{12} derivatives using the BAS cell, the amalgamated platinum working electrode was used. The mobile phase used was a mixture of water and acetonitrile (50:50) containing 0.05M sodium acetate and was titrated to a pH of 5.0 using glacial acetic acid. The stationary phase was a C-18 reverse phase column from Waters Associates. The background obtained when this cell was operated at -1.5 volts vs SCE showed a steady increase in noise with time. The major cause of this noise was tiny gas bubbles on the electrode surface. These were not bubbles transported by the mobile phase, but small amounts of hydrogen gas forming on the electrode surface that aggregate to form larger bubbles. It is necessary to use an

acidic mobile phase to obtain large currents by way of the catalytic hydrogen evolution reaction. The formation of hydrogen gas on an amalgamated platinum surface is inevitable under these conditions.

The use of a hanging mercury electrode was explored next, thus reducing the effect of platinum which has a very low overvoltage for reduction of hydrogen ions. The mercury drop was suspended from the recessed tip of a platinum wire fused inside a glass tube. This does not eliminate the presence of platinum in the working electrode material completely. A Kel-F® block was machined to fit the glass tube as shown in figure 2.2. Eluent from the column was carried by a Teflon® tubing and introduced in the immediate vicinity of the suspended mercury drop. The working electrode and the Kel-F® adapter were immersed in a cell containing the mobile phase. Reference and counter electrodes were also introduced into the bulk solution contained in the cell. The bulk solution was deoxygenated by bubbling nitrogen gas. The background obtained with this set-up was less noisy in the beginning. However with time the noise-level did build up, rendering this arrangement unusable. Also, the Kel-F® polymer was not compatible with the acetonitrile:water mobile phase.

The above results clearly demonstrate that a substantial amount of hydrogen ions is reduced under the conditions of this experiment, characterized by low pH and very negative potentials. It is imperative that the electrode surface be renewed frequently, to prevent build-up of hydrogen gas. For all practical purposes, the use of solid electrodes is ruled out and this led to our attempts to use dropping mercury, which is perhaps the only viable electrode material for a detector based on catalytic hydrogen evolution.

One of the reasons for the lack of popularity of dropping mercury electrode in EC detectors is the mechanical difficulty in configuring mercury drops falling from a capillary into the eluent stream, without significantly contributing to band broadening or deterioration of signal-to-noise ratio. Two of the designs tested in this laboratory are shown in figures 2.3 and 2.4.

Fig 2.3 shows a glass capillary commonly used to construct the dropping mercury electrode in polarographic studies. The capillary is surrounded by a glass cage. The eluent from the column passes through a narrow bore (0.3 mm) Teflon® tubing and exits directly below the mercury drops falling from the capillary tip. The electrode is immersed in the mobile phase contained in a polarographic cell. The bulk solution is kept deoxygenated by bubbling nitrogen gas. Counter and reference electrodes are also introduced in the bulk solution. Excess background noise due to formation of hydrogen gas on the electrode surface was clearly overcome in this design. However with the glass cage made by fusing glass tubes it was extremely difficult to achieve perfect concentric alignment of the mercury capillary and the Teflon® tube carrying the eluent. Yet perfect alignment of the two tubes is critical for optimum performance of the detector. The same function, namely bringing together the mercury drop and the eluent in close proximity, is realized in the current design by a Teflon® plug adapter shown in figures 2.4a and 2.4b The adapter plug fits tightly at the tip of the dropping mercury electrode. A 1.5 mm diameter bore is drilled through the center of the plug, parallel and concentric with the bore of the dropping mercury electrode. The Teflon® tube carrying the eluent is passed through this bore in the Teflon® plug and positioned very close to the mercury drops falling from the capillary tip. Tightening the Teflon® screw on the plug will hold the tube in place. Holes drilled on the sides of the adapter allows eluent and spent mercury to flow out into the bulk solution. Since precision

machining is easier than precision glass-blowing this device was constructed easily and did perform better.

2.3 Overview of the Experiment

The experimental set-up consists of the solvent delivery system, the chromatographic column and the detector. The solvent delivery system used for most of the experiments was a reciprocating pump from Milton Roy. The chromatographic column was a C18 reverse phase column from either Waters Associates or Supelco. The detector consisted of the electrochemical cell as described above together with different configurations of potentiostats and current followers. In one configuration a MINC laboratory computer was used to apply the potential wave form and to acquire and analyze the data. An alternate configuration used a Tacussel pulse polarograph to apply the voltage on the working electrode and to monitor the current response. The Tacussel polarograph is normally used for DC, Tast, Normal Pulse and Differential Pulse polarography, all of which apply a linearly varying voltage with or without superimposed pulses. Interestingly enough, the differential pulse polarographic (DPP) mode can be used to apply a constant size voltage pulse at regular intervals. The choice of pulse heights available are 1, 2, 5, 10, 20, 50 and 100 millivolts. The pulse duration can be varied from 10 to 80 milliseconds in increments of 10 milliseconds. After setting the operating conditions such as initial voltage and pulse height, the instrument is switched to 'external cell' leaving the 'scan' switch in the off position. Figure 2.5 shows the wave form applied on the working electrode and the resulting current produced under these conditions. The current output to the recorder is the difference between the currents sampled just before applying the pulse and at the end of the pulse. The mercury drop is knocked off at the end of each pulse and a new drop is allowed to form. As shown in figure 2.5 the charging

current, unlike the faradaic current, drops to very low levels within a few milliseconds after the pulse is applied. The differential measurement is therefore able to discriminate against the charging current. The ranges available on the Tacussel are somewhat limited, not always allowing the choice of conditions desired for different analyte samples. With the MINC computer, it was possible to select values of initial base potential (V1) and final step potential (V2) anywhere in the potential window available for the solvent. Also, the output could be either the direct current or the derivative current. The background current, mainly due to reduction of hydrogen ions was typically in the 2-3 microamp range. The 20 microamp range on the ammeter was the most sensitive current scale that could be used.

A block diagram of the overall experimental set-up is shown in Figure 2.6. The mobile phase is deoxygenated by sparging helium in a custom made flat bottom flask with air-tight ground glass cover. The helium is presaturated with acetonitrile in a bubbler to prevent loss of acetonitrile from the mobile phase. The mobile phase is then pumped through the column at a flow rate of 1 mL/minute. The eluent exits directly below the mercury drop in the polarographic cell. The bulk solution in the cell is maintained oxygen-free by bubbling nitrogen through a specially constructed bubbler that has a fine frit at the tip and a hood covering the frit. The hood vents directly above the liquid level in the cell. This arrangement allows continuous bubbling of nitrogen even as the chromatogram is being recorded. Any disturbance due to bubbling is contained within the hood and will not contribute to noise at the mercury drop, as was demonstrated. Complete deoxygenation is very important in reductive electrochemistry as dissolved oxygen is easily reduced at mercury. The Tacussel pulse polarograph and a Heath model SR-205 strip chart recorder complete the set-up.

The chromatograms of pure samples of vitamin B_{12}, thiamine, riboflavin and niacinamide, injected separately are shown in figures 2.7 - 2.10. The mobile phase was made up of acetonitrile (60%) and water (40%) containing 0.05M sodium acetate, titrated to a pH of 5.0. A C18 reverse phase column was used and the flow rate of mobile phase was 1 mL/minute. The retention times for the four vitamins under the above conditions, at room temperature are listed in table 2.1. Figures 2.11 and 2.12 are chromatograms of mixtures made up of the above four vitamins. The chromatogram of a commercial multivitamin-mineral preparation viz., Micebrin-T®, manufactured by Dista Pharmaceuticals is shown in figure 2.13. The tablet was crushed after removing the sugar coating and extracted using 50 mL of the mobile phase. The extract was diluted to 1/20th of its concentration and a 20 micro liter sample was injected. The mixture containing over 30 ingredients did not separate well in the isocratic mode. However several components in the mixture are shown to be susceptible to electrochemical detection at the mercury electrode. Better separation was possible with Theragran® containing vitamin B_1 (15 mg), vitamin B_2 (15 mg), vitamin B_6 (25 mg), vitamin B_{12} (12 µg), vitamin C (600 mg), vitamin E (30 I.U.), Niacin (100 mg), pantothenic acid (20 mg), folic acid (400 µg), biotin (45 µg) and iron (27 mg), per tablet. The chromatogram is shown in figure 2.14. Based on retention times and increase in peak height upon addition of known standard, peaks 1, 3 and 8 were assigned to riboflavin, niacinamide and thiamine which are all present in microgram levels in the injected sample. Vitamin B_{12} at less than 10 ng is obscured by peaks 4 and 5. Quantitative analysis of B_{12} and other vitamins in the tablet will require gradient elution and additional sample preparation.

2.4 Optimization of Experimental Parameters

Several experimental variables such as pH of the mobile phase, applied initial potential, pulse width and pulse height contribute to the magnitude of the current signal in the EC detector. The sensitivity of the detector can be greatly enhanced by optimizing these variables.

2.4.1 *Effect of pH on Detector Response*

The effect of varying pH on the catalytic reduction wave of vitamin B_{12} in acetonitrile : water (50:50) mixture containing 0.05M sodium acetate was examined using two different modes of polarography. Figure 2.15a shows the DC (Direct Current) polarogram of vitamin B_{12} recorded in the above solvent mixture whose pH was 8.56. There is only a hint of a reduction wave at about -1.55 volts. The polarogram was recorded again after adding one drop of glacial acetic acid to 50 mL of the above solution, thus lowering the pH to 6.71. The huge increase in current (figure 2.15b) is clear illustration of the orders of magnitude gain in sensitivity attainable by virtue of the catalytic process.

The current maxima, measured from several polarograms over a wide range of pH, is plotted in figure 2.16. The observed trend, viz., an increase in current as pH is lowered is easily predicted on the basis of the catalytic hydrogen evolution mechanism discussed earlier. The same trend was observed in the differential pulse polarographic (DPP) data. The significant increase in current with decreasing pH translates to higher sensitivity for the EC detector at lower pH. However, there is an opposing factor that tends to limit this gain in sensitivity. At low pH more hydrogen ions are reduced, forming hydrogen gas on the electrode surface. The

resulting fluctuation in the area of the electrode leads to an increase in noise. For the acetonitrile:water system there was no improvement in the detection limit when pH was lowered beyond 5.0.

2.4.2 *Effect of Working Electrode Potential on Current Signal*

The response of the dropping mercury electrode can vary significantly with small changes (tens of millivolts) in applied potential. In the differential pulse mode, the output is the difference between the currents flowing through the working electrode at potentials V_1 (before the pulse) and V_2 (after the pulse). Therefore, in choosing V_1 and V_2, it is logical to examine the differential pulse polarogram of the compound in the mobile phase. This is analogous to utilizing information from the UV-Vis spectrum of a compound in choosing the wavelength setting of UV-Vis detector. In the absence of complicating factors such as adsorption, the peaks in the DPP represent the voltages at which the change in current with voltage reaches a maximum. These voltages should also be the value of V_1 that gives rise to the biggest jump in current level when the pulse is applied. Figures 2.17a and 2.17b show several DPPs of vitamin B_{12} in acetonitrile : water mixtures at pH values ranging from 5 to 8. The current vs pH data (figure 2.18) shows the same trend as the DC polarographic data discussed earlier. Another important observation to be made here is a shift in peak potential in the positive direction as the pH is lowered. Also after reaching the peak, the derivative current drops below zero. The drop in current can be explained as a consequence of the electrode surface becoming blocked due to adsorption of the reduction product. Adsorption of molecules at the mercury surface is commonly observed in organic electrochemistry. As the pH is lowered the rate of formation of reduction product is increased and coverage by adsorption occurs earlier on the potential axis. The DPP data

suggest that the best value for initial potential may depend on the pH of the mobile phase. Also the peak potential data as read from the ill defined DPP of Vitamin B_{12}, may be misleading. The optimum value of V_1 can also be determined by recording several chromatograms over a wide range of initial potentials. This experiment was done for vitamin B_{12} and the data is presented in figure 2.19. The maximum in the curve, at -1480 millivolts, differs from the peak in the DPP. In chromatography the electrode is resting in the mobile phase free of analyte until the compound exits the column. Within the next few (10-15) seconds the compound is flushed out of the detector cavity by the eluent stream, whereas in DPP the electrode grows into a solution that contains a relatively higher concentration of the analyte at all times. As a result distortion due to adsorption is more pronounced in DPP. A study of DPP as a function of pH for thiamine (figure 2.20) in the same mobile phase showed peak currents that increase as pH is lowered. The peak potential did not depend on pH unlike the case of vitamin B_{12}. However, the position of the peak on the voltage axis was very close to the decomposition point of the solvent. This cut-off point shifts towards positive potentials as the pH is lowered and at very low pHs the DPP peak from thiamine gets buried. Thus, while the information from DPP experiments could narrow down the base potential range of the electrode, fine tuning by actual experimentation might be required for best results.

2.4.3 *Effect of Pulse-Width and Pulse-Height on Current*

Current in pulse polarography is expected to increase when pulse height is increased and also when pulse width is narrowed. Figure 2.21 shows DPP current increasing as pulse width is decreased for vitamin B_{12} at pH 4.6. However, as pulse width is narrowed, the contribution from capacitance current to the total current increases. Also as the pulse height is increased, the noise

level increases too. To realize the highest attainable sensitivity, it will be necessary to experiment with these variables. The best choice of pulse-width and pulse-height may depend on the actual operating conditions such as electrode area, mobile phase composition, flow rate etc.

2.5 Sensitivity and Signal-to-Noise Ratio

To determine the detection limit and other performance characteristics of the detector, its response as function of concentration of vitamin B_{12} was recorded over a wide range. The result is plotted as a calibration curve in figure 2.22. The curve deviates from straight line only at fairly large concentrations. The linear dynamic range of the detector is at least three orders of magnitude. The detection limit, as determined by extrapolating the straight line to signal to noise ratio of 2:1 , was 0.7 picomole, which is at least an order of magnitude lower than the detection limits reported in the literature [103-105].

There are several factors that adversely affect the signal-to-noise ratio in an EC detector. The EC detector is a solute property detector that relies on a reaction occurring on the surface and is therefore highly sensitive to mass transfer rate at the electrode. With the pump turned off, it is easy to obtain very smooth background even at very high sensitivity ranges. When the pump is turned on, the increased mass transfer rate leads to much higher background current and also higher noise levels. The background noise has the appearance of low level random noise superimposed on a low frequency periodic oscillation (figure 2.23). A very steady pump is essential for the detector to perform well.

Another factor that can add to the noise is irregularity in the mercury drop size. Each sampling of current in the DPP mode is

done on a new drop. The drop is then dislodged by the arm of the drop knocker hitting the capillary. The strength and speed of the arm or hammer and the position where it hits the capillary should be adjusted so that the drop falls off without causing excessive vibration. The tip of the capillary should be maintained clean since residual deposits can easily result in irregular drops. In seeking further improvements in the detector, one might consider modifying the Teflon® plug at the capillary tip. In the present form the eluent exits from the detector cavity into the bulk solution through four vents, about 2-3 millimeter in diameter. By reducing the number and size of these vents as well as the volume inside the detector cavity, it should be possible to flush out the analyte molecules from the vicinity of the electrode in much shorter time. This should decrease broadening of the peaks and increase the efficiency of separation.

2.6 Comparison with a Commercial Instrument (Waters 600E)

To assess the relative merit of the HPLC-ECat detection vs spectrophotometric detection using a modern LC system, several samples of vitamin B_{12} at different concentrations were analyzed using the Waters 600E liquid chromatographic system. The wavelength setting on the spectrophotometric detector was 363 nm corresponding to the maximum in the absorption spectrum of vitamin B_{12} shown in figure 2.24. The data in the form of a calibration curve are shown in figure 2.25. The curve shows a linear dynamic range of about three orders of magnitude which is not very different from that of the electrochemical detector. The detection limit calculated the same way as for EC detector was 1.2 picomole.

There are several aspects of the EC detector that offers considerable room for improvement. In its present state the EC

detector is a crude prototype, whereas the Waters 600E is one of the very modern top-of-the-line commercial instruments. That the EC detector compares well with the 600E is a clear indication of the promise that reductive electrocatalytic detection holds in HPLC analysis.

2.7 Summary

Many organic nitrogenous compounds have been reported to exhibit catalytic hydrogen evolution upon reduction at mercury electrodes. These include drugs, pesticides, proteins etc and their analysis at trace levels can be of enormous practical value. Redox chemistry of many of these molecules have been studied extensively at mercury electrodes. This information available in the literature will enable the analysis of trace levels of many of these compounds by HPLC using electrochemical detection.

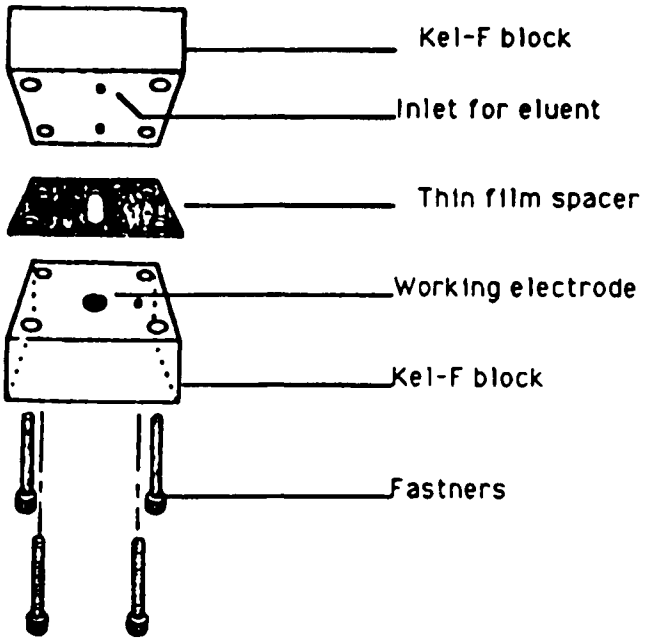

Figure 2.1 Thin-layer cell for BAS Electrochemiocal Detector.

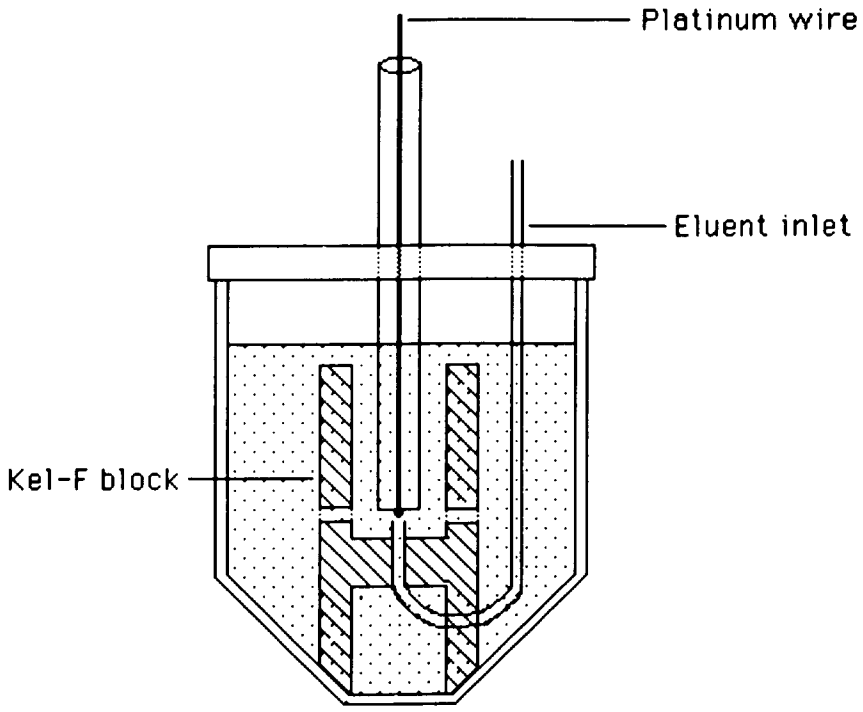

Figure 2.2 Kel-F block adapter used with hanging mercury drop electrode.

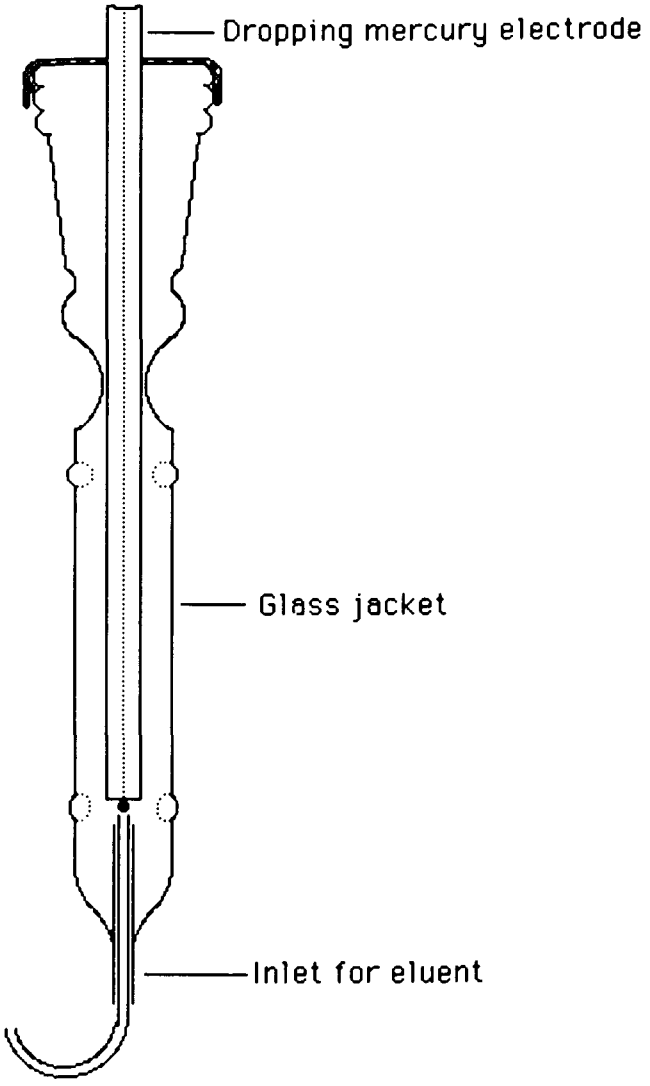

Figure 2.3 Glass adapter for HPLC-EC detector

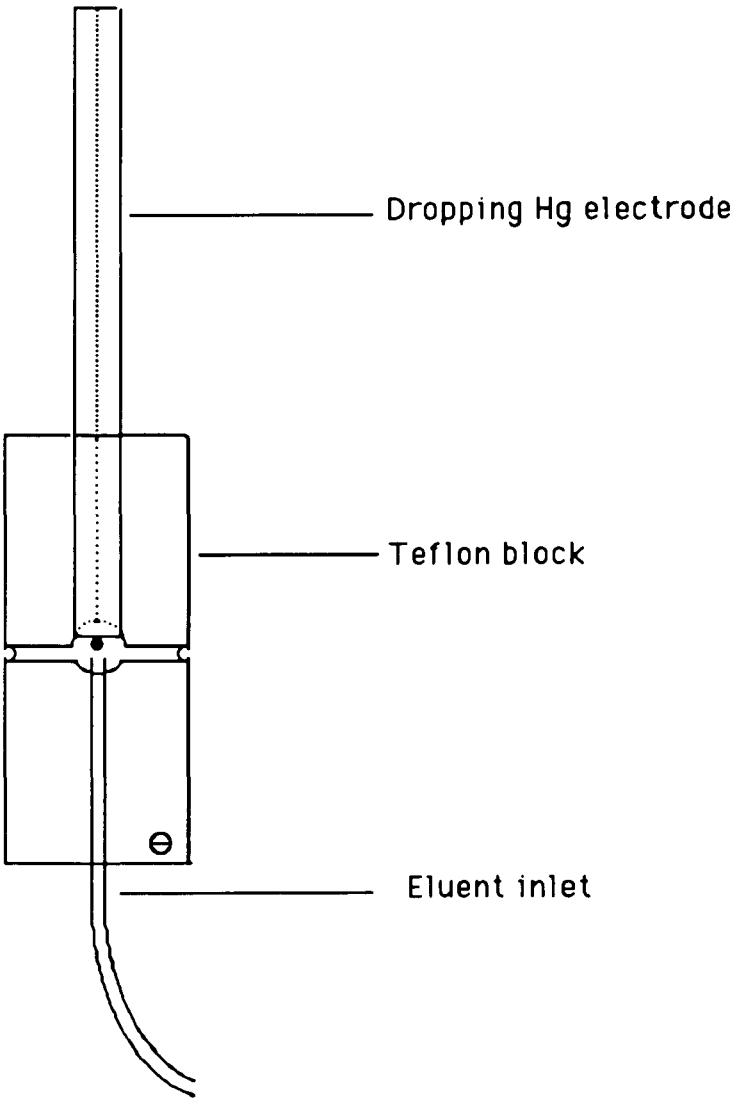

figure 2.4a Teflon plug adapter for dropping Hg electrode EC detector

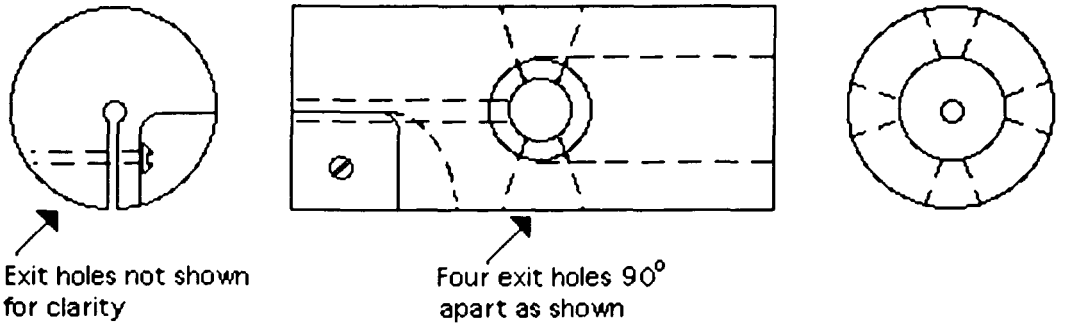

Figure 2.4b
Draftsman's drawing of teflon plug adapter for dropping mercury electrode detector

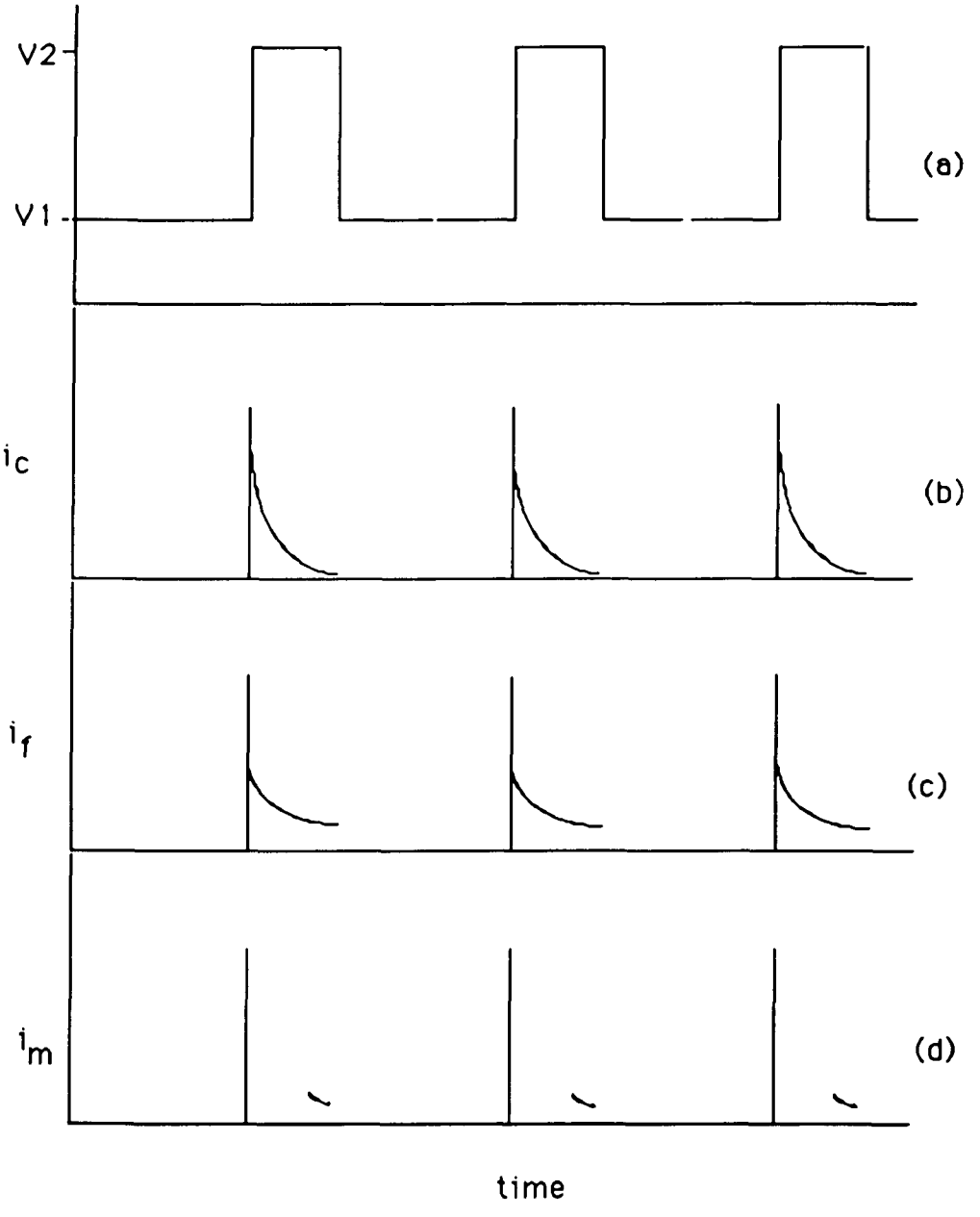

figure 2.5 (a) Potential applied on the working electrode
(b) Charging current (c) Faradaic current
(d) Current measured near the end of the pulse

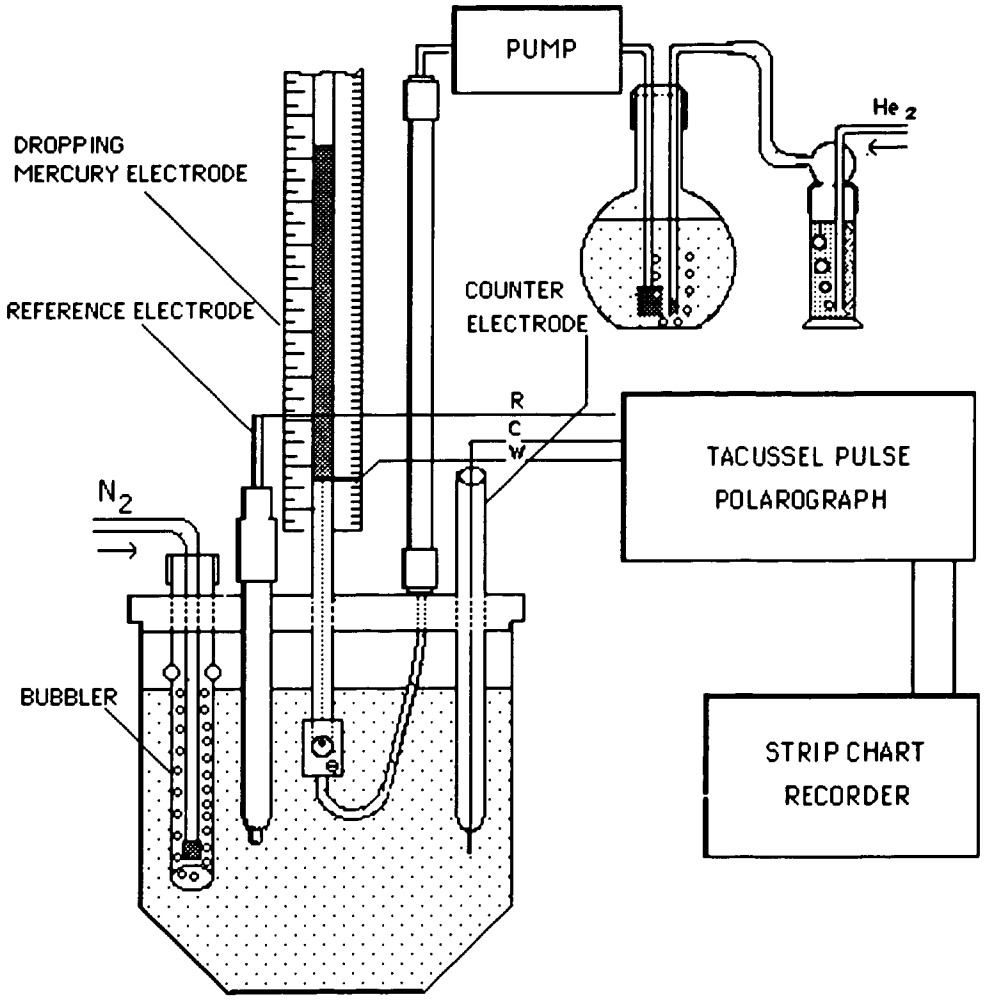

Figure 2.6 Set-up or HPLC using dropping mercury electrode EC detector

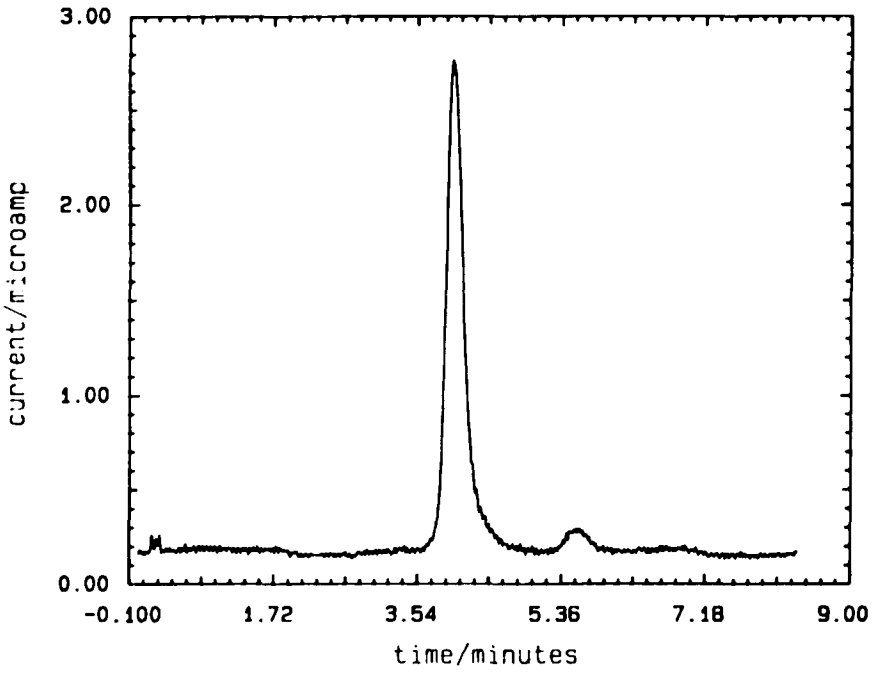

Figure 2.7 HPLC of vitamin B12. Sample:0.36 nmol(0.5μg) Mobile phase: acetonitrile:water(60:40) containing 0.05M sodium acetate, titrated to pH=5.0 with glacial acetic acid

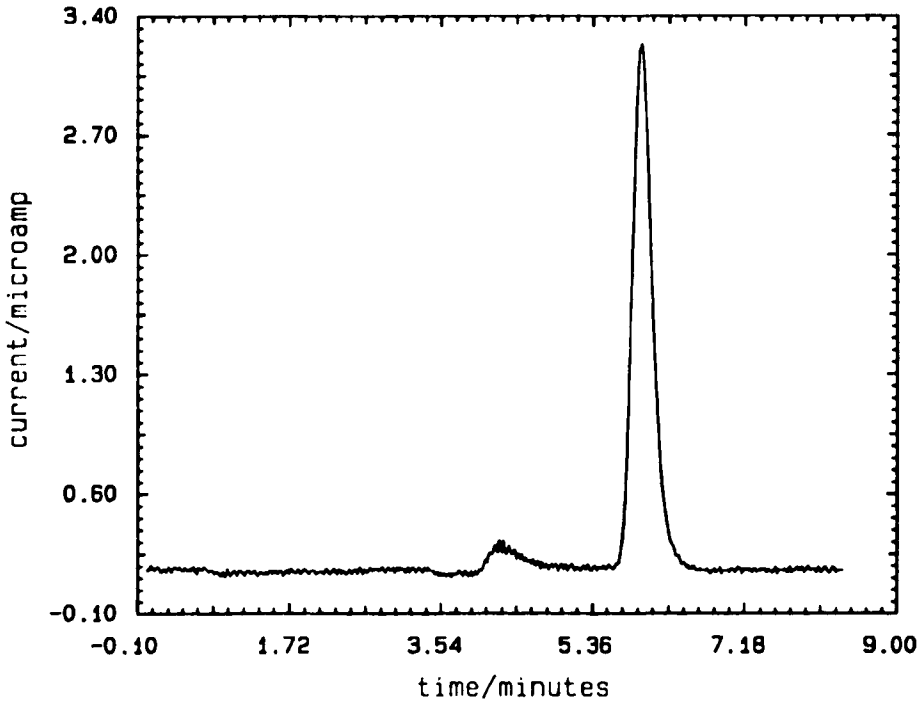

Figure 2.8 HPLC of Thiamine. Sample: 1.22nmol(0.42μg)
Mobile phase: acetonitrile:water(60:40)
Flow rate: 1mL/minute

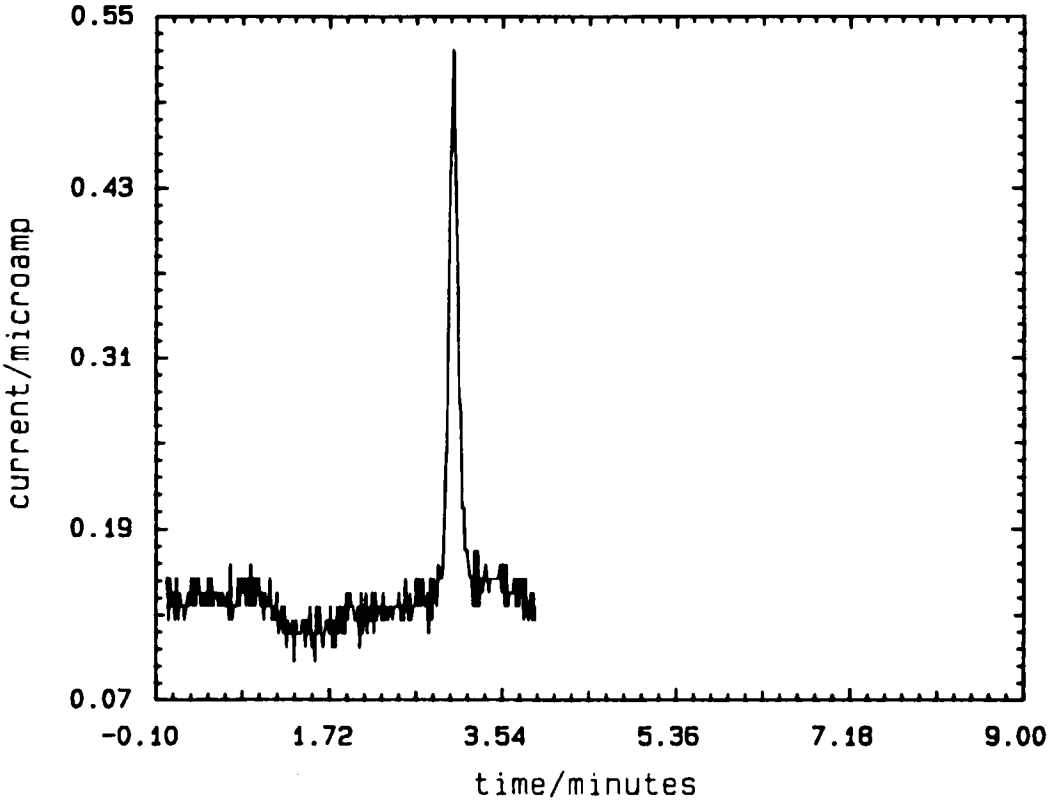

Figure 2.9 HPLC of riboflavin Sample: 1.8nmol(0.68μg)
Mobile phase: acetonitrile:water(60:40), pH=5.0
flow rate: 1mL/minute

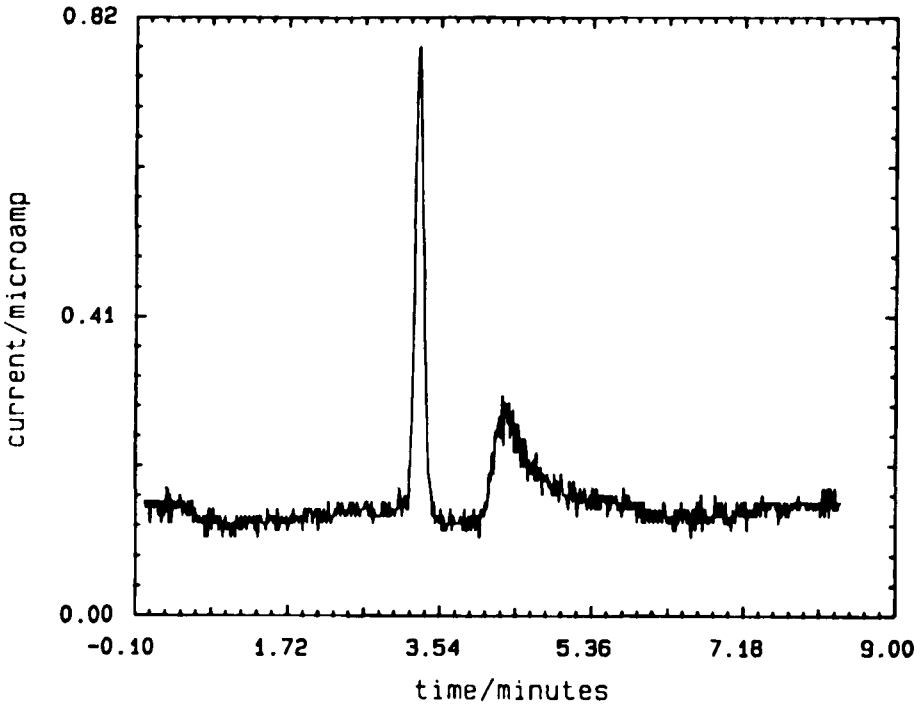

Figure 2.10 HPLC of niacinamide. Sample:0.1nmol(12.0ng)
Mobile phase: acetonitrile:water(60:40), pH=5.0
Flow rate: 1mL/minute

HPLC of mixture of riboflavin, niacinamide and thiamine

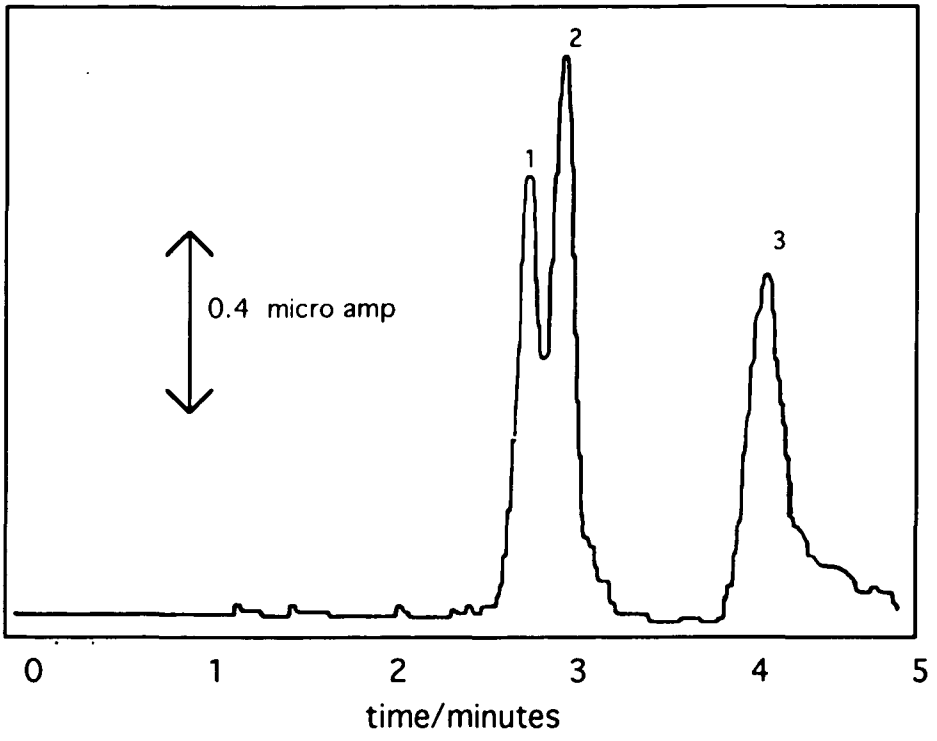

figure 2.11 Peaks 1, 2 and 3 correspond to riboflavin (0.1mmolar), niacinamide (0.1 mmolar) and thiamine (0.01mmolar) respectively.
Mobile phase: acetonitrile:water (50:50), pH 5.0
Flow rate: 1 mL/minute. Sample volume: 20 microliter.
V1=-1.40volts v2=-1.60volts

HPLC of mixture of riboflavin, vitamin B12 and thiamine

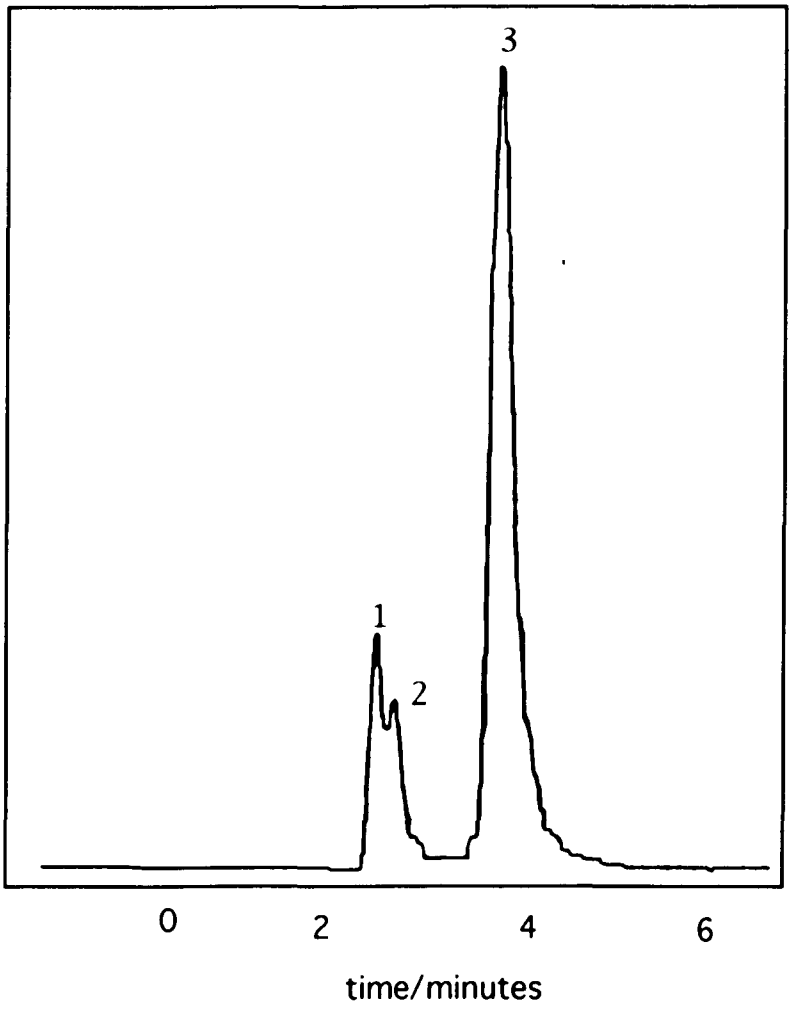

figure 2.12 Peaks 1,2 and 3 correspond to riboflavin(0.1millimolar), B12(0.01millimolar) and thiamine(0.1 millimolar) respecively.
Mobile phase: acetonitrile:water (50:50), pH 5.0
Sample volume: 20 micro liter. V1:-1400 mv V2: -1600 mv
Flow rate: 1mL/minute

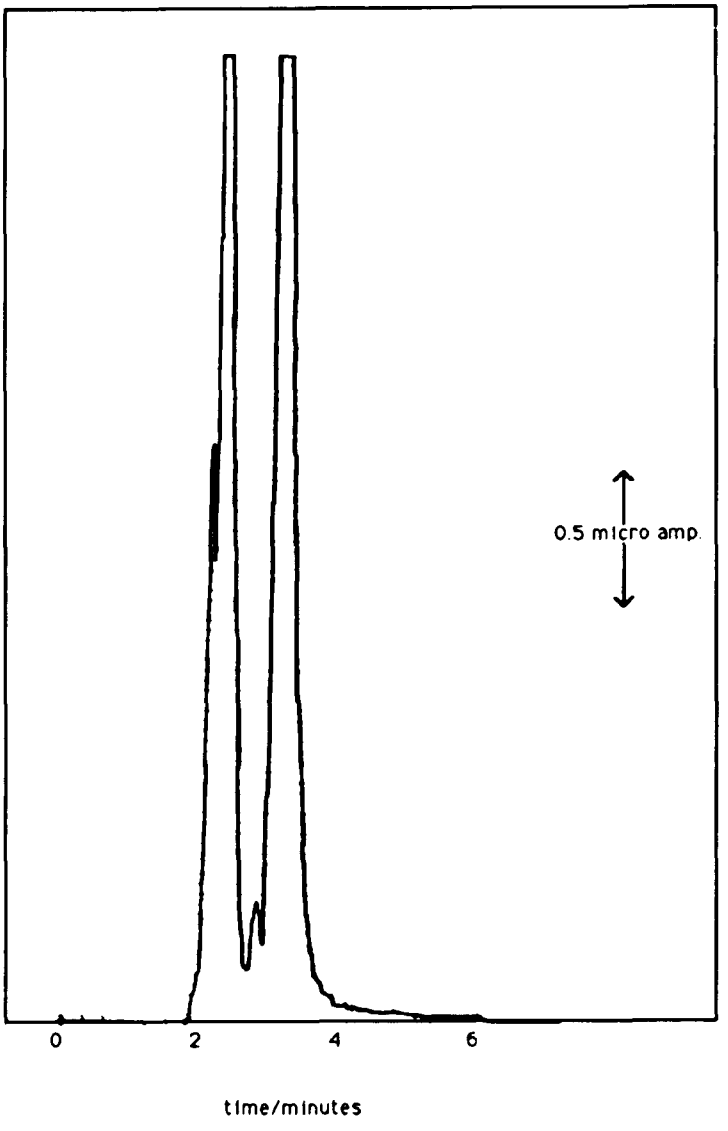

Figure 2.13 HPLC of Micebrin-T vitamin tablet.
Sample: 20 μL of a solution containing one tablet/liter
Mobile phase: acetonitrile:water (50:50), pH=5.0

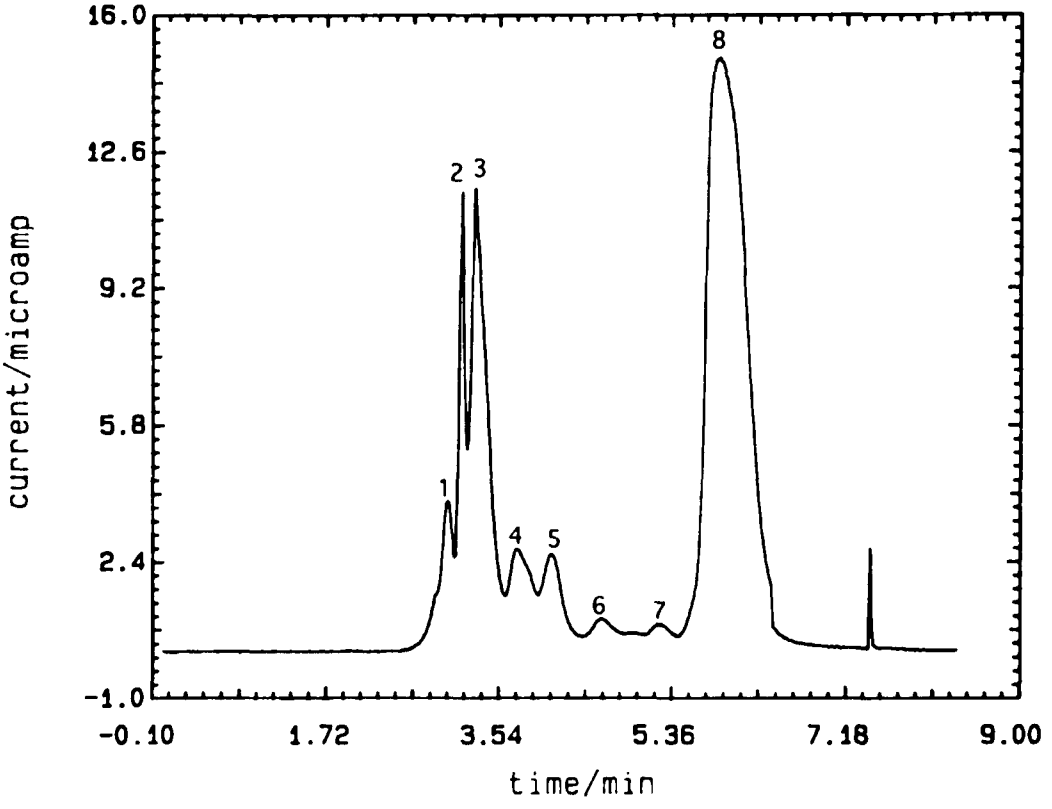

Figure 2.14 HPLC of Theragran. Sample: 20 μL of one tablet dissolved in 25 mL. Mobile phase: acetonitrile:water(60:40), PH = 5.0

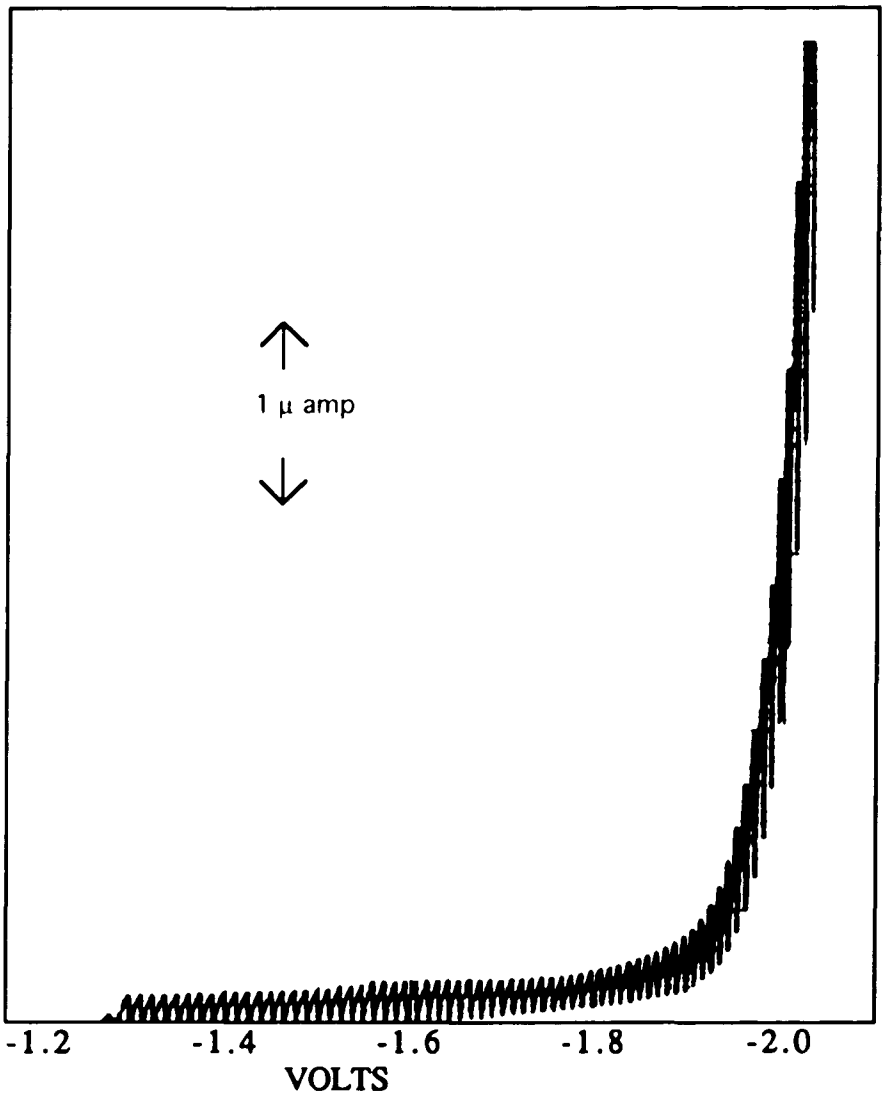

Figure 2.15a DC polarogram of Vitamin B_{12} at pH 8.56 in acetonitrile:water (50:50) mixture. Concentration of B_{12}: 8.55×10^{-5} M

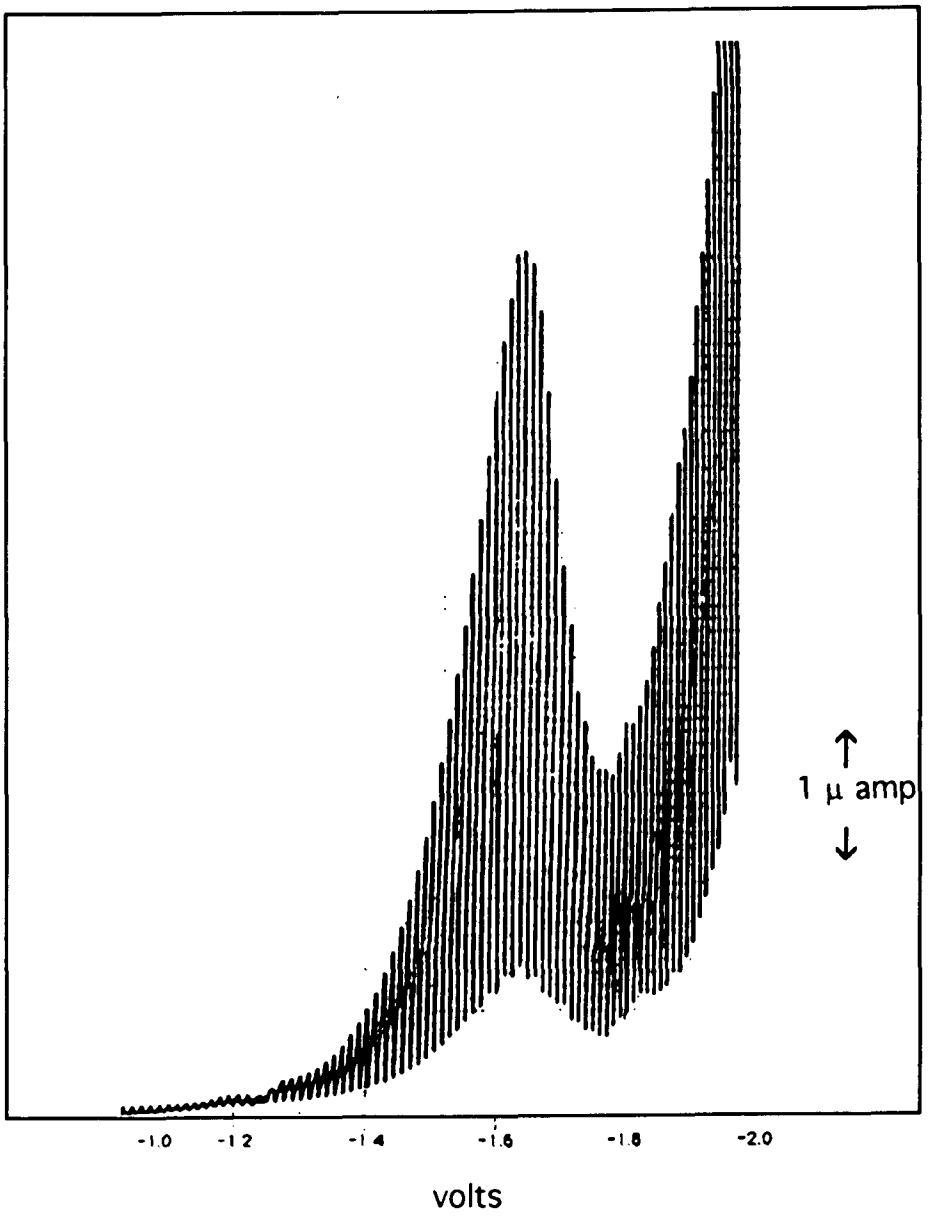

Figure 2.15b DC polarogram of vitamin B_{12} at pH 6.71 in acetonitrile:water (50:50) mixture. Conc.:8.55×10^{-5} M

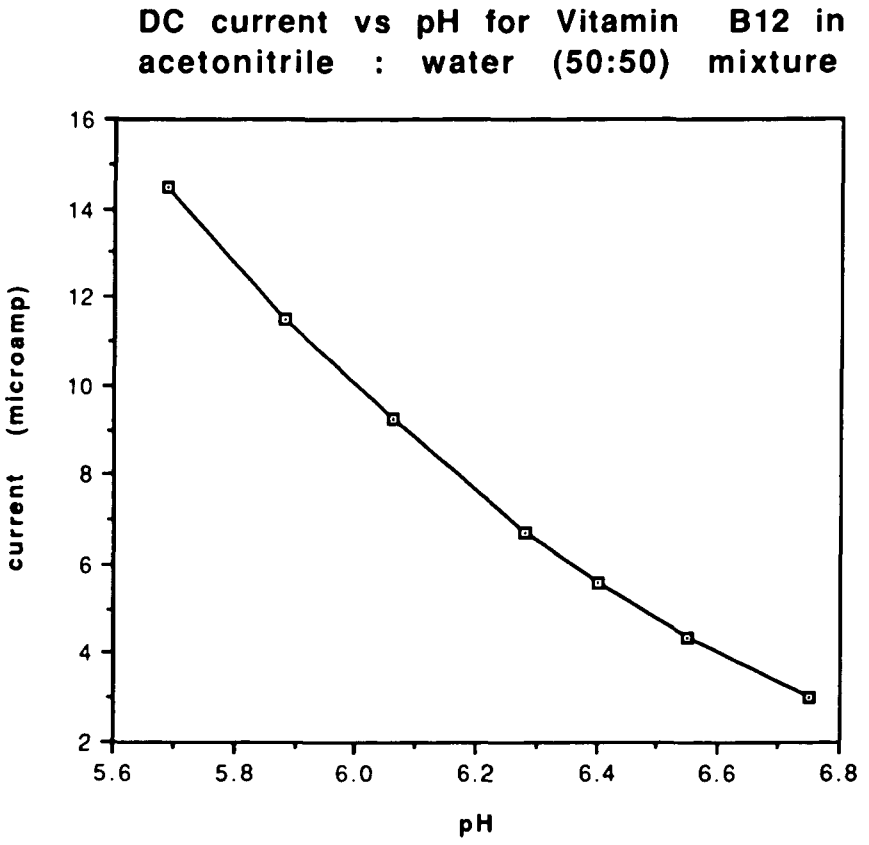

Figure 2.16
Concentration of vitamin B_{12}: 2.85×10^{-5}M

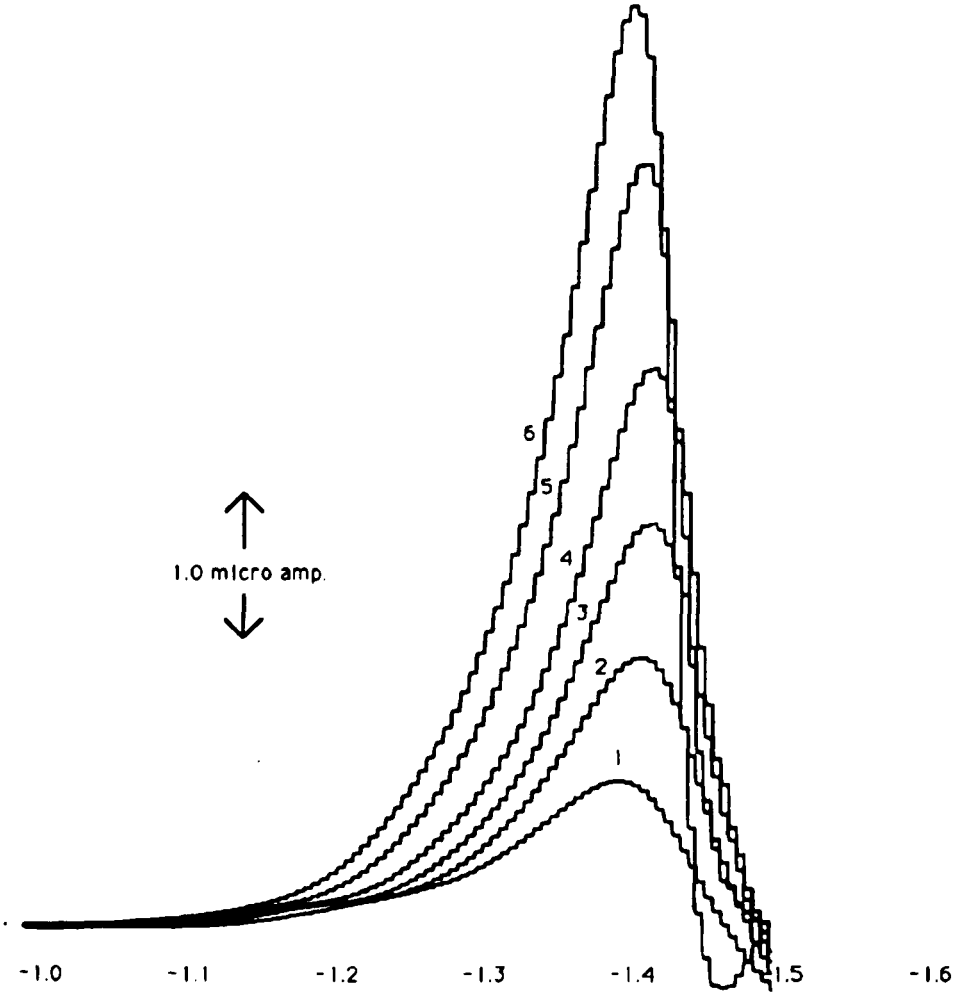

Figure 2.17a DPP of vitamin B12 vs pH. pH for curves 1, 2, 3, 4, 5 and 6 are 6.92, 6.59, 6.33, 6.08, 5.82 and 5.64 respectively. Conc. of B12: 0.88×10^{-5} M. Pulse height: 100 millivolts.

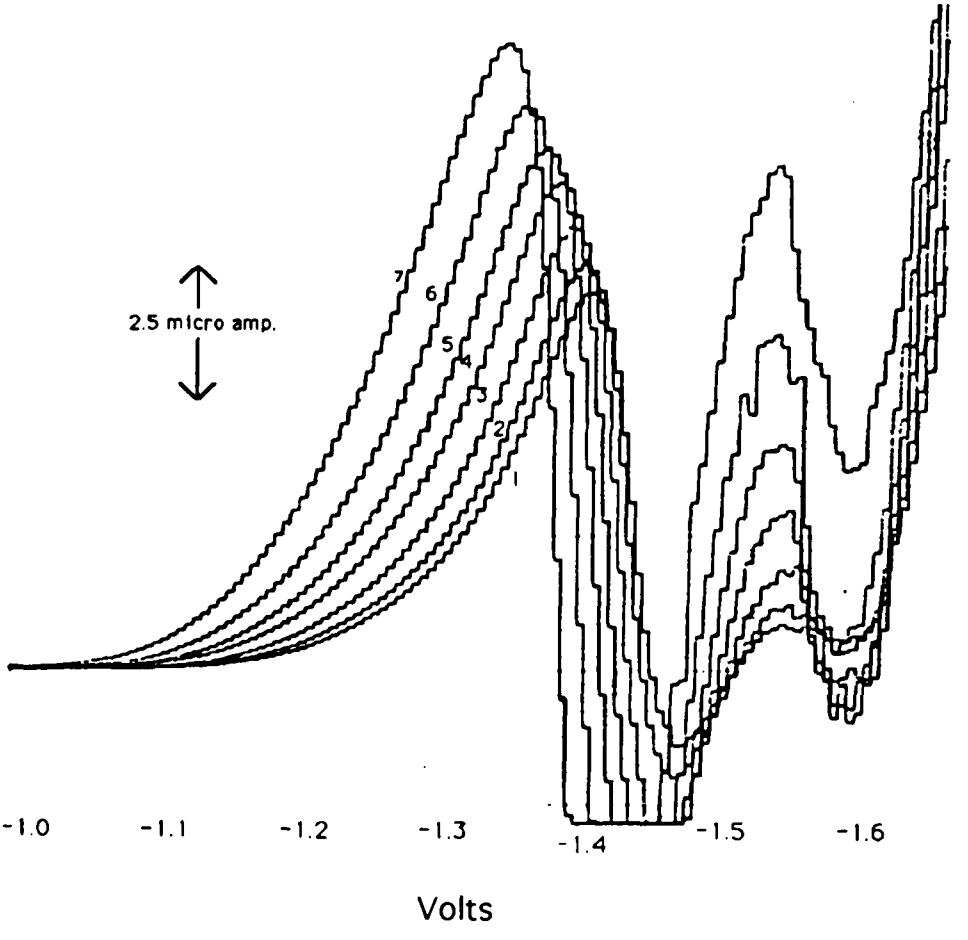

Figure 2.17b DPP of vitamin B12 vs pH pH for curves 1, 2, 3, 4, 5, 6 and 7 are 5.50, 5.42, 5.29, 5.13, 5.00, 4.83 and 4.63 respectively. Conc. of B12:0.88×10^{-5} M. Pulse height: 100 millivolts.

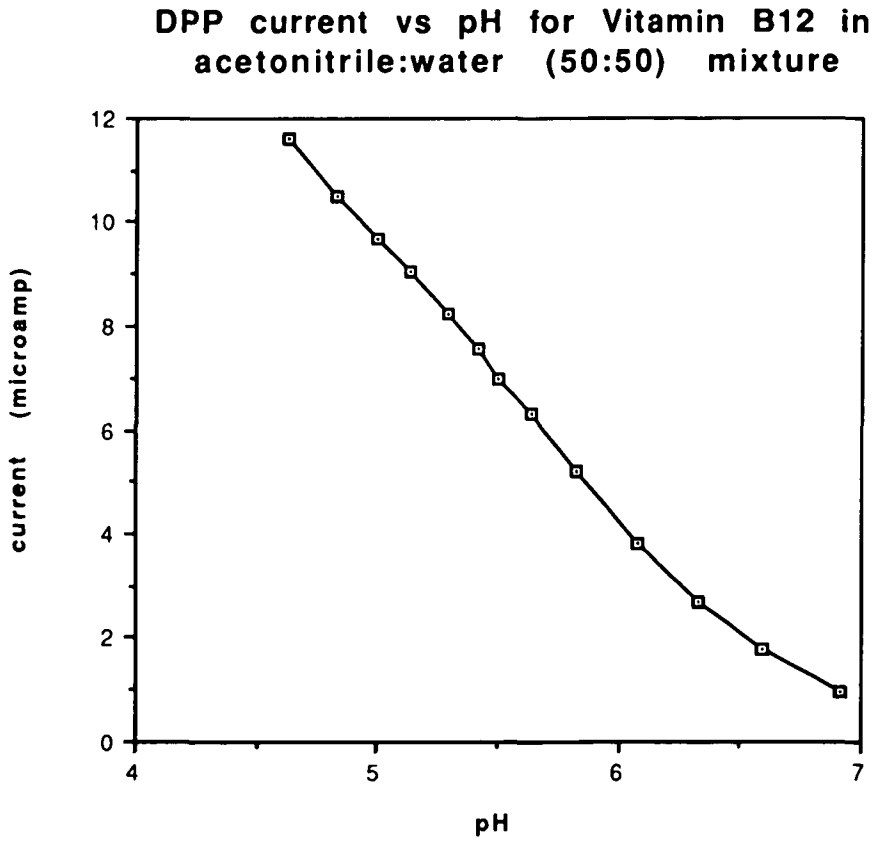

Figure 2.18 Concentration of B_{12}: 0.881 x 10^{-5} M
Pulse height: 100 millivolts

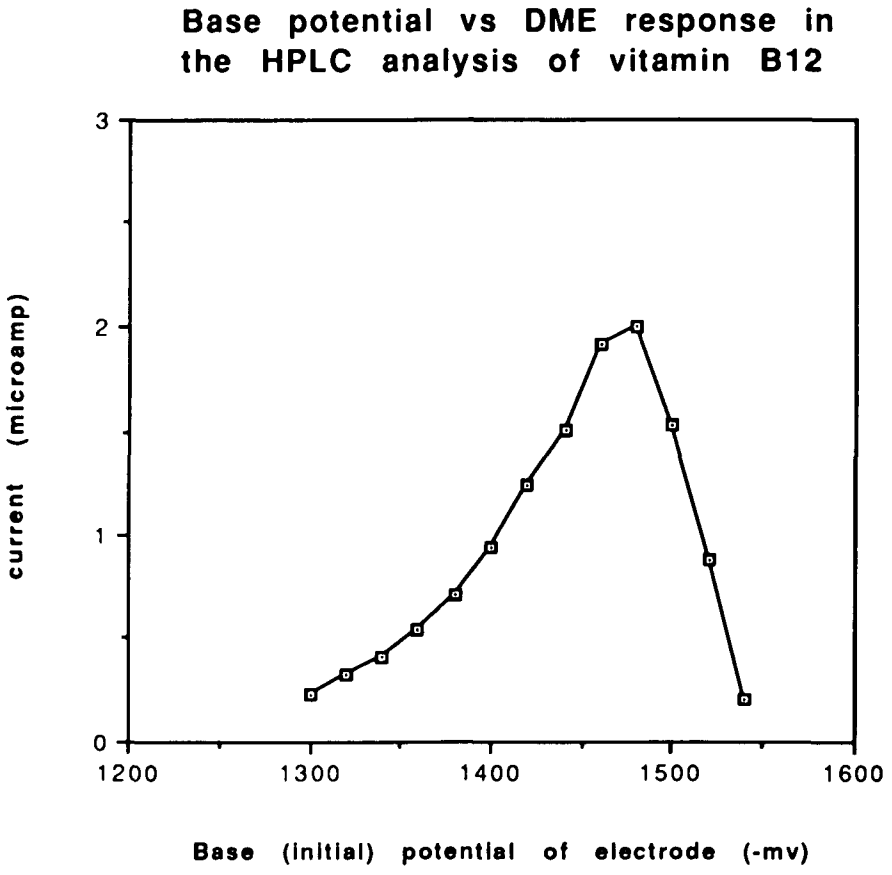

Figure 2.19
Sample: 1.0 x 10^{-5} M Vitamin B_{12}
Pulse height: 100 mv

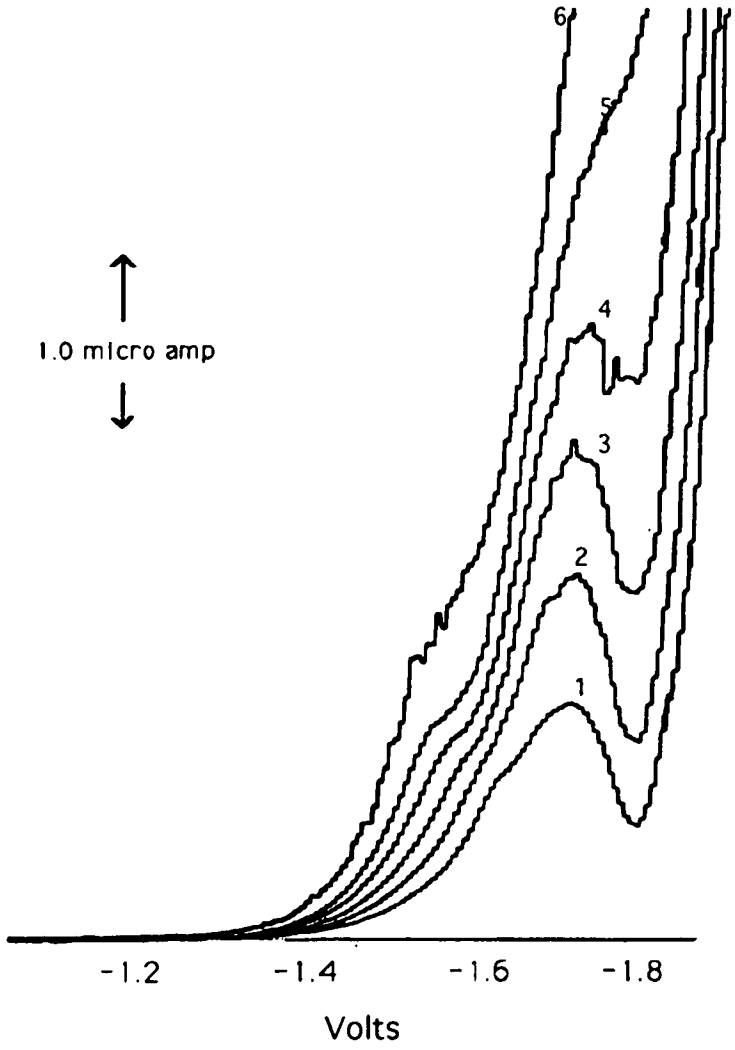

Figure 2.20 DPP of thiamine vs pH. pH for curves 1, 2, 3, 4, 5 and 6 are 6.90, 6.64, 6.44, 6.25, 6.05 and 5.81 respectively. Pulse height = 50 millivolts.

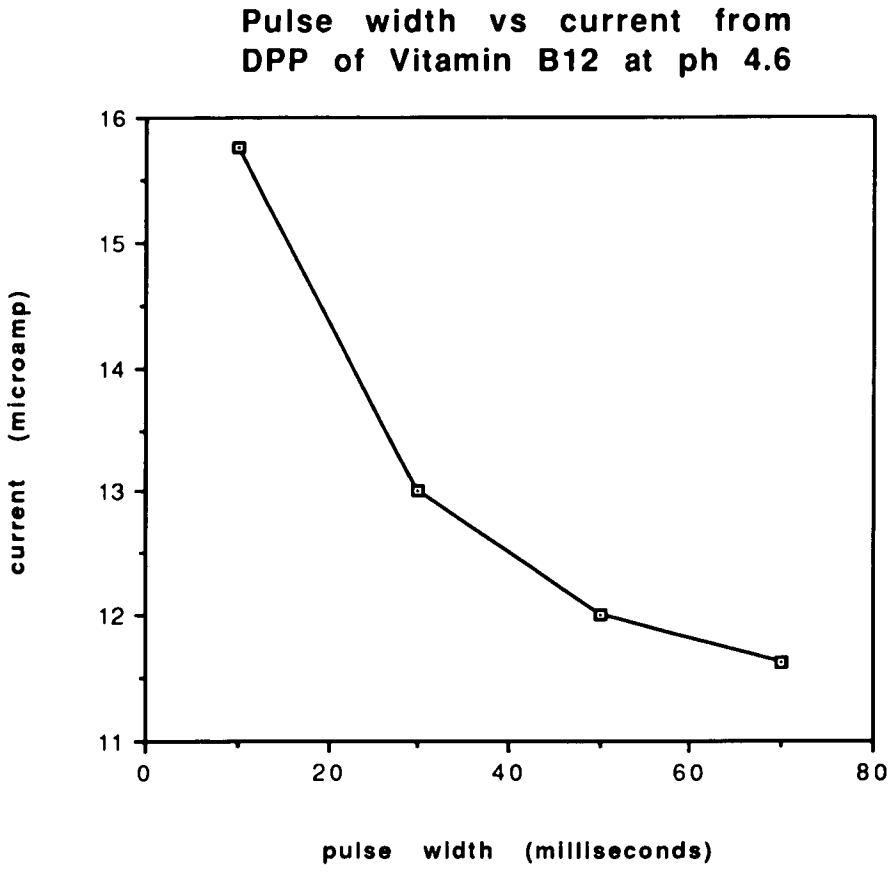
Pulse width vs current from
DPP of Vitamin B12 at ph 4.6
16
15
14
13
12
11
current (microamp)
0
20
40
60
80
pulse width (milliseconds)

Figure 2.21

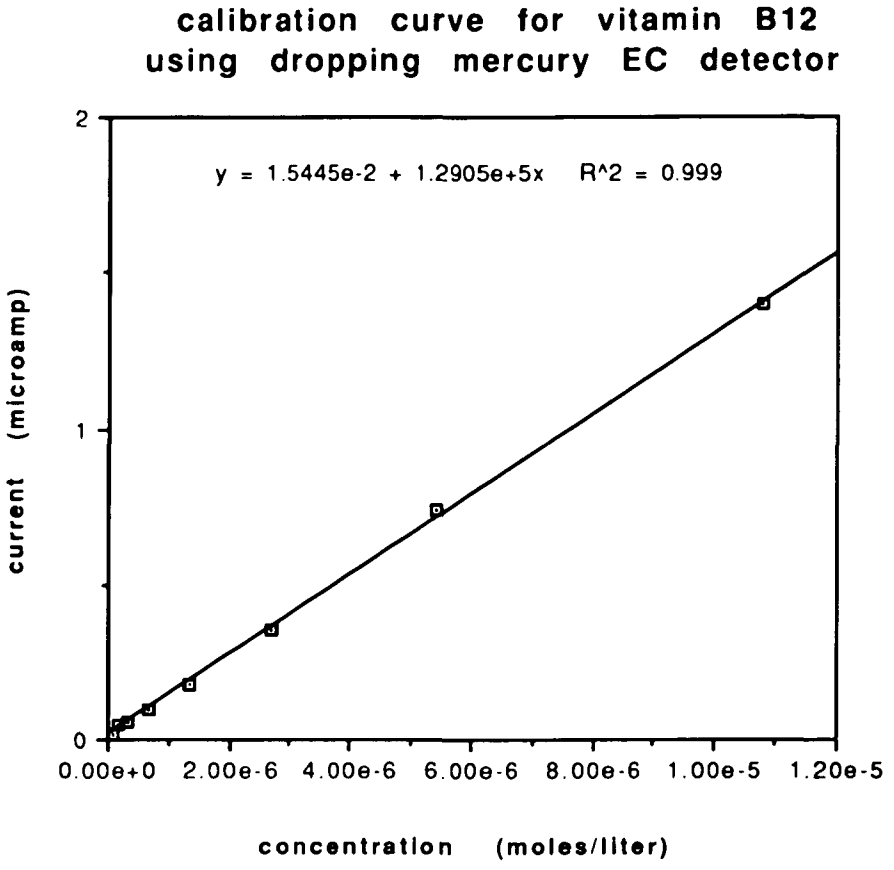

Figure 2.22. Initial potential: -1450 mv. Step potential: -1600 mv. pH 4.5. Concentration range: 4.0 x 10^{-5} to 8.0 x 10^{-8} moles/liter. Sample volume: 20 microliter.

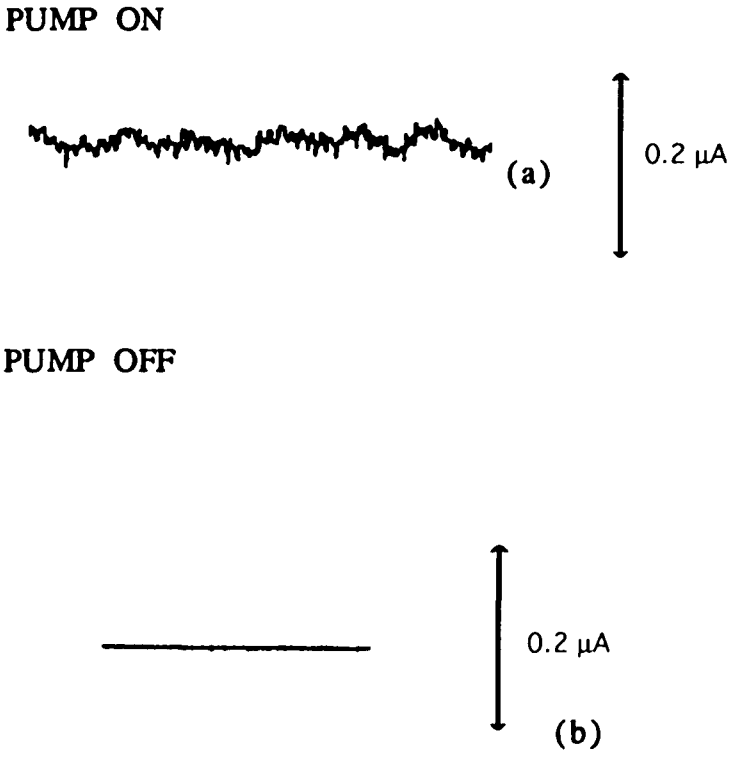

Figure 2.23 Effect of flow on background noise for EC detector using dropping mercury electrode.

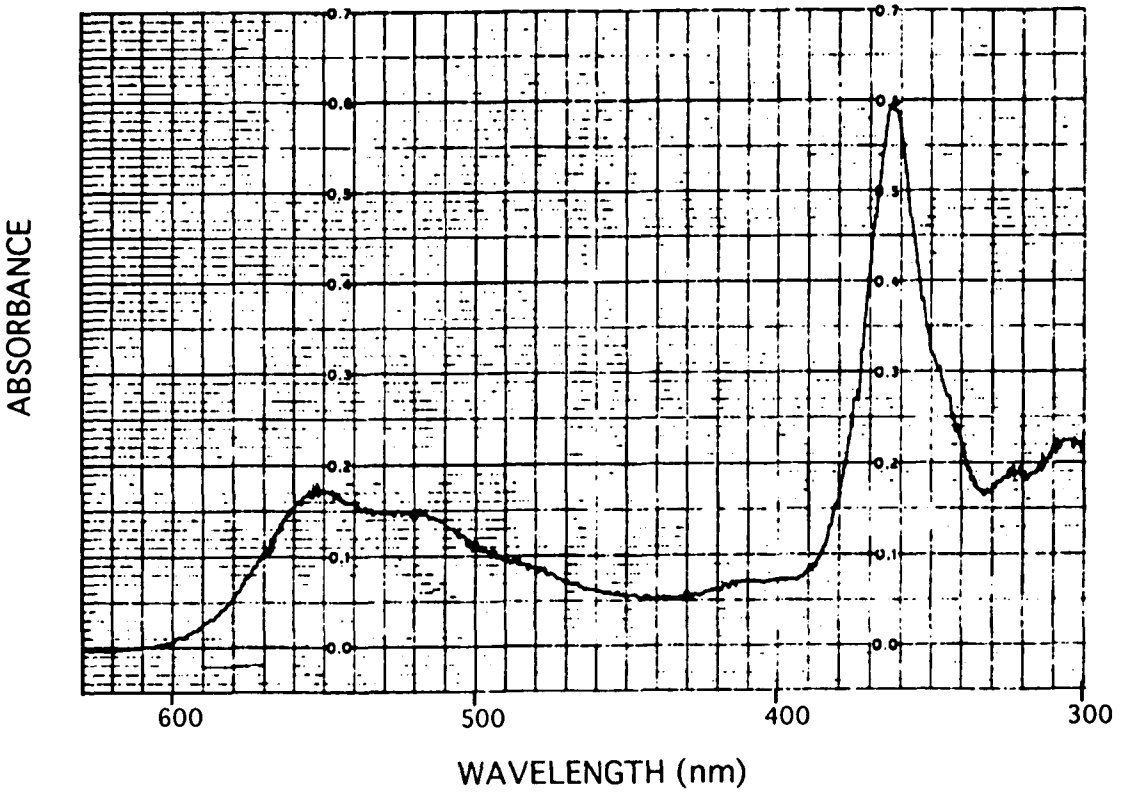

Figure 2.24 Absorption spectrum of vitamin B12 in acetonitrile: water mixture (50:50) at pH 5.0

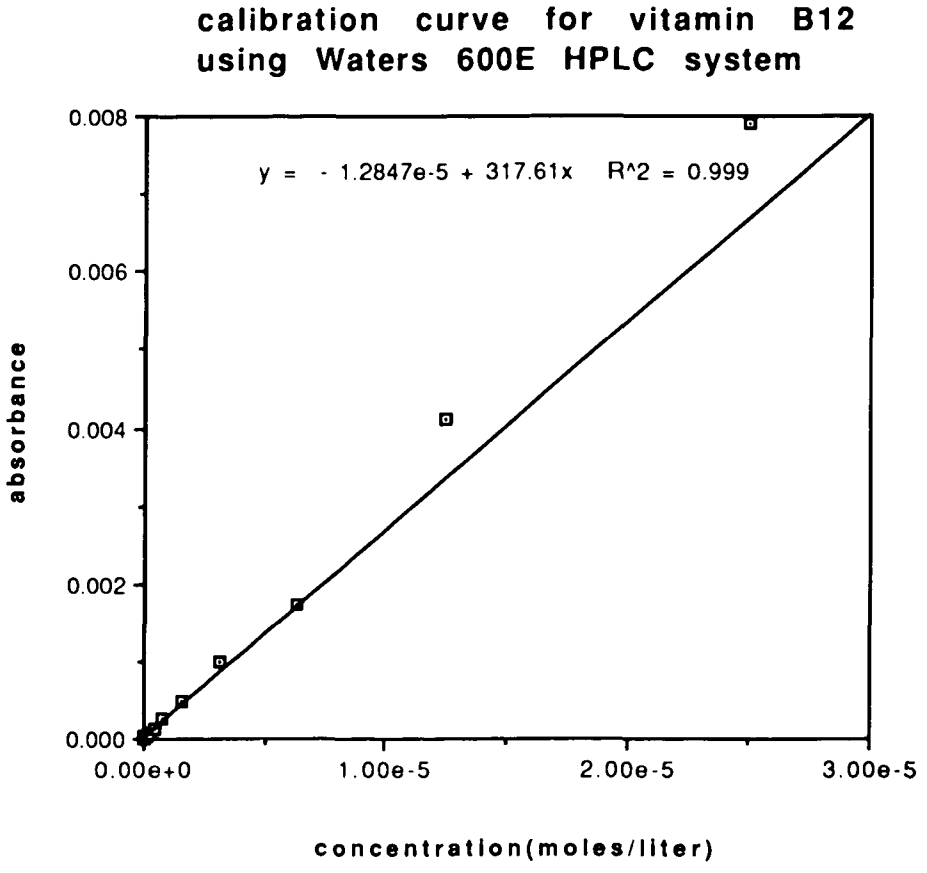

Figure 2.25. Detector response vs concentration of Vitamin B_{12} at 363 nm. Concentration range: 2.5×10^{-5} to 2.4×10^{-8} moles/liter.
Sample volume: 20 microliter.

RETENTION TIMES OF VITAMINS

SAMPLE (20 micro liter of 0.1×10^{-3} M soln.)	RETENTION TIME (minutes)
Riboflavin	3.09
Niacinamide	3.37
Vitamin B_{12} (cyano cobalamin)	4.06
Vitamin B_1 (Thiamine)	6.01

Table 2.1

Mobile Phase: acetonitrile:water (50:50) containing 0.05 molar sodium acetate, titrated to pH 5.0 with glacial HOAc
Flow rate: 1 mL/minute
Column: C18 reverse phase

REFERENCES

PART I

1. Bard, A. J.; Faulkne, L. R. "Electrochemical Methods Fundamentals and Applications"; John Wiley & Sons: New York, 1980; p 92.

2. Bockris, J. O'M.; Reddy, A. K. N. "Modern Electrochemistry"; Plenum: New York, 1970, Vol. II.

3. Brown, E. R.; Large, R. F. In "Techniques of Chemistry"; Weissberger, A.; Rossiter, B.W. ,Ed.; Wiley Interscience: New York, 1971.

4. Marquardt, D. W. J. *Soc. Indust. Appl. Math.*: **1963,** 11, 431.

5. Nelder, J. A. ; Mead, R. *Computer J.* **1965**, 7, 308.

6. Nicholson, R. S. ; Olmstead, M. L. In "Computers in Chemistry", Mercel Decker: New York, 1972.

7. Huber, A. *Montash. Math. Phys.* **1939**, 47, 240.

8. Marcoux, L. *J. Phys. Chem.* **1972**, 76, 3254.

9. Nadjo, L.; Saveant, J. M. *J. Electroanal. Chem.* **1973**, 48, 113.

10. Rickes, E. L.; Brink, N. G.; Koniuszy, F. R.; Wood, T. R.; Folkers, K. *Science* , **1948**,107, 396.

11. Smith, E. L. *Nature* **1948**, 162,144.

12. Smith, E. L.; Parker, L. F. J. *Biochem. J.* **1948**, 8, 43.

13. Diehl, H.; Haar, R. V. W.; Sealock, R. R. *J. AM. Chem. Soc.* **1950**, 72, 5312.

14. Boos, R. N.; Carr, J. E.; Conn, J. B. *Science* **1953**, 117, 603.

15. Jaselski, B.; Diehl, H. *J. Am. Chem. Soc.* **1954**, 76, 4345.

16. Abd-El-Ney, B. A. *J. Electroanal. Chem.* **1974**, 53, 317.

17. Kenyhercz, T. H.; Mark, H. B. *Anal. Lett.* **1974**, 7, 1.

18. Hogenkamp, H. P. C.; Holmes, S. *Biochemistry* **1970**, 9, 1886.

19. Bernhauer, K.; Muller, O.; Wagner, F. *Adv. enzymol.* **1964**, 26, 233.

20. Krachtovic, B; Diehl, H. *Talanta* **1966**, 13, 1013.

21. Halpern, J. In "B12 Chemistry"; Dolphin, D., Ed.; Wiley Interscience: New York, 1982, Vol. I, Chapter 14.

22. Birke, R. L.; Brydon, G. A.; Boyle, M. F. *J. Electroanal. Chem.* **1974**, 52, 237.

23. Schrauzer, G. N.; Deutsch, E.; Windgassen, R. J. *J. Am. Chem. Soc.* **1968**, 90, 2441.

24. Hill, H. A. O.; Pratt, J. M.; Williams, R. P. J. *J. Chem. Soc.* **1964**, 5149.

25. Das, P. K.; Hill, H. A. O.; Pratt, J. M.; Williams, R. P. J. *Biochem. Biophys. Acta* **1967**, 141, 644.

26. Das, P. K.; Hill, H. A. O.; Pratt, J. M.; Williams, R. P. J. *J. Chem. Soc.* **1968**, 1261.

27. Lexa, D.; Saveant, J. M. *J. Am. Chem. Soc.* **1976**, 98, 2652.

28. Schmidt, C. L.; Swofford, H. S. *Anal. Chem.* **1979**, 51, 2026.

29. Schmidt, C. L.; Koplin, C. F.; Swofford, H. S. *Anal. Chem.* **1981**, 53, 41.

30. Birke, R. L.; Venkatesan, S. *J. Electrochem. Soc.* **1981**, 128, 984.

31. Lexa, D.; Saveant, J. M.; Zickler, J. *J. Am Chem. Soc.* **1977**, 99, 2786.

32. Kenhyhercz, T. M.; De Angelis, T. P.; Norris, B. J.; Heineman, W. R.; Mark, H. B. *J. Am. Chem. Soc.* **1976**, 98, 2469.

33. Lexa, D.; Saveant, J. M. *J. Am. Chem. Soc.* **1978**, 100, 3220.

34. De Tacconi, N. R.; Lexa, D.; Saveant, J. M. *J. Am. Chem. Soc.* **1979**, 101, 467.

35. Lexa, D.; Saveant, J. M.; Zickler, J. *J. Am. Chem. Soc.* **1980**, 102, 2654.

36. Lexa, D.; Saveant, J.M. *Acc. Chem. Res.* **1983**, 16, 235.

37. Pratt, J. M. "Inorganic Chemistry of Vitamin B_{12}"; Academic Press: New York, 1972; p5.

38. Lehninger, A. L. "Biochemistry"; Worth Publishers: New York, 1975.

39. Toscano P. J.; Marzilli, L. G. In "Progress in Inorganic Chemistry"; Lippard, S. J., Ed.; John Wiley & Sons: New York, 1984: Vol. I.

40. Rubinson, K. A.; Itabashi E.; Mark Jr. H. B. *Inorg. Chem.* **1982**, 21, 3571.

41. McDuffie, B.; Anderson, L. B.; Riley, C. N. *Anal. Chem.* **1966**, 38, 883.

42. De Angelis, T. P.; Heineman, W. R. *J. Chem. Educ.* **1976**, 53, 594.

43. Kim, M. H.; Birke, R. L. *J. Electroanal. Chem.* **1983**, 144, 331.

44. Cohen, R. L.; West, K. W. "Parameter Error Printouts and Confidence Limits Using NLLSQ"; MM 69-1134-46: Bell Telephone Laboratories, 1969.

45. Foster, M. A.; Dilworth, M. J. Woods, D. D. *Nature* **1964**, 201, 39.

46. Matthews, R. G.; Drummond, J. T. *Chem. Rev.* **1990**, 90, 1275.

47. Banerjee, R. V.; Harder, S. R.; Ragsdale, S. W.; Matthews, R. G. *Biochemistry* **1990**, 29, 1129.

48. Taylor, R. T.; Weissbach, H. *Arch. Biochem. Biophys.* **1968**, 123, 109.

49. Taylor, R. T. In "B12"; Dolphin, D., Ed.; Wiley: New York, 1982; Vol. II, p 307.

50. Zydowsky, T. M.; Courtney, L. F.; Frasca, V.; Kobayashi, K.; Schimizu, H.; Yuen, L. D.; Mattews, R. G.; Benkovic, S. J.; Floss, H. G. *J. Am. Chem. Soc.* **1986**, 108, 3152.

51. Hogenkamp, H. P. C.; Bratt, G. T.; Sun, S. *Biochemistry* **1985**, 24, 6428.

PART II

52. Heyrovsky, J.; Kuta, J. "Principles of Polarography"; Academic Press: New York, 1966; p 416.

53. Babica, J.; Heyrovsky, J. *Collect. Czech. Chem. Commun.* **1940**, 2, 270.

54. Brdicka, R. *Collect. Czech. Chem. Commun.* **1936**, 8, 366.

55. Pech, J. *Collect. Czech. Chem. Commun.* **1934**, 6, 126.

56. Brezina, M.; Zuman, P. "Polarography in Medicine, Biochemistry and Pharmacy"; Interscience: New York; 1958.

57. Snyder, L. R. "Introduction to Modern Liquid chromatography"; John Wiley & Sons Inc.: New York, 1979.

58. Englehardt, H. "Practice of High Performance Liquid Chromatography"; Springer-Verlag: Berlin, 1985.

59. Troitsii, G. V. *Biokhimiya.* **1940**, 5, 375.

60. Muller, O. H. *J. Am. Chem. Soc.* **1947**, 69, 2992.

61. Drake, B. *Acta Chim. Scand.* **1950**, 4, 554.

62. Kemula, W. *Rocz. Chem.* **1952**, 26, 281.

63. Adams, R. N. "Electrochemistry of Solid Electrodes"; Marcel Dekker: New York, 1969.

64. Kissinger, P. T.; Refeshauge, C. J.; Dreiling, R.; Adams, R. N. *Anal. Lett.* **1973**, 6, 465.

65. Kissinger, P. T.; Bratin, K.; Davis, G.; Pachla, L. A. *J. Chromatogr. Sci.* **1979**, 17, 137.

66. Kissinger, P. T. *Anal. Chem.* **1977**, 49, 447A.

67. Brunt, K. "Trace Analysis"; Academic Press: New York, 1981; Vol. I.

68. Stulik, K.; Pacakova, Y. *J. Electroanal. Chem.* **1981**,129, 1.

6 9. Weber, S. G.; Purdy, W. C. J. Electroanal. Chem. **1980**, 115, 175.

70. Weber, S. G.; Purdy, W. C. *Ind. Eng. Chem. Prod. Res. Dev.* **1981**, 20, 593.

71. Krstulvoic, A. M.; Colin, H. *Analysis* **198311**, 111.

72. Bratin, K.; Kissinger, P. T. *J. Liquid Chromatogr.* **1981**, 4, 321; Suppl. 2.

73. Krstulovic, A. M. *J. Chromatogr. Biomed. Appl.* **1982**, 229, 1.

74. Allenmark, S. *J. Liquid Chromatogr.* **1982**, 5, 1.

75. Davis, G. C.; Koch, D. D.; Kissinger,P. T.; Bruntlett, C. S.; Shoup, R. E. In "Liquid Chromatography in Clinical Analysis"; Kabra, P. M.; Marton, L. J., Ed.; Humana Press: Clifton, N. J., 1981.

76. MacCrehan, W. A.; Durst, R. A.; Bellama, J. M. *Anal. Lett.* **1975**, 10, 1175.

77. Richards, D. A. *Surface Technol.* **1982**, 15, 113.

78. Muller, T. H.; Unsicker, K. *J. Neurosci. Methods* **1981**, 4, 39.

79. Kissinger, P. T.; Bruntlett, C. S.; Shoup, R. E. *Life Sci.* **1981**, 28, 455.

80. Mefford, I. N. *J. Neurosci. Methods* 1981, 3, 207.

81. Gunasingham, H.; Fleet, B. *Anal. Chem.***1983**, 55, 1409.

82. Oosterhuls, B.; Brunt, K.; Westerink, B. H. C.; Doornobs, D. A. *Anal. Chem.* **1980**, 52, 203.

83. Lankelma, J.; Poppe, H. *J. Chromatogr.* **1976**,125, 375.

84. Polta, T. C.; Johnson, D. C. *J. Electroanal. Chem.* **1986**, 209, 159.

85. Gunasingham, H.; Tay, B. T.; Ang, K. P. *Anal. Chem.* **1986**, 58, 1578.

86. Schneiderman, M. A.; Sharma, A. K.; Locke, D. C. *J. Chromatogr.* **1987**, 409, 343.

87. Hughes, S.; Johnson, D. C. *Anal. Chim. Acta* **1981**, 132, 11.

88. Coudill, W. L.; Ewing, A. G.; Jones, S.; Wightman, M. *Anal. Chem.* **1983**, 55, 1877.

89. Wang, J.; Dewald, H. D. *Talanta* **1984**, 31, 387.

90. Gunasingham, H. *Anal. Chim. Acta* **1984**, 159, 139.

91. Gunasingham, H.; Tay, B. T.; Ang, K. P. *Anal. Chem.* **1984**, 56, 2422.

92. Krstulovic, A. M.; Colin, H.; Guiochon, G. A. *Adv. Chromatogr.* 24, 83.

93. Johnson, D. C.; Weber, S. G.; Bond, A, M.; Wightman, R. M.; Shoup, R. E.; Krull, I. S. *Anal. Chim. Acta* **1986**, 180, 187.

94. Stillman, R.; Ma, T. S. *Mikrochim. Acta* **1973**, 31, 491.

95. Stillman, R.; Ma, T. S. *Mikrochim. Acta* **1974**, 32, 641.

96. Ashley, L.; Levine, S. L. *Talanta* **1983**, 30, 515.

97. Kowalski, Z.; Kubiak, W. *Anal. Chim. Acta* **1984**, 159, 129.

98. Reardon, P. A.; O'Brien, G. E.; Sturrock, P. E. *Anal. Chim. Acta* **1984**, 162, 175.

99. Scanlon, J. J.; Flaquer, P. A.; Robinson, G. W.; O'Brien, G. E.; Sturrock, P. E. *Anal. Chim. Acta* **1984**, 158, 169.

100. Wang, J.; Ouziel, E.; Yarnitzky, C.; Ariel, M. *Anal. Chim. Acta* **1978**, 102, 99.

101. Elferink, F.; van der Vigh, W. J. F.; Pinedo, H. M. *Anal. Chem.* **1986**, 58, 2293.

102. Hou, W.; Wang, E. *Analyst* **1990**, 115, 139.

103. Jansen, C. C.; Kleijn, J. P. *J. Chromatogr. Sci.* **1990**, 28, 42.

104. Piraner, I. M.; Bershtein, I. Y.; Komarov, E. V. *Khim.-Farm. Zh.*, **1989**, 23, 1.

105. Amin, M.; Reusch, J. *J. Chromatogr.* **1987**, 390, 448.